

SELF-ASSEMBLED POLYMER  
NANOCOMPOSITES AND THEIR NETWORKS

By

NITIN VIKAS PATIL

Bachelor of Polymer Engineering and Technology  
University Institute of Chemical Technology  
Mumbai, Maharashtra; India  
2006

Submitted to the Faculty of the  
Graduate College of the  
Oklahoma State University  
in partial fulfillment of  
the requirements for  
the Degree of  
DOCTOR OF PHILOSOPHY  
December, 2013

SELF-ASSEMBLED POLYMER NANOCOMPOSITES  
AND THEIR NETWORKS

Dissertation Approved:

Dr. Jeffery L. White

---

Dissertation Adviser

Dr. Frank D. Blum

---

Dr. Kevin D. Ausman

---

Dr. Allen Applett

---

Dr. Rob Whiteley

---

## ACKNOWLEDGEMENTS

I would like to express deepest gratitude to my advisor Dr. Jeffery L. White for his guidance, support, motivation, enthusiasm, and immense knowledge. I would also like to acknowledge Pandit. Shri Ram Sharma Acharya for making me an ethical and principled human being.

I would like to thank my committee members: Dr. Frank D. Blum, Dr. Kevin D. Ausman, Dr. Allen Apblett, and Dr. Rob Whiteley for their valuable comments. I would like to give special thanks to Dr. Warren T. Ford, Dr. Brian P. Grady, Dr. Frank D. Blum, and Dr. Nicholas F. Materer for allowing me to use their instruments.

Additional thank to my past and present lab mates: Dr. Rosimar Truitt, Dr. Lance Gill, Dr. Gaumani Gyanwali, Josh, Jessica, Dr. Andrew Clough, Tapash, Chen, Jarred, and Mathis for their valuable comments in my PhD research. I would like to thank my friends: Sovan, Atri, Harshwardhan, Chakkaravarthy, Farai, Joseph, and Lakshmi for making my stay at OSU exciting.

Last, I would like to thank my parents, brothers, wife, sister-in law, my nephew Bhargav, and my son Savya for their support, encouragement, love, and motivation throughout my doctorate studies.

Name: NITIN VIKAS PATIL

Date of Degree: DECEMBER, 2013

Title of Study: SELF-ASSEMBLED POLYMER NANOCOMPOSITES AND THEIR NETWORKS

Major Field: CHEMISTRY

Abstract:

This dissertation describes new routes to synthesize polymer nanocomposite networks via self-assembly. Polymerizable structure directing agents (referred to as surfmers) obtained by end-group functionalization preserves the structure-directing capabilities of the surfactant for templating ordered mesoporous silica particle growth, while simultaneously generating a reactive matrix for polymer network formation through reactive end groups in the presence of intimately mixed mesoporous silicates. A combination of small angle X-ray scattering, surface area, and microscopy experiments on mesoporous silica indicated the structure directing capabilities of surfmers. Free-radical polymerization of the surfmer leads to novel crosslinked nanocomposites networks. Multiple experiments, including gel permeation chromatography, swelling, and solid state NMR experiments on polymer nanocomposites gave evidence of the polymerization of surfmer leading to formation of crosslink networks. Polymer nanocomposites with varied silica content were prepared. Effects of silica content on polymer nanocomposites were studied on rheometer. Results obtained from rheological experiments indicate that the storage ( $G'$ ) and loss modulus ( $G''$ ) increases with increase in the content of mesoporous silica. In this way, the nanocomposites networks obtained via self-assembly shows independent behavior with respect to frequency in rheological experiments. Additionally, this self-assembled route was extended to synthesize biodegradable and biocompatible polymer nanocomposites networks. The nanocomposite networks obtained with 15% of silica content showed the increase in storage modulus by two orders of magnitude in rheological experiments.

## TABLE OF CONTENTS

Chapter	Page
I. INTRODUCTION.....	1
1.1 Polymer Composites.....	1
1.2 Factors affecting the properties of polymer composites.....	2
1.2.1 Interfacial Adhesion.....	2
1.2.2 Orientation of inorganic fillers in polymer matrix.....	3
1.2.3 Dispersion of inorganic fillers into polymer matrix.....	4
1.3 Polymers.....	4
1.4 Properties of Polymer Composites.....	10
1.5 Mesoporous Silica.....	12
1.6.1 True Crystal Liquid Templating.....	16
1.6.2 Co-operative Self-Assembly.....	16
1.6.3 Evaporation Induced Self-Assembly.....	17
1.6.4 Exo-templating.....	18
1.6 Motivation.....	19
1.7.1 Co-condensation Method.....	21
1.7.2 Post-functionalization Method.....	23
1.7.3 Sol-gel Method.....	24
1.7 Approach.....	26
1.8 Research Objectives.....	27
1.9 Experimental Techniques.....	28
1.9.1 Physisorption.....	28
1.9.2 Differential Scanning Calorimetry.....	32
1.9.3 Thermal Gravimetric Analysis.....	33
1.9.4 Gel Permeation Chromatorgraphy.....	34
1.9.5 Rheology.....	36
1.9.6 Small Angle X-ray Scattering.....	39
1.9.7 Nuclear Magnetic Resonance.....	40
1.9.7.1 Bloch Decay experiments.....	45
1.9.7.2 Cross-Polarization experiments.....	46
1.10 Structure of dissertation.....	48
1.11 References.....	48

Chapter	Page
II. POLYMERIZATION STRUCTURE DIRECTING AGENTS THAT ENABLE IN-SITU SYNTHESSES OF COMPOSITE MATERIALS .....	58
2.1 Introduction.....	59
2.2 Experimental.....	60
2.2.1 Materials .....	60
2.2.2 Characterization .....	61
2.2.3 Synthesis of monoallyl Pluronic P123 .....	61
2.2.4 Synthesis of SBA-15 and SBA-15 analogues.....	62
2.2.5 Polymerization of monoallyl pluronic P123 .....	62
2.2.6 Characterization of extent of end-group functionalization in aP123 .....	63
2.3 Results and Discussion .....	64
2.3.1 Generating functionalized templates.....	64
2.3.2 Polymerizing the reactive template.....	68
2.3.3 Inter-particle versus intra-particle polymerizations and bulk properties .....	70
2.4 Conclusions.....	72
2.5 References.....	73
III. Self-ASSEMBLED POLYMER NANOCOMPOSITES AND THEIR NETWORKS .....	76
3.1 Introduction.....	77
3.2 Experimental.....	78
3.2.1 Materials .....	78
3.2.2 Characterization .....	78
3.2.3 Synthesis of acrylated- and styrenated- functionalized pluronic P123 .....	78
3.2.2 Synthesis of SBA-15 and SBA-15 analogues (acryP123 and styrP123) .....	79
3.2.3 Characterization of end-group functionalization in acry/styrP123 .....	80
3.2.4 Preparation of polymer nanocomposites.....	82
3.3 Linear Viscoelastic Measurements .....	84
3.4 Small Angle X-ray Scattering Measurements.....	84
3.5 Results and Discussion .....	85
3.6 Conclusions.....	93
3.7 References.....	94
IV. CREATING POLYMER TEMPLATES AND THEIR USE IN THE IN-SITU SYNTHESIS OF BIODEGRADABLE NANOCOMPOSITES .....	97
4.1 Introduction.....	98
4.2 Experimental.....	99
4.2.1 Materials .....	99
4.2.2 Characterization .....	99

4.2.3 Synthesis of PECE-4K and PECE-6K triblock copolymers .....	100
4.2.2 PECE end-group functionalization to form acrylated-PECE.....	102
4.2.3 PECE-templated porous-silica formation .....	102
4.2.4 Preparation of polymer nanocomposites from PECE/silica products...	103
4.3 Linear Viscoelastic Measurements .....	104
4.4 Small Angle X-ray Scattering Measurements.....	104
4.5 Results and Discussion .....	104
4.6 Conclusions.....	114
4.7 References.....	115
V. FUTURE WORK.....	119
APPENDICES .....	121

## LIST OF TABLES

Table	Page
1.1 Silane coupling agents .....	26
2.1 Pore size distributions, BET surface area, and d-spacing of mesoporous silica prepared using aP123 and P123 .....	68
3.1 Pore size distributions, BET surface area, and d-spacing of mesoporous silica prepared using styrP123, acryP123, and P123 .....	80
3.2 Composition of SBA15acryP123 polymer nanocomposites.....	83
4.1 Composition of MSacryPECE polymer nanocomposites .....	103
4.2 BET surface area and pore volume .....	106



## LIST OF FIGURES

Figure	Page
1.1 Chemical structures of <b>a</b> ) poly(isoprene) a naturally occurring polymer and <b>b</b> ) poly(vinyl chloride)-synthetic polymers.....	5
1.2 Different types of branching in polymers: a) linear, b) branched, c) cross-linked, and d) dendrimers.....	6
1.3 Condensation polymerization technique for synthesis of polyesters.....	6
1.4 Free-radical polymerization sequence .....	7
1.5 Arrangements of monomers to form: a) random, b) alternating, c) block, and d) gradient copolymers.....	8
1.6 Schematic representation of graft copolymers.....	8
1.7 Molecular weight distributions: a) narrow and b) broad .....	10
1.8 a) Dumbbell shaped polymer/ polymer composites specimen and b) typical stress-strain curve for polymers .....	11
1.9 Stress-strain curves of a) Soft and weak, b) soft and tough, c) hard and brittle, d) hard and strong, and e) hard and tough polymeric materials .....	11
1.10 Classification of nanoporous materials.....	12
1.11 Sol-gel hydrolysis and condensation reactions.....	13
1.12 Types of electrostatic interactions: a) $S^+T^-$ , b) $S^+X^-T^+$ , c) $ST^+$ , and d) $S^-M^+T^+$ that can occur between surfactant and silica species.....	14

1.13 Silica precursors under different pH .....	15
1.14 Mechanism of mesoporus silica formation by a) true liquid crystal templating and b) co-operative self-assembly routes.....	17
1.15 Schematic representation of EISA approach .....	18
1.16 Schematic representation of exo-template approach for mesoporous materials .	19
1.17 TEM images of mesoporous silica pores of a) cubic, b) hexagonal, and c) SEM image spherical shapes.....	20
1.18 Comparison of articles published on a) polymer silica nanocomposites and b) polymer mesoporous silica nanocomposites from 1998 to 2012.....	20
1.19 Mesoporous silica/polymer nanocomposites by co-condensation approach .....	22
1.20 Mesoporous silica/polymer nanocomposites using post-functionalization approach .....	24
1.21 Polymer nanocomposites using the sol-gel approach .....	25
1.22 Schematic representation of ring-opening polymerization of D,L-lactide inside the mesoporous silica.....	25
1.23 Schematic representation of polymerizable structure directing agent approach for the synthesis of polymer mesoporous silica nanocomposites.....	27
1.24 Schematic representation of physisorption experiments.....	29
1.25 a) Isotherms and b) hysteresis loop of type IV isotherm .....	30
1.26 Typical BET plot.....	31
1.27 Schematic representation of DSC cell .....	32
1.28 Typical DSC thermogram.....	33
1.29 Typical TGA thermogram.....	34

1.30 Schematic representation of Agilent 1100 series Gel Permeation Chromatography .....	35
1.31 a) Calibration curve using polystyrene standards and b) GPC chromatogram of unknown sample .....	36
1.32 Mechanical analog of a viscoelastic liquid .....	37
1.33 Schematic representation of parallel plates used in Rheometric scientific RSA II.....	38
1.34 Plot of $G'$ with respect to frequency of a viscoelastic material .....	39
1.35 Schematic representation of a) SAXS instrument and b) diffraction of rays from sample .....	40
1.36 Splitting of energy levels in the presence of the external magnetic field ( $B_0$ ) ....	41
1.37 Axis of rotation of nucleus in the presence of the external magnetic field ( $B_0$ )..	42
1.38 Bulk magnetization of the spins aligned in the direction of the external magnetic field .....	43
1.39 Two spin system in the magnetic field $B_0$ .....	44
1.40 Sample rotor at magic angle with respect to applied magnetic field ( $B_0$ ) .....	45
1.41 a) Pulse diagram of Bloch decay experiment and b) vector model representation of spins after $90^\circ$ pulse .....	46
1.42 Zeeman splitting occurring at Hartmann-Hahn condition .....	47
1.43 Pulse diagram of CP/MAS NMR.....	47
2.1 600 MHz $^{13}\text{C}$ solution NMR spectrum acquired with $^1\text{H}$ decoupling of (bottom) pure P123 starting material and (top) allyl-functionalized aP123 following reaction according to Scheme 1. End group signals are shown in the aP123 inset.....	64

2.2 a) Schematic representation of synthesis of mesoporous materials and polymer composite networks using the allyl-modified P123 surfactant, and b) Expanded view of channel interior showing reaction (denoted by green lines) between olefinic ends of neighboring template molecules .....	66
2.3 SAXS data of SBA15P123 and SBA15_aP123, denoted by solid and dotted lines respectively .....	67
2.4 TGA data of SBA15P123 and SBA15_aP123, denoted by solid and dotted lines respectively .....	67
2.5 GPC chromatograms of a) pure P123, b) aP123, c) polymerized aP123, and d) polymer extracted from the composite following polymerization of aP123 template molecules in-situ. No change in molecular weight was observed for control experiments involving pure P123 in the same acid-catalyzed reaction. GPC flow rates were 1 ml/min .....	69
2.6 Solid-state $^1\text{H} \rightarrow ^{13}\text{C}$ CP (cross-polarization)/MAS spectra for (a) the P123 surfactants in normal uncalcined SBA-15 following synthesis, and (b) the organic fraction generated by polymerizing the aP123 structure-directing agents inside and around the SBA-15 following crystallization .....	70
2.7 Pellets formed from (a) polymerized aP123/SBA-15 composite versus (b) versus aP123/SBA-15 without the polymerization step. Both pellets contain ca. 30-33 wt% organic content. (c) Pellet from polymerized composite in $\text{CH}_2\text{Cl}_2$ , at the bottom of the vial, and (d) the corresponding unpolymerized control pellet floating near the surface. The two pellets were placed in each solvent container at exactly the same time, which was 1 minute prior to taking the photo .....	72

3.1 600 MHz <sup>13</sup> C solution NMR spectrum acquired with <sup>1</sup> H decoupling of (bottom) pure P123 starting material and (top) acrylate-functionalized acryP123 following reaction according to Scheme 1. End group signals are shown in the acryP123 inset, exhibiting the characteristic vinyl signals between 120 and 130 ppm.....	81
3.2 600 MHz <sup>13</sup> C solution NMR spectrum acquired with <sup>1</sup> H decoupling of (bottom) pure P123 starting material and (top) styrenate-functionalized styrP123 following reaction according to Scheme 1. End group signals are shown in the styrP123 inset, exhibiting the characteristic styrene between 125 and 140 ppm .....	82
3.3 SAXS data for (a) SBA15P123; (b) SBA15_styrP123; (c) SBA15_styrP123 after polymerization of the astyrP123; (d) same as (a); (e) SBA15_acryP123; and (f) SBA15_acryP123 following polymerization. Diffractograms in (c) and (f) were acquired without calcination, and thus in the presence of the polymer product in and around the silica mesopores .....	86
3.4 Adsorption-desorption curves (on left) and pore size distribution (on right) of SBA15_P123 (a, d); SBA15_acryP123 (b, e); and SBA15_styrP123 (c, f). .....	87
3.5 TEM micrographs for (a) SBA15P123, (b) SBA15_acryP123, and (c) SBA15_styrP123.....	88
3.6 TGA results for polymer nanocomposites made using acryP123 composites with a) 0% b) 10 %; c) 20 %; and d) 70 wt% silica content .....	89
3.7 Images acquired for THF-swollen of polymer nanocomposites using acryP123 (on left) and styrP123 (on right) of a) respective functionalized P123 i.e. acryP123 on left and styrP123 on right b) 0% c) 70 % t; d) 10 %; and e) 20 wt% silica content .....	90
3.8 Solid-state <sup>1</sup> H→ <sup>13</sup> C CP (cross-polarization)/MAS spectra for (a) the acryP123	

template in uncalcined SBA-15 following synthesis but prior to polymerization, (b) the organic fraction generated by polymerizing the acryP123 structure-directing agents inside and around the SBA-15 following crystallization, corresponding to a 30 wt% polymer composite, and (c) same starting material as in (a) but with additional acryP123 added prior to polymerization, resulting in a polymerized composite with 80 wt % organic fraction .....91

3.9 Storage moduli ( $G'$ ) and loss moduli ( $G''$ ) collected from strain sweep (top row) and frequency sweep (bottom row) of acryP123 nanocomposite networks with a) 0%, b) 10%, and c) 20 wt% silica content .....92

3.10 Storage moduli ( $G'$ ) and loss moduli ( $G''$ ) collected from strain sweep (top row) and frequency sweep (bottom row) of styrP123 nanocomposite networks with a) 0%, b) 10%, and c) 20 wt% silica content .....93

4.1 (a) Nitrogen adsorption-desorption isotherm for calcined silica synthesized using the non-ionic PECE-6K template, and (b) pore size distribution for the same material as in (a) .....106

4.2 TEM images for silica templated by (a) the PECE4K macromer and (b) the PECE6K macromer, obtained following calcination to remove the PECE. The open channels/pores appear dark in the image. SAXS results (wavelength = 1.54 Å) for silica (c) templated by PECE4K, and (d) templated by PECE6K .....107

4.3 SEM images for silica templated by the acrylated-PECE6K macromer at (a) 20,000× and (b) 210,000× magnification .....108

4.4 (a) Images acquired for 1,4-dioxane swollen polymerized acrylated-PECE6K (far left) and (proceeding to the right) its 5, 10, and 15 wt% silica nanocomposites following

polymerization. The black mark on each vial indicates the starting volume of the networked material before swelling. (b) Solvent uptake capacities for polymerized pure acrylated-PECE6K and its nanocomposite networks, where solvent uptake capacity is defined as (solvent mass/mass swollen network)\*100 .....110

4.5 Storage moduli ( $G'$ ) and loss moduli ( $G''$ ) collected from strain sweep (top row) and frequency sweep (bottom row) of (◆) polymerized PECE6K; (▲) polymer nanocomposite network with 5, (Δ) 7.5, (●) 10, (○) 12.5 , and (■) 15 wt. % silica content .....112

4.6 Plot of storage modulus  $G'$  (log scale) taken at 1 rad/s versus weight percentage of silica for nanocomposites prepared in-situ using the PECE6K template. Data were acquired at 60°C .....113

4.7 General schematic representation of self-assembly and synthesis of polymer composites using acrylated-PECE macromer templates. After organization of the mesoporous silica matrix occurs, polymerization between PECE macromers takes place within and outside of those particles. The small orange circles in the lower left frame of the reaction scheme are an idealized representation of individual particles in the network, which of course are not regularly arrayed as shown. Cross-linking to form networks occurred due to the reactivity of macromers that contain acrylate groups on both chain ends .....114

## LIST OF SCHEMES

Schemes	Page
2.1 Formation of ester linkage .....	60
2.2 Functionalization of pluronic P123 with allyl group .....	62
2.3 Polymerization of allyl group .....	63
3.1 Reaction scheme for the formation of acryP123 and styrP123.....	79
3.2 Polymerization of acrylic group.....	84
3.3 Polymerization of styrenic group.....	84
4.1 Reaction scheme for formation of triblock copolymer PECE .....	101



## LIST OF ABBREVIATIONS

ATRP	Atom Transfer Radical Polymerization
AIBN	Azo bisisobutyronitrile
BDDT	Brunauer Deming Deming Teller
BET	Brunauer Emmett Teller
BJH	Barrett Joyner Halenda
CP	Cross polarization
CPC	Cetyl pyridinium chloride
CTAB	Cetyl trimethyl ammonium bromide
DGEBA	Diglycidylether of bisphenol A
DSC	Differential Scanning Calorimetry
EISA	Evaporation Induced Self-Assembly
GMA	Glycidyl methacrylate
GPC	Gel Permeation Chromatography
HDPE	High density polyethylene
HMDI	Hexamethylene diisocyanate
IUPAC	International Union Pure and Applied Chemistry
IV	Intrinsic viscosity
KIT	Korea Advanced Institute of Science & Technology
MAS	Magic Angle Spinning
MCM	Mesoporous Crystalline Materials

$M_n$	Number average molecular weight
$M_w$	Weight average molecular weight
NMR	Nuclear Magnetic Resonance
PE	Polyethylene
PECE	poly(ethylene oxide)-b-poly(caprolactone)-b-poly(ethylene oxide)
PEG	Polyethylene glycol
PET	Poly(ethylene terephthalate)
PMMA	Poly(methyl methacrylate)
PNIPAM	Poly(N-isopropyl acrylamide)
PP	Polypropylene
PS	Polystyrene
PVAc	Poly(vinyl acetate)
PVC	Poly(vinyl chloride)
RAFT	Reverse Addition Fragmentation Chain Transfer
RI	Refractive Index
RV	Retention Volume
SAXS	Small Angle X-Ray Scattering
SBA	Santa Barbara Amorphous
SDS	Sodium dodecyl sulfate
$T_c$	Crystallization temperature
$T_g$	Glass transition temperature
$T_m$	Melting temperature
TEOS	Tetraethylorthosilicate
TGA	Thermal Gravimetric Analysis
THF	Tetrahydrofuran

TLCT	True Liquid Crystal Templating
TMOS	Tetramethylorthosilicate
VBC	Vinylbenzyl chloride
ssNMR	solid-state Nuclear Magnetic Resonance

## CHAPTER I

### INTRODUCTION

#### **1.1 Polymer Composites**

Composites are materials that consist of two or more components which are chemically and physically different and are phase separated by a distinct interface. Composites have superior mechanical properties and can be uniquely different than the properties of their constituents. They have found successful application in aircraft structures, electronics, sensors, constructions, coatings, and packaging for biomedical equipment.<sup>1-12</sup> Advantages such as low weight but high mechanical strength, corrosion resistance, durability, high fatigue strength, and faster assembly have made these materials desirable.<sup>11,12</sup>

The two components in composites are matrix and filler, sometimes referred to as the reinforcing agent. The constituent that is continuous and the present in greater quantity is called the matrix. The main purpose of the matrix is to bind and distribute the fillers uniformly such that in the event of external applied force, the force will be distributed evenly.<sup>11,12</sup> Most commonly, one looks at how the matrix properties are improved after incorporation of other constituents. Fillers such as sheets, fibers, or particles are the constituents of the composites which are embedded in the matrix uniformly. In most cases, the fillers are stronger and stiffer than the matrix.

Composites are classified in three categories based on the matrix: ceramic, metal, and polymer matrix composites. The scope of this research is limited to polymer matrix composites. Polymer matrix composites are more popular than ceramic and metal matrix composites due to the ease of fabrication and when fillers are in size of 1-100 nm, they are referred to as polymer nanocomposites. An interesting feature of polymer nanocomposites is the dramatic increase in mechanical properties after the incorporation of small amounts of inorganic fillers.

Several polymer nanocomposites have been synthesized and studied to date for targeted properties and applications by changing polymers with different inorganic fillers such as nanotubes, silicates, nanoparticles of metals, metal oxides, and semiconductors. Polymer silica nanocomposites are most commonly studied in the literature and have numerous applications.

**1.2 Factors affecting the properties of polymer composites.** In addition to the type of fillers and polymers used, factors that also govern the properties of the final polymer nanocomposites are the interaction between the polymer chains and silica particles i.e. interfacial adhesion, the size and geometry of inorganic fillers, and dispersion of fillers into the organic polymer matrix.

### **1.2.1 Interfacial Adhesion**

Since the composites are formed from mixing two components, the resulting properties strongly depends on the interaction of the filler with the matrix. For instance, the large differences in chemical and physical properties of the polymer and silica can often cause an unwanted phase separation leading to poor properties of the polymer silica nanocomposites. To achieve the good mechanical properties the interfacial adhesion should be strong. Effective interfacial adhesion can be brought by either chemical or physical modification to the inorganic fillers.

Chemical modification with modifying agents or grafting polymers leads to strong interfacial adhesion between polymer and silica via covalent bonds. Modifying agents such as silanes are the most effective as they generally possess active functional groups that can interact chemically with polymers. Other modifying agents such as epichlorohydrin, diglycidyl ether of bisphenol A (DGEBA), glycidyl methacrylate (GMA), and octadecylamine have also been used to improve the interfacial adhesion.<sup>13-20</sup> Grafting polymer chains have also been shown to improve the interfacial adhesion between silica and polymer. Zhang and co-workers have used an irradiation technique to graft polymer onto silica and found that the final polymer nanocomposites have increased mechanical properties. Also, the structure-properties relationship can easily be tailored in nanocomposites using grafting technique by changing the polymeric grafting species.<sup>21-28</sup>

Physical modification using surface active agents (also referred as surfactants) have also proven effective in reducing the interfacial tension by adsorption onto the silica. The principle of surfactant treatment is the preferential adsorption of polar head groups onto the silica via hydrogen bonding.<sup>29-32</sup> Reculosa et al., have modified the surface of silica by adsorbing hydrophilic poly(ethylene oxides) via hydrogen bonds with silanol groups of silica.<sup>33</sup>

### **1.2.2 Orientation of inorganic fillers in polymer matrix**

Inorganic fillers can come with defined shapes. For instance, reinforcing silica particles can have an ordered geometric shape, such as spherical, cubic, platelet, or hexagonal.<sup>15,16,34,35</sup> The orientation of these shapes in the polymer matrix can have drastic effects on the properties of the final polymer composites. The improved mechanical property is generally obtained from anisotropic interconnection of filler particles.

### **1.2.3 Dispersion of inorganic fillers into organic matrix**

The simplest method for preparing polymer silica nanocomposites is the direct mixing of silica into the polymer matrix. The effective dispersion of fillers is difficult as they tend to agglomerate in the polymer matrix. Melt and solution blending are the two most commonly used techniques for dispersion of fillers in the polymer matrix.

Melt blending is a mixing of inorganic silica into the molten state of a polymer. The most common polymer matrixes used are polyethylene (PE), polypropylene (PP), poly(methyl methacrylate) (PMMA), polystyrene (PS), poly(vinyl acetate) (PVAc), poly(ethylene terephthalate) (PET), poly(lactide), poly(hydroxyalkanoate), styrene-butadiene rubber, and perfluoropolymer.<sup>36-40</sup> High shear and rate of mixing is important for a homogenous dispersion of silica into the polymer matrix. However, it is difficult to disperse silica into a polymer with a high viscosity i.e. high molecular weight polymer.

Solution blending is a liquid-state powder processing method that results in good molecular level mixing of silica and hence is widely used in material preparation and processing.<sup>8</sup> The polymer is first dissolved in a solvent followed by silica addition into solution while stirring. After removal of the solvent by evaporation, the resulting final polymer nanocomposites exhibits well dispersed silica throughout the polymer matrix.<sup>41-43</sup>

## **1.3 Polymers**

Polymers are macromolecules composed of many small (monomeric) repeating units. Polymers are sometimes also described as high molecular weight substances. Polymers are classified into categories based on occurrence, branching, and polymerization techniques.<sup>44, 45</sup> Polymers can be classified as either naturally occurring polymers or synthetic polymers. Naturally occurring polymers include poly(isoprene), silk, proteins, starches, and cellulose

(shown in **Figure 1.1**). Synthetic polymers include materials such as poly(ethylene terephthalate), poly(vinyl chloride), nylon, and rubbers (shown in **Figure 1.1**).

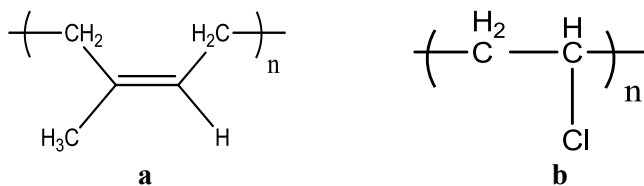


**Figure 1.1.** Chemical structures of **a**) poly(isoprene) a naturally occurring polymer and **b**) poly(vinyl chloride)-synthetic polymers.<sup>44,45</sup>

The properties of polymers are affected not only by their molecular weight, but also the number of branch or linkage in the chain. In other words, the polymer with the same type of monomeric units and molecular weight can have different properties depending upon the branching. The polymers can be classified into four categories based on branching: a) linear, b) branched, c) cross-linked polymers, d) star or dendrimers.<sup>44, 45</sup>

A linear polymer consists of single backbone chain atoms to which the substituents are attached. Polyethylene (PE), poly(vinyl chloride) (PVC), PMMA, and poly(acrylonitrile) are typical examples of linear polymers. These polymers are easily soluble in some solvents. Polymers with branches at intervals along the long polymer chain are referred as branched polymers. The amount of branching affects the physical properties such as solubility, viscosity, and elasticity. Highly branched polymers may swell in certain solvents. High density polyethylene (HDPE) is a typical example of branched polymers. Such materials either swell or do not dissolve in the solvents. The amount by which the polymer swells depends on the degree of cross-linking. Interesting polymeric architecture like star shaped with 5 or 6 arms and tree like structures were synthesized from the multifunctional core (shown in **Figure 1.2**).<sup>44, 45</sup>



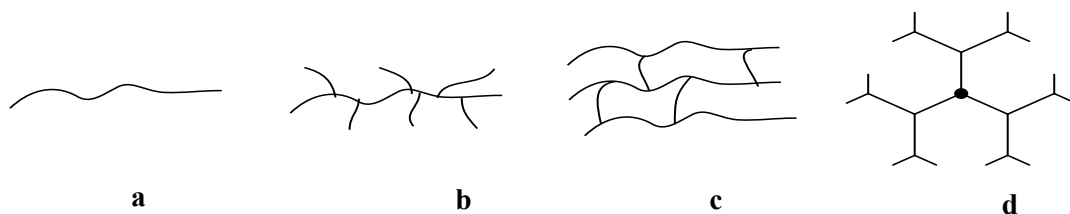


**Figure 1.2.** Different types of branching in polymers: a) linear, b) branched, c) cross-linked, and d) dendrimers.<sup>44, 45</sup>

Polymers can be synthesized in one of two polymerization techniques: condensation or addition. Condensation polymerization occurs when the two or more molecules reacts with each other with the loss of small organic molecules such as water, and ammonia (shown in **Figure 1.3**). Nylon, polyesters, phenol-formaldehyde, urea-formaldehyde, and alkyd resins are the examples of condensation polymers. In this, the reactive functional groups react to form dimer, and dimer reacts with dimers to form tetramers, and so on. As a result, the disappearance of monomer at the early stage is observed and hence results in broad molecular weight distribution.<sup>44, 45</sup>

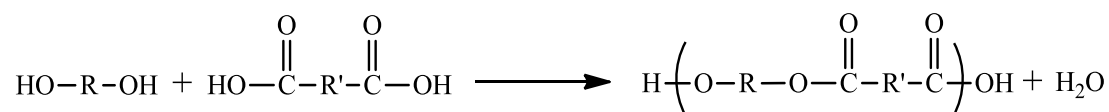


**Figure 1.3.** Condensation polymerization technique for synthesis of polyesters.<sup>44, 45</sup>

In addition polymerization, macromolecules are formed from linking the monomeric species without the loss of any organic molecules. This polymerization involves the breaking of pi bonds followed by the formation of sigma bonds between the monomers. This polymerization has three steps: Initiation, propagation, and termination (shown in **Figure 1.4**). Firstly, the monomer species are initiated followed by propagation in which the monomers are added to the chain and finally termination occurs when the two free radical reacts together to form a covalent bond.

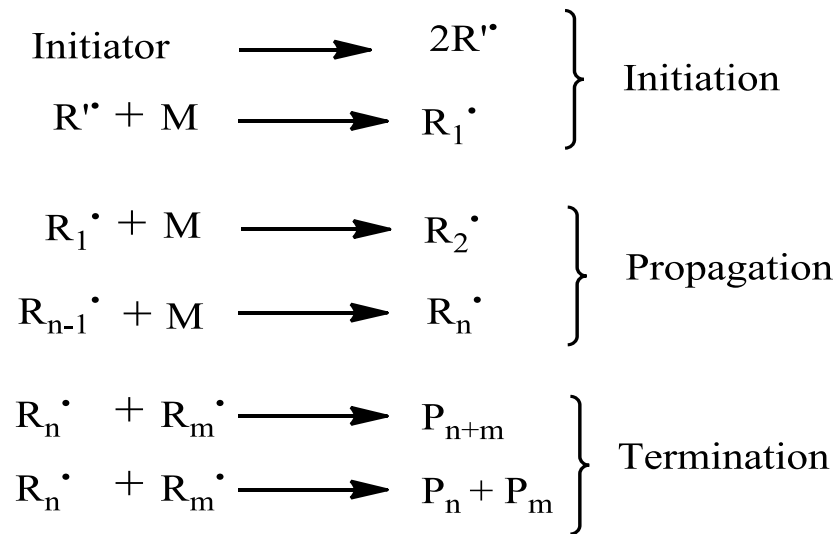


**Figure 1.4.** Free-radical polymerization sequence.<sup>44, 45</sup>

Addition of the monomers is not only restricted to one specific type of monomer. Polymers with two or more different types of monomers are called copolymers. For example, if styrene and acrylonitrile are allowed to polymerize, it will result in a long chain of polymer consisting of both monomer species. Such arrangements of monomers lead to four different types of copolymers: a) random copolymers, where monomers ‘A’ and ‘B’ are randomly distributed throughout the polymer chain b) alternating copolymers where the two monomers are arranged in a regular alternating sequence throughout the polymer chain, c) block copolymers where a block of monomer ‘A’ is connected to a block of monomer ‘B’, and d) gradient copolymers where a gradual change occurs in monomer composition from mostly monomer ‘A’ to mostly monomer ‘B’ in the polymer chain (shown in **Figure 1.5**). The arrangements are tailored on the basis of reactivity ratios and sequential addition of monomers.

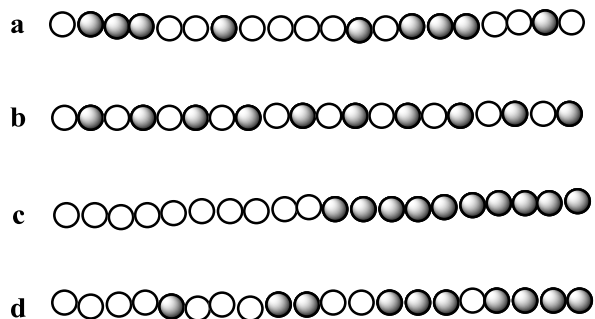


**Figure 1.5.** Arrangements of monomers to form: **a)** random, **b)** alternating, **c)** block, and **d)** gradient copolymers.<sup>44, 45</sup>

Telechelic polymers such as graft copolymers were developed over the course of research in designing polymer architecture. In these copolymers, the polymer from monomer B is grafted onto the polymer chain length of A as shown in the **Figure 1.6**.

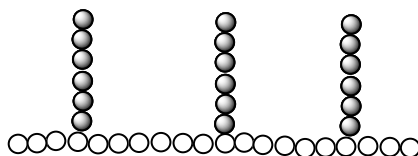


**Figure 1.6.** Schematic representation of graft copolymers.<sup>44, 45</sup>

There are two classes of polymers based on their behavior when exposed to heat. The thermoplastic softens and will melt when heated.<sup>44, 45</sup> Hence, one can easily change the shape of thermoplastic materials. Polystyrene, polyethylene, polypropylene, and any linear polymers are examples of thermoplastic polymers. Thermosetting polymers are cross-linked polymers and hence rigid. Once shaped, such polymers cannot be re-shaped. Phenol-formaldehyde and polyurethane are examples of thermosetting resins.

The distinguishing features of polymers are molecular weight and glass transition temperature ( $T_g$ ). Small organic molecules have definite molecular weight, whereas polymers do not. Given a polymeric sample, it will have different chain lengths produced from the initiator

radicals depending on the degree of polymerization.<sup>44, 45</sup> Hence, molecular weights of polymers are usually reported as averages. Experimentally determined molecular weight averages for polymers are: number average molecular weight ( $M_n$ ), weighted average molecular weight ( $M_w$ ), viscosity average molecular weight ( $M_v$ ), and z-average molecular weight ( $M_z$ ). Out of those the two most commonly reported are  $M_n$  and  $M_w$ . They are calculated from the equations **1** and **2**.<sup>44</sup>

,45

$$M_n = \frac{\sum N_i M_i}{\sum N_i} \quad (1)$$

$$M_w = \frac{\sum N_i M_i^2}{\sum N_i M_i} \quad (2)$$

where,  $M_n$  is the number average molecular weight,  $M_w$  is the weight average molecular weight,  $N_i$  is the number of repeating units, and  $M_i$  is the molecular weight of each repeating unit.

The polydispersity index, defined as the ratio  $M_w/M_n$ , is a measure of molecular weight distribution. If the polydispersity index is close to 1, then the molecular weight distribution is narrow (shown in **Figure 1.7a**). This occurs in addition polymers. A broad molecular weight distribution is generally observed when the polydispersity index is above 2 (shown in **Figure 1.7b**). This occurs in condensation polymers.

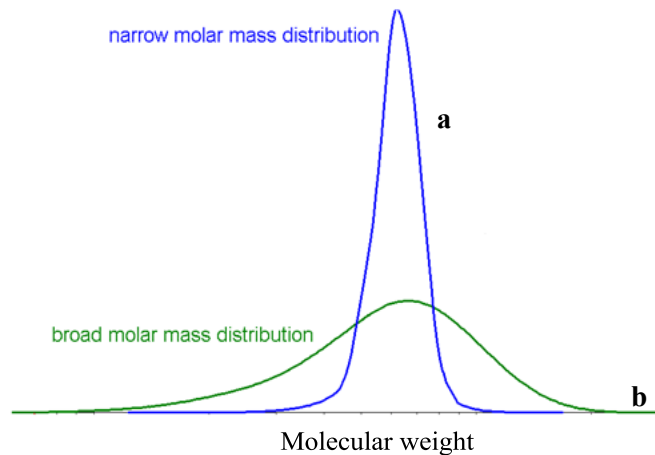


**Figure 1.7.** Molecular weight distributions: **a)** narrow and **b)** broad.<sup>44,45</sup>

Most polymers have amorphous and crystalline regions. What differs is the percentage of each region in the polymer chains. A single polymer occurs in different forms glassy or rubbery depending on the temperature. The temperature above which it is rubbery and below which it is glassy in state is called as glass transition temperature ( $T_g$ ). For instance, the glass transition temperature of polystyrene is  $90^\circ\text{C}$ . The polystyrene if used below its  $T_g$  will behave like a rigid glass as the structural mobility of amorphous domains are restricted. Conversely, if it is used above  $T_g$  the polymer chains will have some degree of movement and hence will behave like rubber. Therefore, linear polymers possess  $T_g$  as they possess free chains, whereas highly crosslinked or thermoset polymers do not.<sup>44,45</sup>

#### **1.4 Properties of polymer composites**

Polymer and polymer composites are well known for light weight but high mechanical strength. One can easily extract the mechanical properties from the stress-strain plot. Stress is the force applied per unit cross-sectional area, while strain is the response of the sample under a given stress. The typical stress-strain curve and commonly used shape of specimen for characterizing mechanical properties of polymer or polymer composites are shown in **Figure 1.8**.

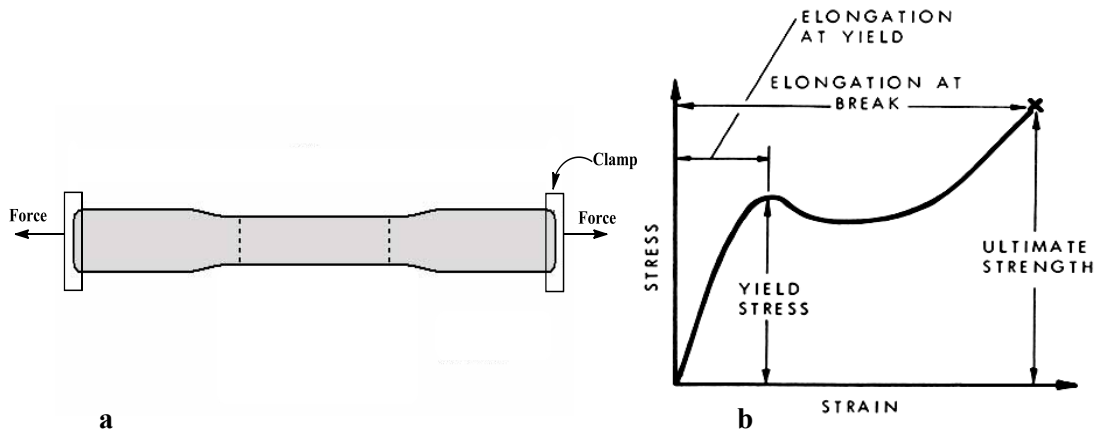


**Figure 1.8.** a) Dumbbell shaped polymer/ polymer composites specimen and b) typical stress-strain curve for polymers.<sup>44, 48</sup>

Young's modulus which is the ratio of stress to strain is a measure of stiffness. The toughness is the measure of resistance to breaking. The tensile strength (also referred to as Ultimate strength) is the maximum stress the material can withstand. For instance, if the material is soft, then it will yield more. If the material is brittle it will yield less. **Figure 1.6** shows the characteristic stress-strain curves of five different types of materials.

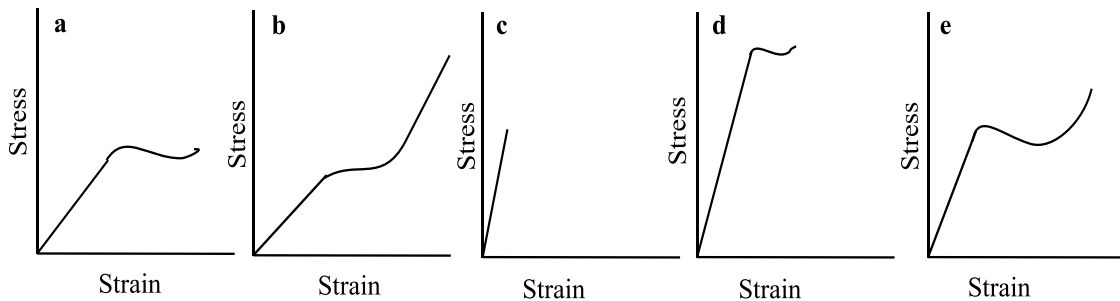


**Figure 1.9.** Stress-strain curves of a) Soft and weak, b) soft and tough, c) hard and brittle, d) hard and strong, and e) hard and tough polymeric materials.<sup>44, 45</sup>

## 1.5 Mesoporous Silica

This dissertation focuses on using mesoporous silica as inorganic filler. The most generalized definition of a porous material is a continuous and solid network of material filled with voids. Nanoporous materials are less than 100 nm in pore diameter. According to IUPAC nomenclature, the pores are classified into three categories based on the size: a) micropores (pore diameter less than 2 nm, b) mesopores (pore diameter between 2 nm and 50 nm), and c) macropores (pore diameter more than 50 nm). Pores can also be classified based on their framework: a) purely inorganic, b) organic-inorganic hybrid, and c) purely inorganic (shown in **Figure 1.10**).

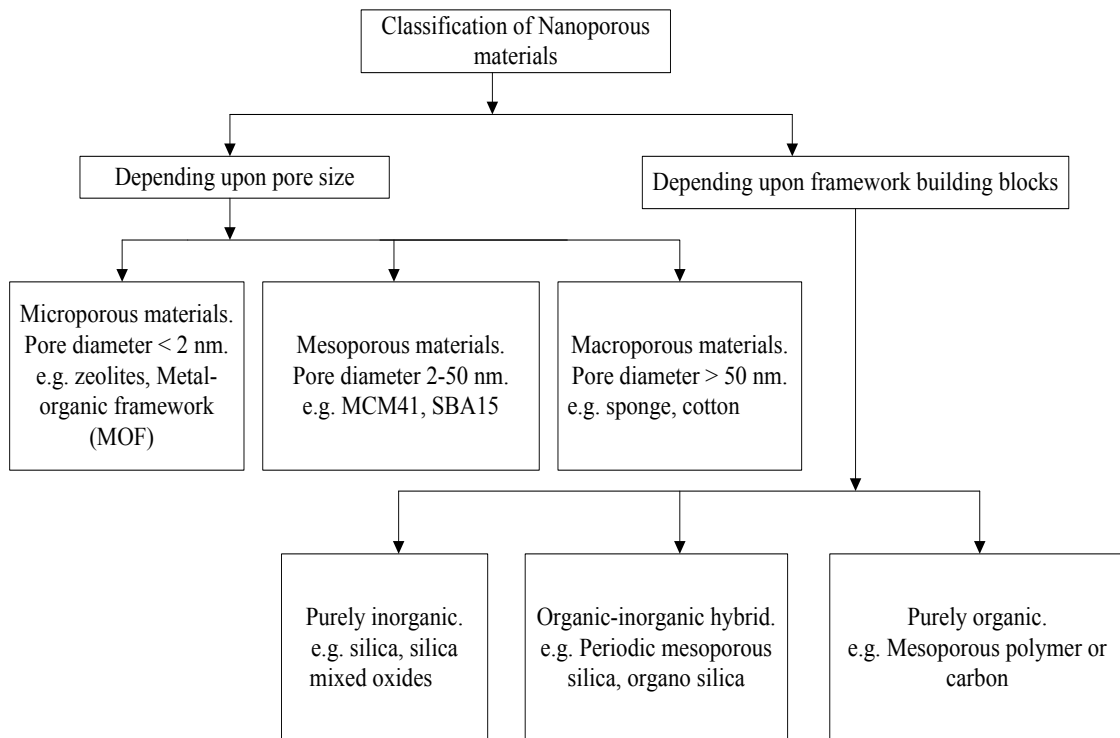
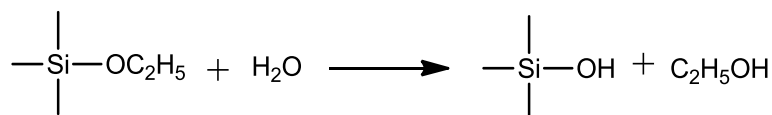


**Figure 1.10.** Classification of nanoporous materials.<sup>49</sup>

Mesoporous materials can be ordered or disordered in nature. The hydrolysis and polycondensation reactions of the silica precursors to synthesis mesoporous silica are the same

that occur in sol-gel process. Disordered mesoporous silica like KIT-1 (Korea Advanced Institute of Science and Technology number 1) has uniform channels but a disordered shape as the result of uncontrolled sol-gel reactions. Controlled polycondensation using the surfactant assisted self-assembly pathway leads to ordered mesoporous silica, having a defined shape with uniform and regular arrangements of pores. Hydrolysis of an alkoxy group attached to silica results in hydroxyl silica species. These hydroxylated silica species, upon condensation by reacting with either the hydroxyl group or the alkoxy of the other silica species, results in the formation of silica.

**Hydrolysis:**



**Condensation:**

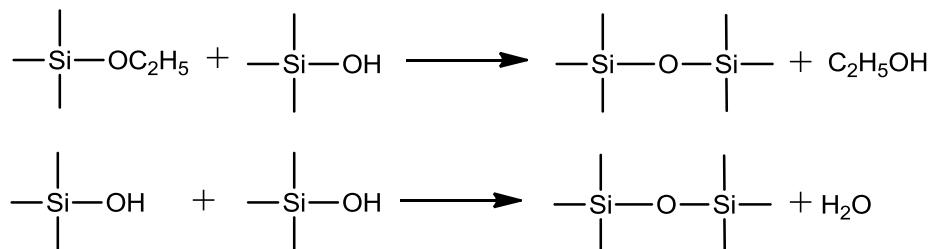


**Figure 1.11.** Sol-gel hydrolysis and condensation reactions.<sup>50-53</sup>

Surfactants have both hydrophobic and hydrophilic components. It controls the sol-gel reactions (shown in **Figure 1.11**) and can tune the size, shape, and ordered arrangement of pores. In aqueous solution, the hydrophilic part of surfactants interacts with the water whereas the hydrophobic part stays away from the water molecules. Beyond some concentration, the surfactants arrange as micelles in either 3D spherical or 2D rod like arrays; such concentration is called as critical micelle concentration. This arrangement of micelles helps in pore generation.



Surfactants are classified into three categories depending upon the charge: a) cationic such as cetyl trimethylammonium bromide (CTAB), cetyl pyridinium chloride (CPC); b) anionic such as sodium dodecyl sulfate (SDS), lauric acid; and c) Non-ionic (pluronic P123, F127).<sup>49</sup>

Interactions between inorganic components and organic templates are among the most important thermodynamic drivers that usually determine the feasibility of mesostructure formation and its topology. Each of the four electrostatic interactions given below can occur under a wide range of pHs, temperatures, and the type of surfactant used. The interactions are:  $S^+I^-$ ,  $S^-I^+$ ,  $S^-M^+I^+$ , and  $S^+X^+I^-$  where S is the surfactant, I is the inorganic phase, M is the intermediate ion, and X is the mediating species (shown in **Figure 1.12**).<sup>50-55</sup> The charge on the inorganic species has to be controlled by pH. The pH at which the charge of molecules is zero is called isoelectric point. The isoelectric point of silica species is 2. Silica species has positive charge at  $pH < 2$ , whereas  $pH > 2$  silica has negative charge. **Figure 1.13** below shows the hydrolysis and condensation of silica precursors under different pH conditions.

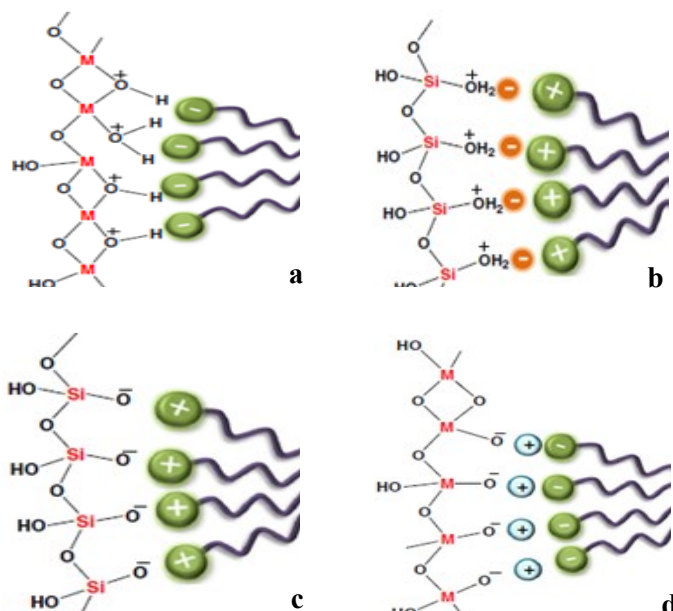


**Figure 1.12.** Types of electrostatic interactions: a)  $S^+I^-$ , b)  $S^+X^+I^-$ , c)  $S^-I^+$ , and d)  $S^-M^+I^+$  that can occur between surfactant and silica species.<sup>49</sup>

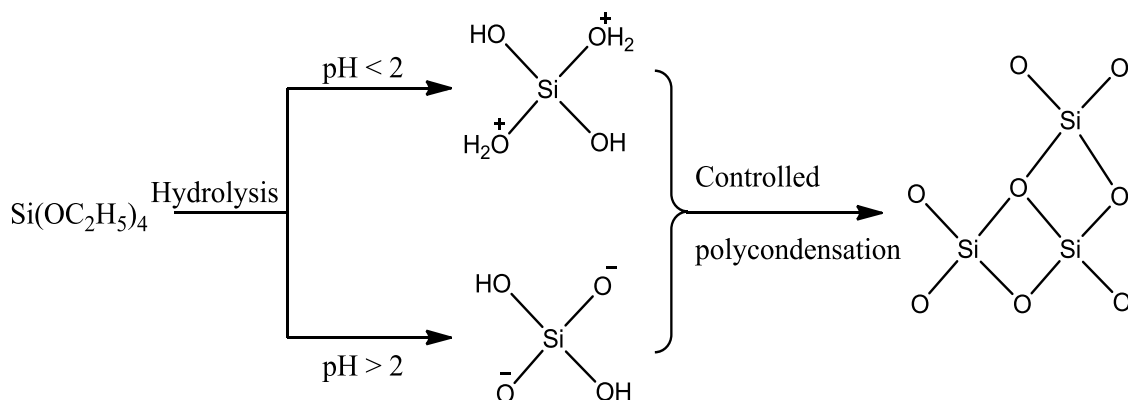


**Figure 1.13.** Silica precursors under different pH.<sup>49</sup>

The first mesoporous silica MCM41 (Mesoporous Crystalline Materials) prepared by Mobil Oil Corporation scientists in 1992 was synthesized at basic condition, where silica species have negative charge using cationic surfactant CTAB via  $\text{S}^+\text{T}^-$  interaction.<sup>56, 57</sup> Che et al., synthesized silica using organoalkoxy silane with quaternary ammonium silica as a co-structure directing agent via  $\text{S}^+\text{T}^-$  interactions.<sup>58</sup> Mesoporous silica MCM41 has high surface area ( $>1000 \text{ m}^2/\text{g}$ ), with hexagonal pores and thinner walls. Due to the thinner walls, they do not have good hydrolytic stability. As a result, many researchers investigated strategies to make thicker walls. In 1998, Stucky and co-workers synthesized mesoporous silica SBA15 with thicker walls, 2D hexagonal pores, and high surface area using a non-ionic surfactant through  $\text{S}^+\text{X}^-\text{T}^+$  interactions.<sup>59</sup>

To date, four routes have been successfully developed leading to mesoporous silica are true liquid crystal templating (TLCT), co-operative self-assembly, evaporation-induced self-assembly (EISA), and exo-templating. All of these routes were developed in order to tune the pore size and ordered framework of silica/other meso-structured materials.

### 1.5.1 True Liquid Crystal Templating (TLCT)

MCM41 mesoporous family is not only the first reported mesoporous silica materials with mesophases, but also with well-ordered hexagonal silica channels. MCM41 attracted many scientists to understand the mechanism of its formation. In this mechanism, liquid crystal mesophases are involved in the surfactant self-assembly to synthesized ordered mesoporous silica. Attard and coworkers proposed and observed that at high concentration of surfactant and under specific pH and temperature conditions, the cylindrical rod like micelles lyotropic liquid-crystalline mesophases are formed without requiring the presence of inorganic precursors to get the mesostructure framework (shown in **Figure 1.14a**).<sup>60</sup> Deposition followed by condensation of inorganic species onto and in between the rod-like micelles results in the composite materials where organic surfactant lies inside the mesostructured silica. Pores are obtained by removing the surfactant. Calcination is the thermal treatment to remove surfactant by oxidative decomposition.<sup>54, 58, 61-63</sup> Solvent extraction is another process to remove surfactant from mesophases of silica.

### 1.5.2 Co-operative Self-Assembly

The TLCT mechanism can be applied where the surfactant concentration is high. However, the mesoporous silicas are also formed at very low concentration of silicate and surfactant in strongly basic conditions. Therefore, an alternative mechanism was proposed where the formation of cylindrical micelles of surfactant, adsorption of the silica species, and condensation of silica precursors occurs at the same time (shown in **Figure 1.14b**).<sup>54, 58, 61-63</sup> Steel et al. confirmed the formation of highly ordered mesoporous silica using <sup>14</sup>N nuclear magnetic resonance (NMR spectroscopy).<sup>64</sup> They proposed that the hexagonal mesophases of surfactant molecules were organized after the incorporation of siliceous species.

There are reports on the mechanism of mesoporous silica formation using experimental techniques like X-ray diffraction combined with  $^{29}\text{Si}$  magic-angle spinning (MAS) solid state NMR spectroscopy.<sup>65</sup> Huo et al., proposed that under basic conditions, the negatively charged silica ( $\Gamma$ ) bind to the cationic head groups of the surfactant. The  $\text{S}^+\text{T}$  interactions lead to thermodynamically favored lamellar configurations at the early stages followed by polycondensation of the silicate species and solidification of the layers resulting in hexagonal mesophases.

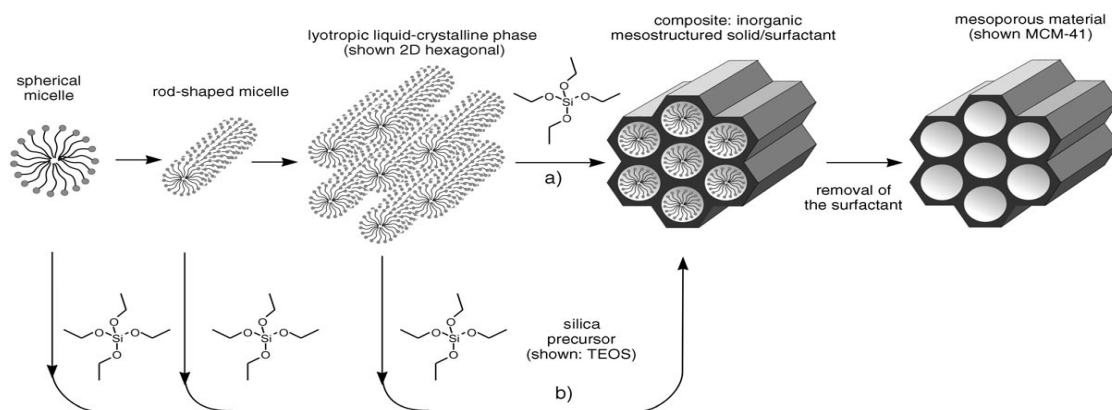


**Figure 1.14.** Mechanism of mesoporus silica formation by a) true liquid crystal templating and b) co-operative self-assembly routes.<sup>55</sup>

### 1.5.3 Evaporation-Induced Self-Assembly (EISA)

As the name suggests, this method is based on the formation of meso-structured phases by evaporating volatile solvents from dilute solutions containing silica precursors and surfactant. Brinker et al. have reported the mesostructured silica thin films using TEOS and poly(styrene)-b-poly(ethylene oxide) diblock copolymers via the EISA approach.<sup>54, 58, 61-63</sup> In this method surfactant, inorganic species and silica precursors are allowed to interact in the presence of solvent such as tetrahydrofuran (THF) or ethanol (shown in **Figure 1.15**). The mesostructured film was then cast by evaporation of the solvent. The film consisting of inorganic-organic hybrid mesophases which is formed after evaporation of solvent is flexible due to low degree of polycondensation of inorganic species. Hydrothermal treatment of such soft materials leads to

ordering of the organic-inorganic framework. This route is also used for synthesis of non-silica based mesoporous silica. Li et al. have synthesized 2D hexagonal mesoporous silica and phenolic resins using amphiphilic poly(ethylene oxide)-b-poly(caprolactone) diblock copolymer.<sup>66a, 66b</sup>

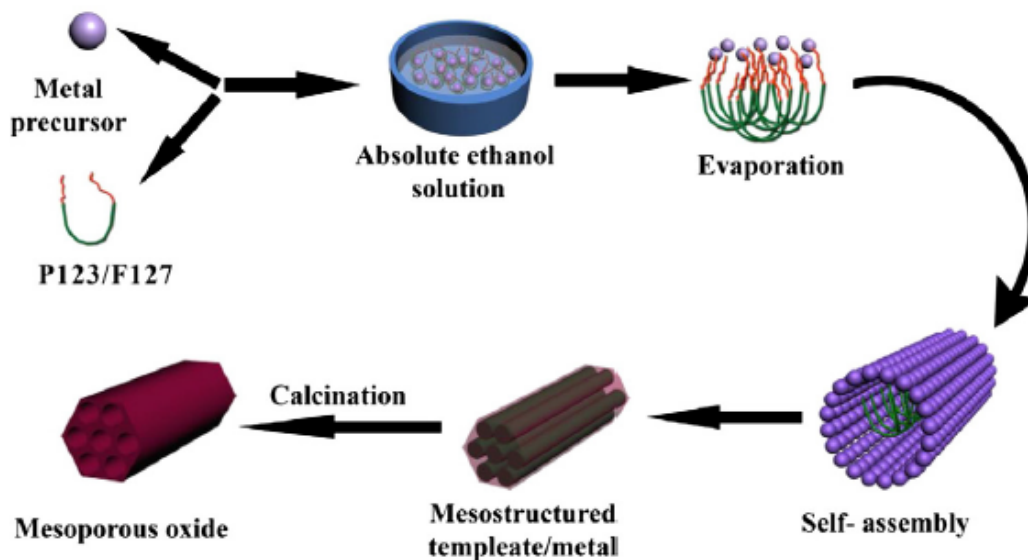


**Figure 1.15.** Schematic representation of EISA approach.<sup>49</sup>

#### 1.5.4 Exo-templating route

Mesoporous organic polymer resins, carbons and other metal oxides are synthesized via exo-templating methods. This route is also known as hard-templating or nano casting method. In this method, the mesoporous matrix is used as a template. The spaces of such templates are first impregnated by inorganic/organic precursor, followed by curing the precursor inside the template at high temperature. In this way, the pores of the template are copied as a negative image (shown in **Figure 1.16**). Upon removal of the template, the cured material possesses high surface area and shape as the template used. Ryoo et al. synthesized mesoporous carbon by exo-template route.<sup>54, 58, 61-63</sup> They used mesoporous silica MCM41 as the exotemplate and then filled the pores with sucrose and sulfuric acid as the catalyst in aqueous solution. Upon curing at high temperature, sucrose was converted into carbon. Removal of the mesoporous silica template resulted in a

mesoporous carbon which had an identical shape as that of MCM41. Recently, many metal oxides have been synthesized using this method.

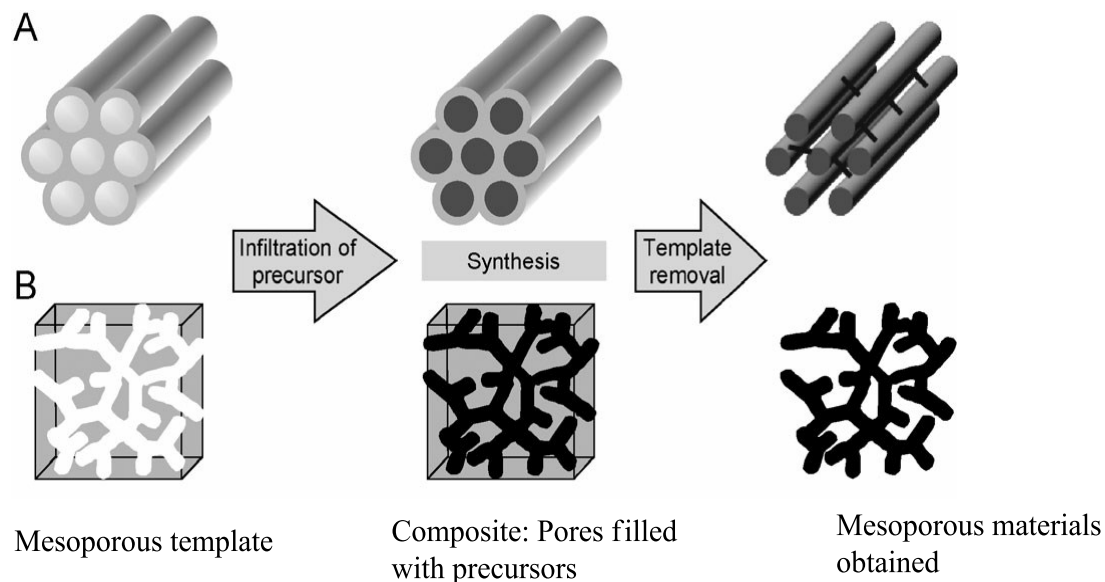


**Figure 1.16.** Schematic representation of exo-template approach for mesoporous materials.<sup>54,58,</sup>

61-63

## 1.6 Motivation

Since the publication of the first paper on ordered hexagonal mesoporous silica MCM41 in 1992 by Mobil Oil Corporation Scientists,<sup>56,57</sup> attracted material scientists to use it as inorganic filler in polymer nanocomposites. Because mesoporous silica possess high surface area, ordered structure, and allows ease of functionalization of the nanopores, mesoporous silica polymer nanocomposites have found application in catalysis, drug delivery, sensor technology, and gas storage.<sup>67-70</sup> Following any of the four mechanism described in section 1.5; mesopores of silica can be tailored to spherical, cubic, or hexagonal shapes depending on structure directing agents and reaction conditions (shown in **Figure 1.17**).

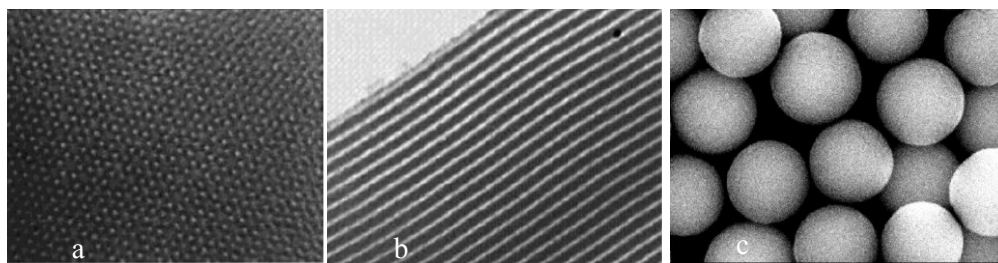


**Figure 1.17.** TEM images of mesoporous silica pores of a) cubic, b) hexagonal, and c) SEM image spherical shapes.<sup>71, 72</sup>

**Figure 1.18** illustrates that there is a dramatic increase in interest on studying polymer silica nanocomposites as compared to polymer mesoporous silica nanocomposites. A major problem for use of mesoporous silica in synthesizing polymer nanocomposites is difficulty of filling pores with polymers.

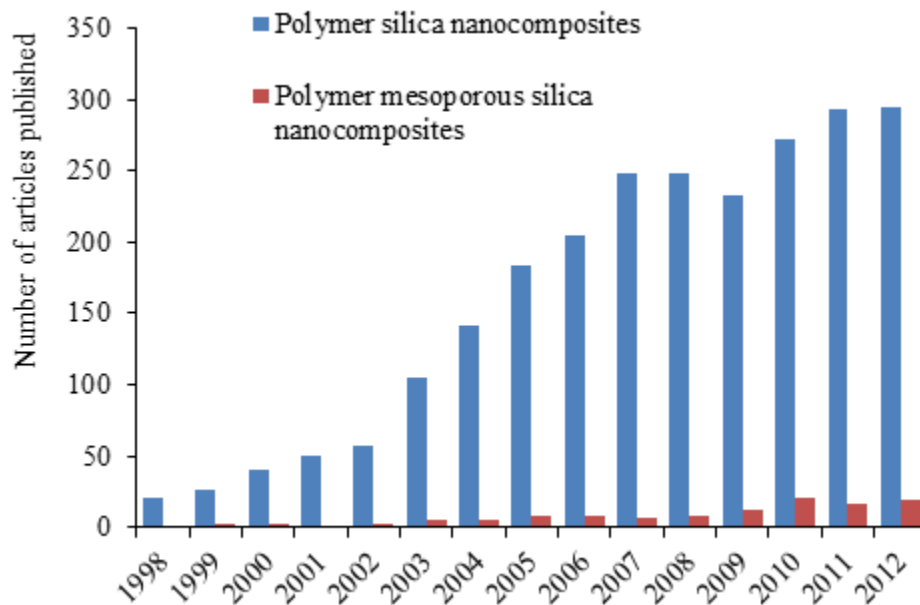


**Figure 1.18.** Comparison of articles published on a) polymer silica nanocomposites and b) polymer mesoporous silica nanocomposites from 1998 to 2012. The data is extracted from scifinder.

Mesoporous silica MCM41 possess pore diameter from 2-10 nm, with high surface area, and thinner silica walls. Thinner walls of MCM41 yield polymer nanocomposites with poor

mechanical properties. Hence limit its use in synthesizing polymer nanocomposites. There have been many attempts to synthesize mesoporous silica with thicker walls. In 1998, Stucky et al., reported mesoporous silica SBA15 (Santa Barbara Amorphous 15) with thicker walls, two dimensional hexagonal pores, and a high surface area using non-ionic surfactant.<sup>59</sup> Such unique pores provide scaffolds for the fabrication of hybrid organic-inorganic nanocomposites. There are three approaches to synthesize polymer nanocomposites using mesoporous silica as filler: 1) co-condensation, 2) post-synthetic functionalization (also known as grafting), and 3) the sol-gel method.

### **1.6.1. Co-condensation Method**

In this method, organically modified mesoporous silica is synthesized by the co-condensation of tri-alkoxyorganosilanes [ $R'Si(OR)_3$   $R'$  being the monomeric unit] with tetra-alkoxyorganosilanes [ $Si(OR)_4$ ] in the presence of structure directing agents. Polymerizing the organic group results in polymer nanocomposites networks wherein mesoporous channels are filled with polymers. Ji et al. have synthesized poly(propyl methacrylate) mesoporous silica nanocomposites using (3-Trimethoxysilyl)propyl methacrylate.<sup>73</sup> These composites have shown improved tensile strength, modulus, and toughness resulted from chemical bonding of silica with polymer chains within mesoporous silica channels. Schematic representation of synthesizing polymer nanocomposites using co-condensation is shown in **Figure 1.19**.



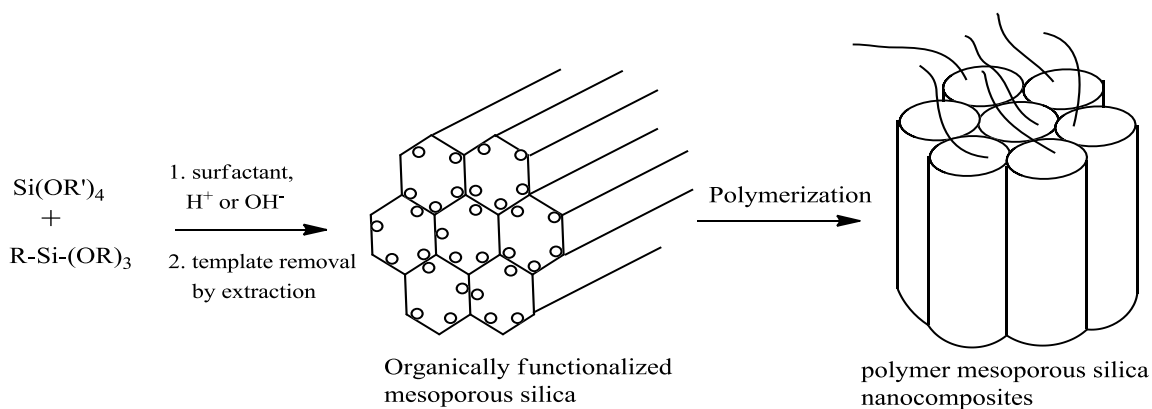


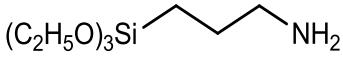
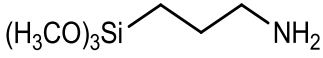
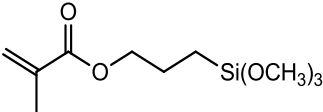
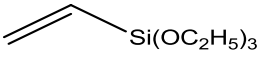
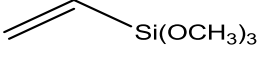
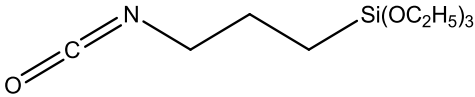
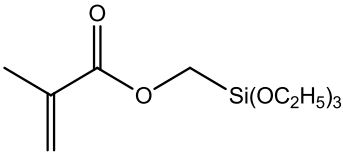
**Figure 1.19.** Mesoporous silica/polymer nanocomposites by co-condensation approach.<sup>73</sup>

The groups of Mann, Macquarrie, and Stein have shown the possibilities of modified mesoporous silica using co-condensation method with different organic groups.<sup>55, 74, 75</sup> The organic groups such as amino, cyano, vinyl, allyl, organophosphine, alkyl, thiol, or aromatic groups can be incorporated in the pores of mesoporous silica using silane coupling agents.<sup>55, 76</sup>

**Table 1.1** shows typical silane coupling agents. Polymerization of vinyl acetate, styrene, methyl acrylate, and acrylate has been carried out in the pore channels of the mesoporous silica.

In addition to a being one-pot synthesis, this method has the advantage of strong covalent chemical bonding of filler with the polymer matrix resulting in improved mechanical properties. However, the increase in the density of the organic groups inside the pores will disrupt the ordered mesoporous silica. Thermal treatment to create the pores will destroy the organic groups and hence the pores have to be generated by solvent extraction.

**Table 1.1.** Silane coupling agents.<sup>8, 55</sup>

	Name	Structure
1.	3-aminopropyltriethoxysilane	
2.	3-aminopropyltrimethoxysilane	
3.	3-trimethoxysilylpropyl methacrylate	
4.	Vinyltriethoxysilane	
5.	Vinyltrimethoxysilane	
6.	3-isocyanatopropyltriethoxysilane	
7.	Methacryloxymethyltriethoxysilane	

### 1.6.2. Post-functionalization

Grafting refers to surface modification of mesoporous silica with organic groups. Exploiting the hydroxyl groups in the pores of mesoporous silica, one can easily connect the ATRP/RAFT initiator leading to preparation of polymer nanocomposites by two routes: “grafting to” and “grafting from”. The “grafting to” refers to the attachment of polymers to mesoporous silica, but also some generates non-grafted chains.

Mesoporous silica MCM41 composites with polystyrene, polyacrylonitrile, PMMA, polypeptide, and PNIPAMM have been synthesized using a “grafting from” controlled radical polymerization method.<sup>77-80</sup> The initiator is attached to the mesoporous silica, followed by the

polymerization of the monomeric species. Since, the initiator is attached after the pores have been created; thermal calcination is not an issue. However, if the organic group (i.e. monomers) is large and reacts preferentially during the initial stages of modification near the opening of the pores of the mesoporous silica, pore blocking may occur which can in turn lead to inhomogeneous distribution of organic groups over the mesoporous silica channels. The schematic representation of post-functionalization is shown in **Figure 1.20**.

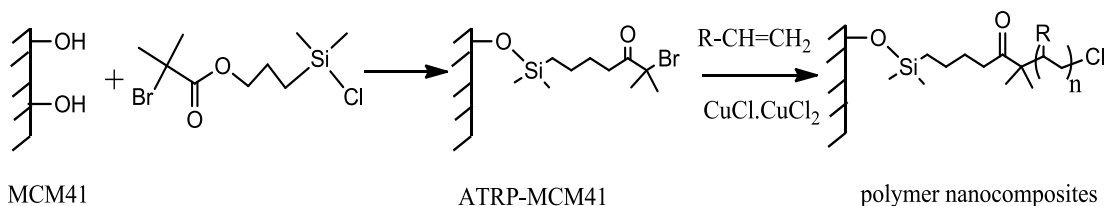


**Figure 1.20.** Mesoporous silica/polymer nanocomposites using post-functionalization approach.<sup>81</sup>

### 1.6.3. Sol-gel method

In this method, the monomer or polymer is well dispersed in the silica precursor (TEOS or TMOS) which after hydrolysis and polycondensation of the silica precursor results in the polymer nanocomposites. This chemistry is performed in any one of the following polymerization techniques: emulsion, emulsifier-free emulsion polymerization, mini-emulsion and dispersion.<sup>8</sup>

Polymerization techniques mentioned above result in homogeneously dispersed silica into the polymer matrix. Unlike co-condensation or post-synthetic functionalization, the silica is not covalently linked to the polymer. Networks formed between the two components are due to strong hydrogen-bonding interaction. The hydrogen bonding reduces interfacial tension between the two components which retards phase separation during network formation. Most of the polymers like PMMA, PVAc, poly(hydroxystyrene), and poly(vinylpyrrolidone) interact with the inorganic phases, but when the monomer or polymer does not possess these groups to interact

with silica via hydrogen bonding, compatibilizers are added.<sup>8, 81, 83</sup> **Figure 1.21** shown below represents the synthesis of polymer nanocomposites via the sol-gel method.

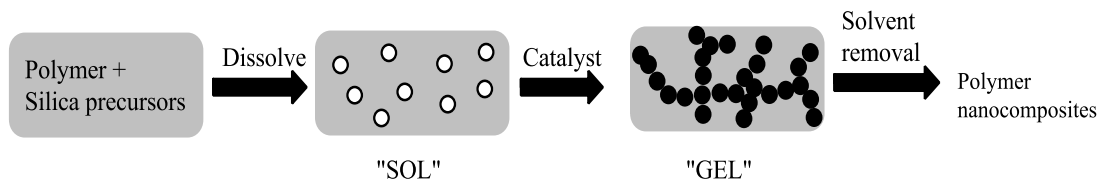


**Figure 1.21.** Polymer nanocomposites using the sol-gel approach.

In previous research, our group synthesized polymer mesoporous silica nanocomposites using grafting approach. We successfully loaded tin catalyst on the mesoporous silica channels of MCM41 via hydroxyl groups. Ring opening polymerization of D,L-lactide monomer was employed in the presence of a tin catalyst resulting in the biopolymer nanocomposites from inside to outside of the MCM41 silica channels. The schematic diagram of synthesis of biopolymer composites is shown in **Figure 1.22**.

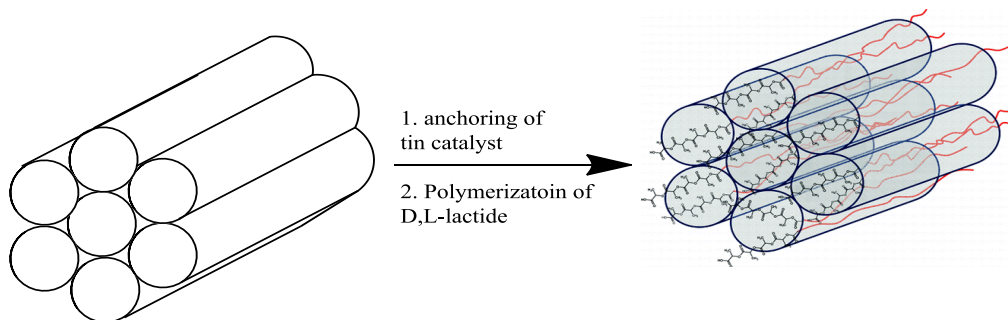


**Figure 1.22.** Schematic representation of ring-opening polymerization of D,L-lactide inside the mesoporous silica.<sup>84</sup>

Whilst most of the approaches discussed above produce polymer nanocomposites retaining the mesostructure of the silica, they involve three or more steps in generating polymer nanocomposites or networks. Even the one-pot co-condensation approach can only incorporate a small percentage of monomers inside the mesoporous silica channels. These limitations motivated

the need of a new strategy for synthesizing biopolymer nanocomposites with a reduced number of steps while retaining the internal surface area of mesoporous silica.

### 1.7 Approach

The efforts made so far in synthesizing mesoporous silica reinforced polymer nanocomposites were focused on functionalizing the pore walls with organic components which upon polymerization results in nanocomposites. Here we propose an alternative approach of synthesizing the polymer nanocomposites, focusing on functionalizing structure directing agents used for preparing the mesoporous silica with polymerizable organic components. Such polymerizable structure directing agents, also referred as “surfmers” are chemically composed of hydrophobic, hydrophilic, and monomeric units (either on the chain ends or on the backbone of surfactants). The concept of functional and reactive surfactants is not new in the field of micelle polymerization, but their successful application to the synthesis of ordered siliceous-based composite materials has been limited to small-molecule ionic templates.

Surfmers template the growth of inorganic species ( $\text{SiO}_2$ ) by a co-operative self-assembled approach resulting in mesostructured silica channels similar to SBA15 as discussed in section 1.5. Before calcination, all silica based mesophases are organic-inorganic composite materials. Polymerizing the surfmers at this stage results in mesoporous channels filled with polymer that extends out, connecting other silica particles leading to intimately mixed nanocomposite networks that cannot phase separate. The schematic representation of this strategy is shown in **Figure 1.23**. Unlike previous reports, there is no chemical grafting to the interior or exterior of the mesoporous silica surface, nor is there any separation of the components at any time during the synthesis.

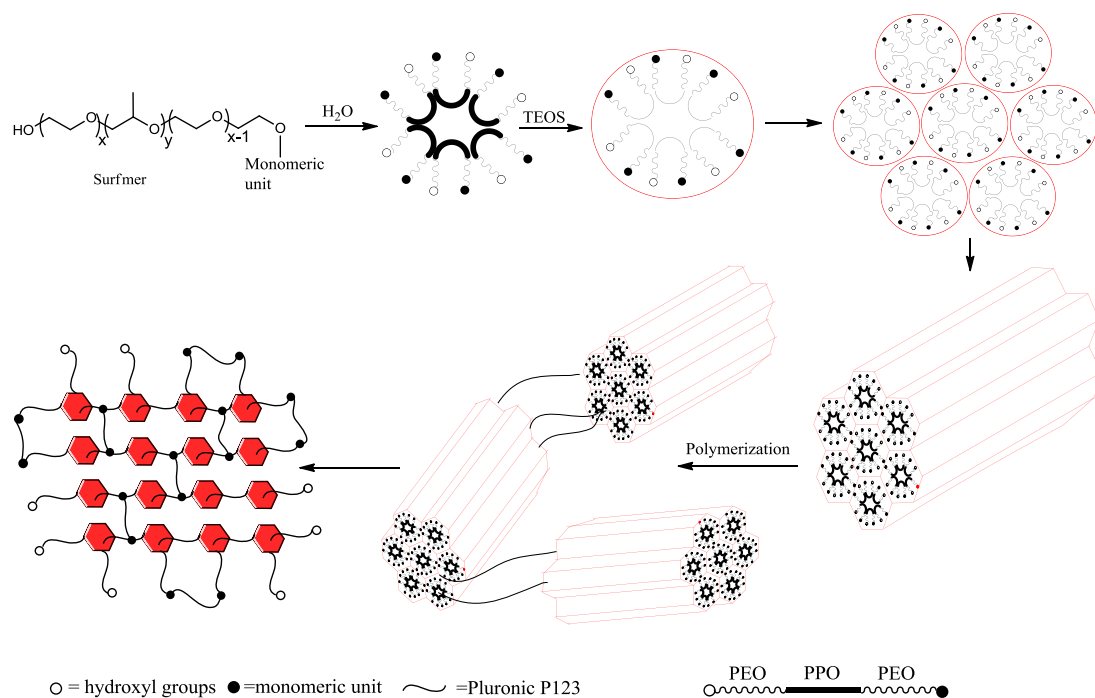


**Figure 1.23.** Schematic representation of polymerizable structure directing agent approach for the synthesis of polymer mesoporous silica nanocomposites.

## 1.8 Research Objectives

This dissertation focuses on the synthesis of polymer mesoporous silica nanocomposites and their networks using a polymerizable structure directing approach which fulfills the following two objectives.

**Objective 1:** The key component of the research is the polymerizable structure directing agents that can template the growth of silica. This objective aims at synthesizing two different polymerizable structure directing agents (surfmers) by end-group functionalization of approximately one of the chain ends of: a) poly(ethylene oxide)-b-poly(propylene oxide)-b-poly(ethylene oxide) triblock copolymer (pluronic P123), or b) poly(ethylene oxide)-b-poly(caprolactone)-b-poly(ethylene oxide) triblock copolymer with monomeric units (allylic, acrylic, or styrenic).

**Objective 2:** This objective aims at synthesizing mesoporous silica using surfmers synthesized in objective 1, by co-operative self-assembly approach. At this stage, the mesoporous silica developed has organic component (surfmer) inside the pores of silica. Polymerizing the surfmer will generate the biodegradable nanocomposite networks wherein mesopores are completely filled with polymer; and whose total organic/inorganic ratio may be controlled

## **1.9 Experimental Techniques**

Mesoporous silica and polymer nanocomposite networks synthesized are characterized by variety of experimental techniques as described below.

### **1.9.1 Physisorption experiments**

Physisorption, also known as physical adsorption, is a process in which molecules get adsorbed onto the substrates by means of van der Waals forces of attraction. This technique is used to characterize the type of pores, surface area, pore size distribution, and wall thickness of the substrate without damaging the substrate.

Samples must be degassed to remove any moisture in order to properly determine the surface area and adsorption-desorption profile of nitrogen gas. This is usually done by heating at higher temperature (generally 100°C) under reduced pressure for several hours in the glass-bulb sample holder. A glass rod is inserted in the sample holder to avoid any artifacts caused by dead volume. The measurement is performed at low temperature using liquid nitrogen in order to provide a strong physical interaction between the gas molecules and the substrate. The adsorbate (nitrogen gas) is then inserted in the sample holder using calibrated piston and the amount of gas adsorbed-desorbed is collected with respect to relative pressure. The schematic representation of the experiment is shown in **Figure 1.24**.

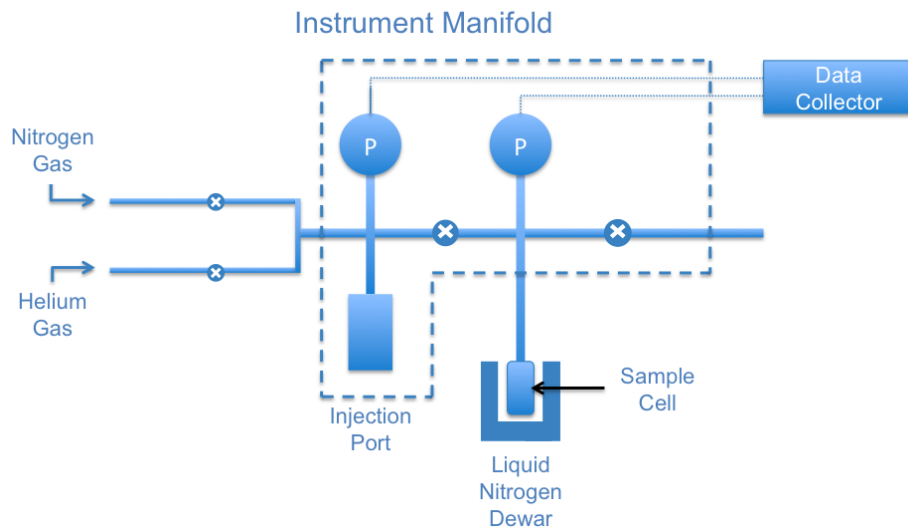


**Figure 1.24.** Schematic representation of physisorption experiments.<sup>84</sup>

### A) Adsorption Isotherm

An adsorption isotherm is the quantitative relationship between the amount of gas adsorbed by unit mass of substrate (the adsorbent) and the relative pressure ( $p/p_0$ ) of the gas at constant temperature. According to the Brunauer, Deming, Deming, and Teller (BDDT) IUPAC classification IUPAC nomenclature (1984), the adsorption isotherms are classified into six different types as shown in the **Figure 1.25a**.

Type I isotherm is characteristic of microporous adsorbents. At low relative pressures, micropores are being filled as seen by a steep increase in the amount of gas adsorbed. After the pores are filled completely, the entire surface of adsorbent is covered by gas as seen by the horizontal plateau. Type II isotherm is characteristic of non-porous adsorbents. Type III and V isotherms are uncommon. An increase in the amount of adsorbed gas takes place at a higher relative pressure, which is caused by very weak interactions between the adsorbent and adsorptive. Type VI represents an isotherm of stepwise multilayer adsorption of uniform non-porous adsorbents.<sup>87-88</sup>



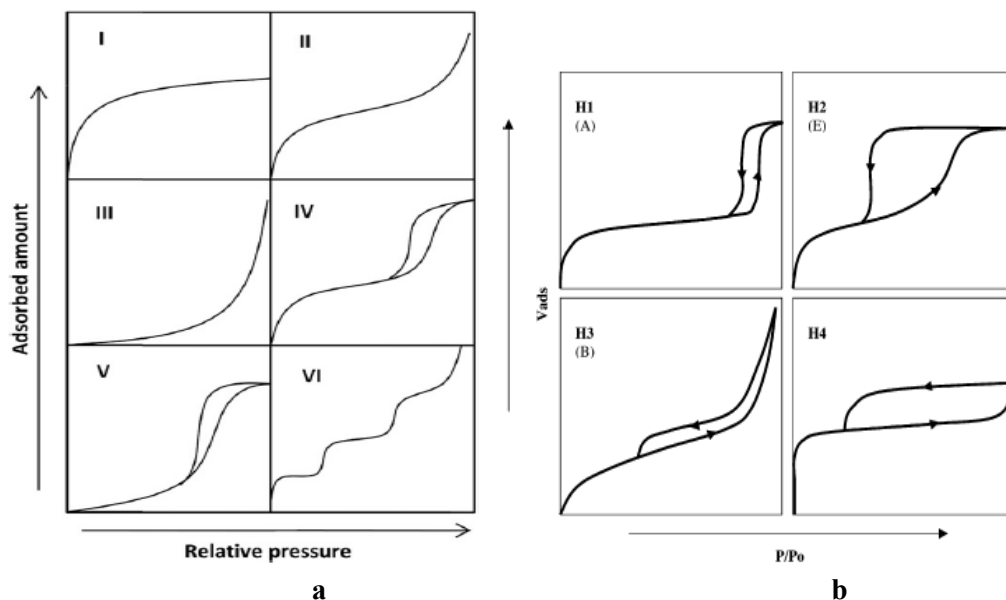


**Figure 1.25.** a) Isotherms and b) hysteresis loop of type IV isotherm.<sup>86</sup>

The most common hysteresis loop observed in the case of mesoporous substrates is H1, with fewer exhibiting H2 loop, and H3 is observed rarely. Mesoporous silica shows Type IV H2 loop indicating even pores with interconnecting channels. H4 hysteresis loop is often seen in narrow slit-like pores.

### **B) Surface Area Determination: BET Theory**

The theory is named after the three scientists Brunauer, Emmett, and Teller. It is a modification of Langmuir adsorption isotherm. Following are the assumptions of BET theory:<sup>85</sup>

- 1) Adsorption of the first adsorptive layer is assumed to take place on an array of surface sites of uniform energy.
- 2) Adsorbate layers stack one above the other. When,  $p = p_0$  (the saturated vapor pressure of the adsorptive), an infinite number of layers will form.
- 3) At equilibrium, the rates of condensation and evaporation are the same for each individual layer.
- 4) No interactions exist between the adsorbate molecules.

The surface area of the adsorbent is determined by the following BET equation 3.

$$\frac{1}{W \times \left( \left( \frac{p}{p_o} \right) - 1 \right)} = \frac{1}{W_m \times C} + \frac{C-1}{W_m \times C} \times \left( \frac{p}{p_o} \right) \quad (3)$$

Plotting a graph of  $\frac{1}{\left( \frac{p}{p_o} \right) - 1}$  with respect to relative pressure (shown in **Figure 26**), one

will get the slope ( $s$ ) and intercept ( $i$ ) which corresponds to equation 4.  $W_m$  (amount of monolayer adsorbed gas) can be calculated from equation 4. The specific surface area ( $S$ ) are calculated from equation 5.

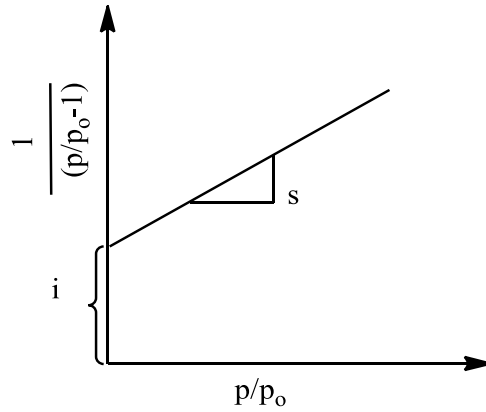


**Figure 1.26.** Typical BET plot.<sup>85</sup>

$$s = \frac{C-1}{W_m \times C} \quad \text{and} \quad i = \frac{C-1}{W_m \times C} \quad (4)$$

$$S_t = \frac{W_m \times N \times A_{cs}}{M} \quad (5)$$

Note that, ' $s$ ' and ' $i$ ' are the slope and intercept respectively. ' $S_t$ ' is the total surface area, ' $W_m$ ' is the amount of monolayer adsorbed gas, ' $N$ ' is the avogadro's number, ' $A_{cs}$ ' is the cross-sectional area of the adsorbate (nitrogen) which is  $16.2 \text{ \AA}^2$  for nitrogen gas, ' $M$ ' is the molecular weight of

nitrogen, and 'w' is the weight of the sample. The specific surface area is calculated from total surface area as shown in equation 6.

$$S = \frac{S_t}{w} \quad (6)$$

### 1.9.2 Differential Scanning Calorimetry (DSC)

DSC is a technique to determine the temperature at which the local segmental motions of polymeric chains can occur. Thermal properties of polymers such as glass transition temperature ( $T_g$ ), melting temperature ( $T_m$ ), and crystallization temperature ( $T_c$ ) can be determined using DSC. The schematic representation of the DSC instrument and the typical DSC thermogram are shown in **Figure 1.27** and **1.28** respectively. The pan that contains a polymer is referred to as “sample pan” whereas the one without the polymer is referred to as “reference pan”. In DSC experiments, the sample and reference pans are heated at the same rate and at the same time. The difference in the heat flow of sample and reference pans are recorded and plotted as the function of temperature.

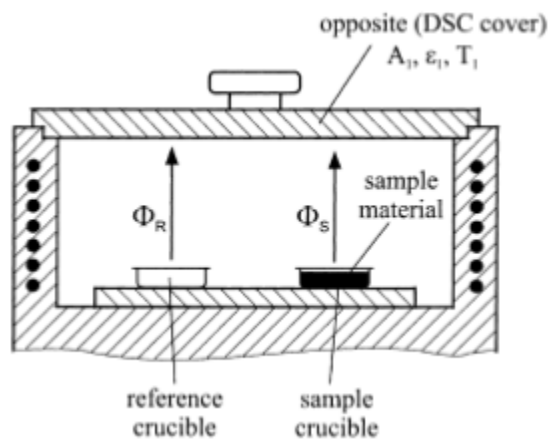


**Figure 1.27.** Schematic representation of DSC cell.<sup>89</sup>

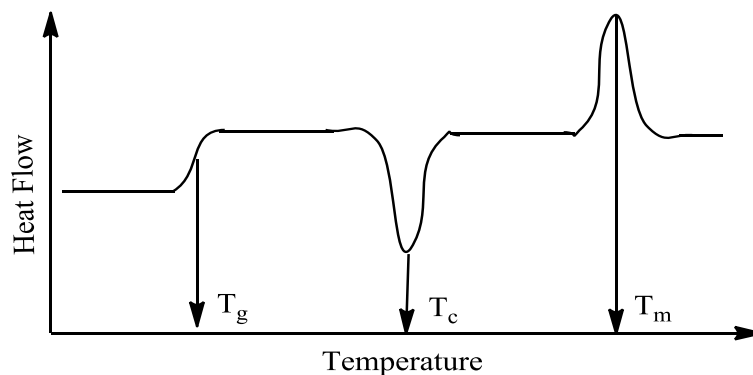


**Figure 28.** Typical DSC thermogram.<sup>90</sup>

To extract the information from thermogram, one should know the first order and second order transition. The first order transition is the transition which involves both latent heat (heat given off or absorbed) and heat capacity. Polymers melt by absorbing heat and therefore melting is an endothermic process. Polymers crystallize by giving off heat and therefore are an exothermic process. The second order transition involves only the change in heat capacity such as glass transition temperature. As polymers have high heat capacity at the glass transition temperature, therefore the small increase in temperature will increase the heat flow.

### 1.9.3 Thermal Gravimetric Analysis (TGA)

Thermal gravimetric analysis is useful particularly in determining the percentage of organic content in polymer nanocomposites. In this method, the mass loss is determined as the function of temperature using high precision balance. The typical TGA thermogram is shown in **Figure 1.29**. TGA is equipped with the balance that keeps that track of mass loss during the degradation of polymer or any organic materials is with respect to temperature. In some cases, materials are decomposed in the presence of inert atmosphere to eliminate the formation of side products. The typical experiment consists of three steps: a) the aluminum pan is tared on the balance, b) sample is transferred on the pan which is then loaded on balance, and c) sample is then heated from room temperature to 600°C at 20 °C per minute under air flow.

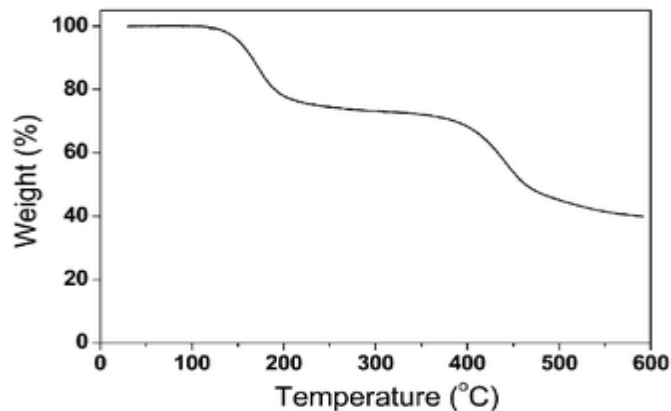


**Figure 1.29.** The typical TGA thermogram.<sup>91</sup>

#### 1.9.4 Gel Permeation Chromatography (GPC)

Gel permeation chromatography, also referred to as “Size-Exclusion Chromatography”, is the separation of polymers on the basis of size. GPC has become most prominent and widely used method for estimating molecular weights and their distributions. It is an indirect method of determining  $M_n$  and  $M_w$  of the polymers. Often, the separation takes place in a chromatographic column made from highly crosslinked porous polystyrene, but other column types are also available.<sup>44, 45</sup>

A schematic representation of a typical GPC instrument is shown in the **Figure 1.30**. GPC consists of 1) a pump which pushes the solvent into the instrument, 2) an injection port to introduce the sample into the column, 3) columns to hold the stationary phase, 4) one or more detectors (generally refractive index detectors) to detect the polymeric components as they leave the column, and 5) software to control the different parts of the instrument, calculate, and display the results.

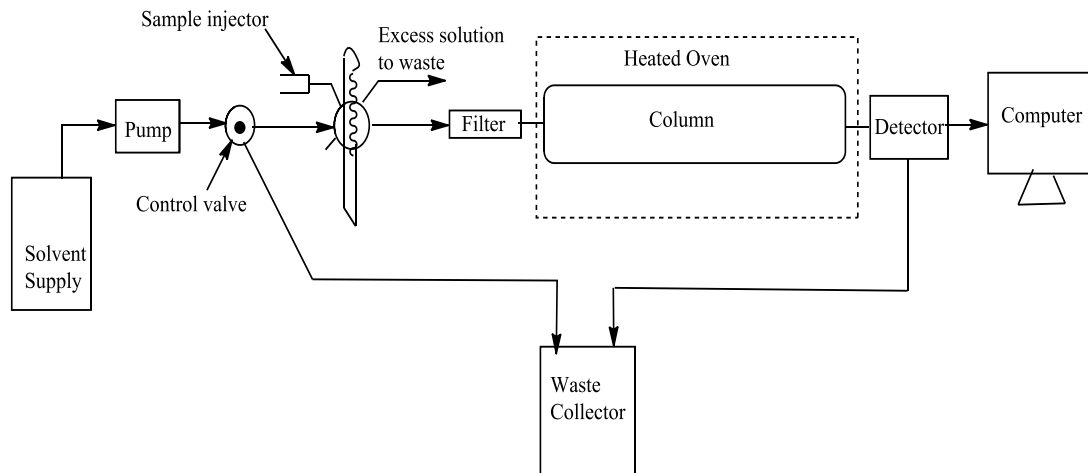


**Figure 1.30.** Schematic representation of Agilent 1100 series Gel Permeation Chromatography.

The instrument used in this research is an Agilent Technologies 1100 series. The calibration curve (molecular weight vs elution time) is plotted using the six different molecular weights of polystyrene or poly(ethylene oxide) standards whose polydispersity index is close to 1.0 (shown in **Figure 1.31a**). The procedure is as follows: 1) Inject the series of standards polymer, 2) Measure the retention volume of the resulting RI peak apex, 3) Construct a calibration curve of  $\text{Log}(\text{MW} \cdot \text{IV})$  vs. retention volume. In the analysis of our unknown sample, each data point (retention volume, RV) we can look up on the calibration curve to find  $\text{RV}_i = \text{Log}(\text{MW}_i \cdot \text{IV}_i)$ . Where,  $\text{RV}_i$ ,  $\text{MW}_i$ , and  $\text{IV}_i$  are the retention volume, molecular weight, and intrinsic viscosity of the unknown polymer. The polymer solution is then introduced into the columns. Intrinsic viscosity (IV) is measured by viscosity detector coupled with refractive index detector.

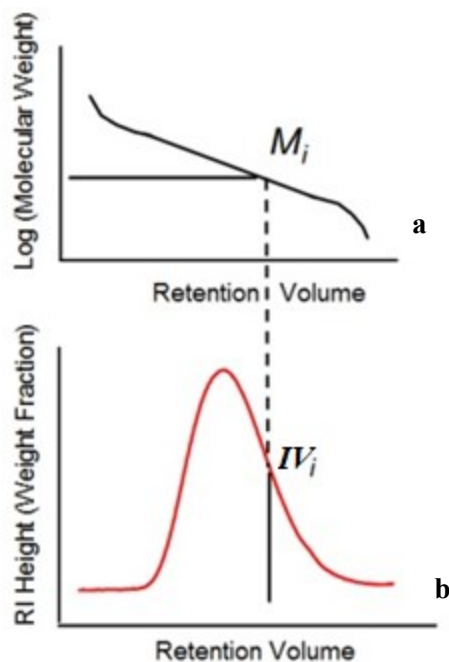


**Figure 1.31.** a) Calibration curve using polystyrene standards and b) GPC chromatogram of unknown sample.<sup>92</sup>

### 1.9.5 Rheology

Rheology is the study of deformation and flow of matter. It helps in understanding the material behaviors such as elastic, viscous, or viscoelastic. The polymeric materials are viscoelastic, in other words they show both elastic and viscous behaviors. In order to extract the information from the rheological experiments, the terms such as stress and strain are important to understand. The stress is the applied force per unit area of the sample whereas; strain is the ratio of change in length to the original length of the sample.

The elasticity deals with the mechanical properties of solid where the stress ( $\sigma$ ) is proportional to strain ( $\epsilon$ ) which obeys the Hooke's law. Viscosity deals with the properties of liquids where stress ( $\sigma$ ) is proportional to the shear rate ( $\dot{\eta}$ ) as which obeys the Newton's law. The viscoelastic behavior of the polymers is explained by spring and dashpot model (shown in **Figure 1.32**). If they are placed in series, the resulting *Maxwell element* exhibits flow plus elasticity on

the application of stress. When the stress is applied, the spring elongates while the dashpot slowly yields and on the removal of the stress the spring recovers but the dashpot does not. The resulting strain is given by the equation 7.

$$\frac{\partial \varepsilon}{\partial t} = \frac{1}{E} \frac{\partial \sigma}{\partial t} + \frac{\sigma}{\eta} \quad (7)$$

(Hooke) (Newton)

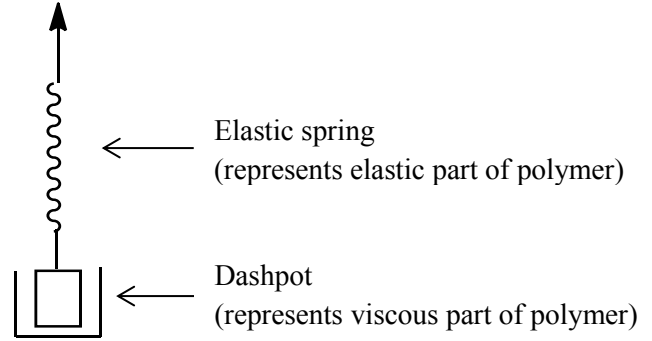


**Figure 1.32.** Mechanical analog of a viscoelastic liquid.<sup>93</sup>

The schematic representation of the rheometer is shown in **Figure 1.33**. The rheometer can be equipped with either cup-cone plate or parallel plates. In this research, the Rheometric Scientific RSA-II rheometer equipped with parallel plates is used to characterize the storage ( $G'$ ) and loss modulus ( $G''$ ) of the crosslinked polymer nanocomposites networks. The sample with circular disc of length ( $l$ ) and radius ( $r$ ) was used for rheological testing. It is placed in between the two parallel plates and then the experiments are performed. Parameters such as stress, strain, storage modulus ( $G'$ ), loss modulus ( $G''$ ) are calculated from the equations 9 to 11.<sup>94</sup>

$$Stress = \frac{2 \times Force \times length}{\pi r^3} \quad (8)$$

$$Strain = \frac{3 \times displacement \times radius}{(length)^2} \quad (9)$$

$$G' = \left( \frac{Stress}{Strain} \right) \times \cos \delta \quad (10)$$



$$G'' = \left( \frac{\text{Stress}}{\text{Strain}} \right) \times \sin \delta \quad (11)$$

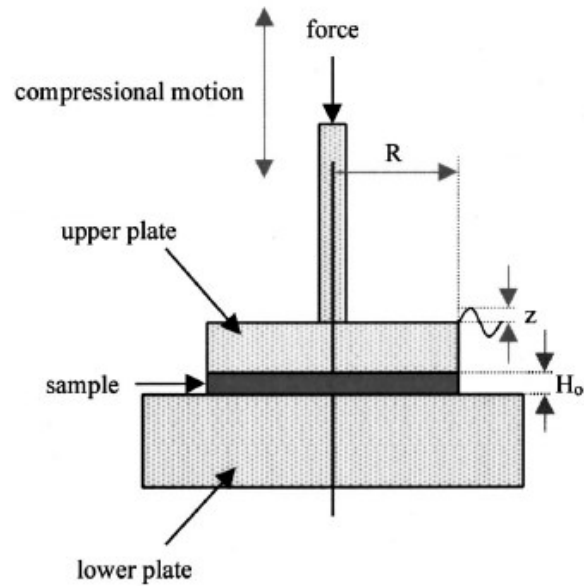


**Figure 1.33.** Schematic representation of parallel plates used in Rheometric scientific RSA II.<sup>94</sup>

Viscoelastic properties are investigated using rheological experiments such as strain sweep, frequency sweep, or temperature sweep. Strain sweep are the experiments where  $G'$  and  $G''$  are measured as the function of strain at constant frequency and temperature. Frequency sweep are the experiments where  $G'$  and  $G''$  are measured as the function of frequency at constant strain and temperature. The linear viscoelastic region is determined by performing the strain sweep and then frequency sweep data is collected to calculate the storage modulus ( $G'$ ) and loss modulus ( $G''$ ). The polymer behavior can be easily predicted from the logarithmic plots of storage and loss modulus as the function of frequency.

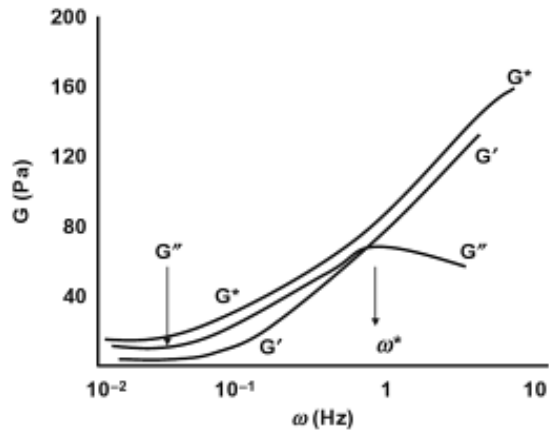


**Figure 1.34.** Plot of  $G'$  with respect to frequency of a viscoelastic material.<sup>93</sup>

If  $G' < G''$  at low frequency, then polymer dissipates energy and behaves as viscous liquid. If  $G' > G''$  at higher frequency, then the polymer becomes more rigid and behaves as elastic (shown in **Figure 1.34**). In crosslinked polymer,  $G'$  and  $G''$  are independent of the frequency indicating perfect network formation. The tan delta which is the ratio of loss modulus to storage modulus describes the balance between viscous and elastic behaviors of polymer.

### 1.9.6 Small Angle X-Ray Scattering (SAXS)

SAXS is a non-destructive technique to characterize materials (in solid, liquid, or gels) for crystallite structure, size, and recognition of amorphous phases. **Figure 1.35a** shows the typical schematic representation of SAXS. When monochromatic wavelength of x-rays hits the sample, it generates the scattered rays. The intensity of the scattered rays is collected as the function of scattering angle  $2\theta$ . These scattered rays create constructive interference that satisfies the Bragg's Law ( $n\lambda = 2d \sin \theta$ ; where  $n$  is an integer,  $\lambda$  is the wavelength of the incident light,  $d$  is the spacing between the planes of atomic lattices, and  $\theta$  is the angle between the incident rays and the scattering planes). The plot of scattered intensity versus scattering angle obtained is then compared with the International Centre for Diffraction Data database. **Figure 1.35b** shows the interaction of x-rays with the sample.

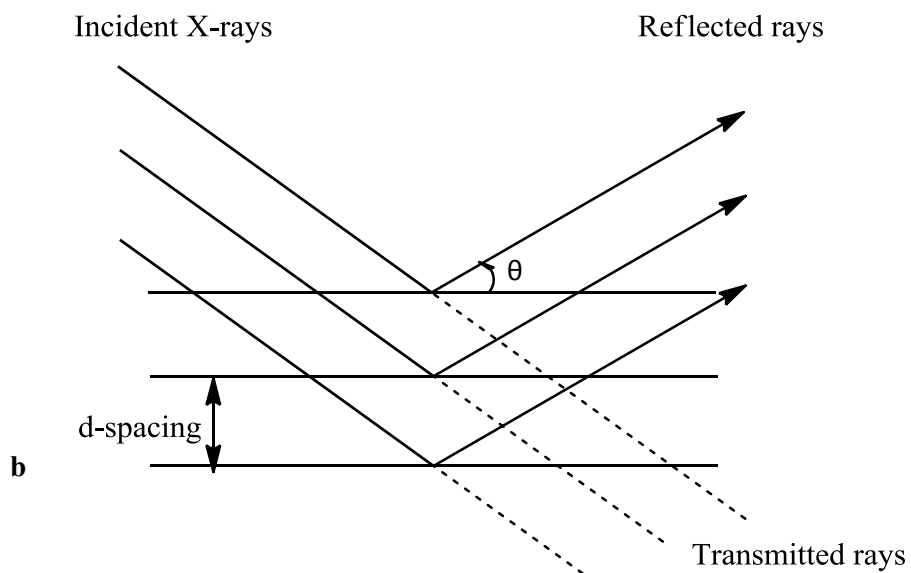
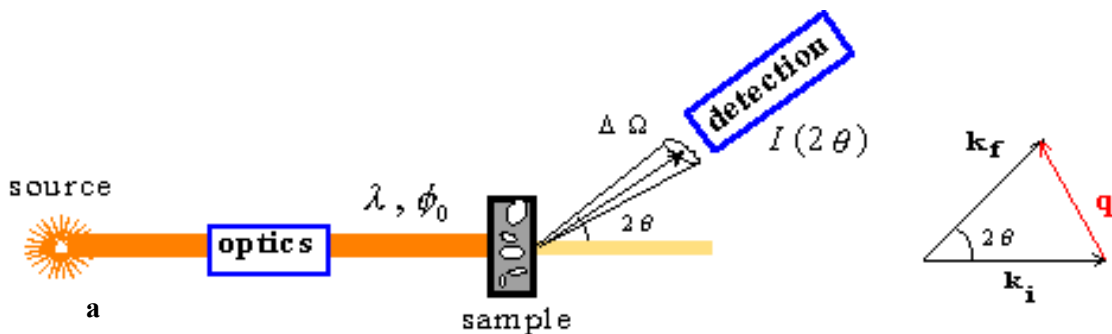


**Figure 1.35.** Schematic representation of **a)** SAXS instrument and **b)** diffraction of rays from sample.<sup>95</sup>

### 1.9.7 Nuclear Magnetic Resonance

NMR is the powerful analytical tool to determine the chemical structure. It was co-discovered by Bloch and Purcell, who received Nobel Prize in 1952 for detecting the protons signals from water and paraffin wax respectively. In NMR, the experiments are performed on the nuclei of atoms with angular momentum ( $\hbar \hat{I}$ ); therefore the magnetic moment ( $\mu$ ) is calculated by equations 12 and 13.

$$\mu = \gamma \hbar \hat{I} \quad (12)$$

$$\mu = \gamma \hbar m_s \quad (13)$$

where,  $\gamma$  is the magnetogyric ratio and is constant for each nucleus,  $\hat{I}$  is the nuclear spin (unobservable),  $m_s$  is spin quantum number, and  $\hbar$  is the planck's constant.

Nuclei with overall nuclear spin ( $\hat{I}$ ) not equal to zero are called as spin active nuclei. Quantum mechanics tells that the nuclear spin ( $\hat{I}$ ) will have  $(2\hat{I} + 1)$  orientations. In the absence of external magnetic field, these orientations are of equal energy. When the external magnetic field ( $B_0$ ) is applied, then the energy levels splits. Such splitting is called as Zeeman splitting (shown in **Figure 1.36**). The initial population in the energy levels can be calculated by Boltzmann distribution (equation 14).

$$\left( \frac{N^-}{N^+} \right) = e^{\left( \frac{E}{kT} \right)} \quad (14)$$

where,  $N^+$  is the number of spins in the lower energy level,  $N^-$  is the number of spins in the upper energy level,  $E$  is the energy difference between the energy levels,  $k$  is the Boltzmann constant, and  $T$  is the temperature in kelvin.

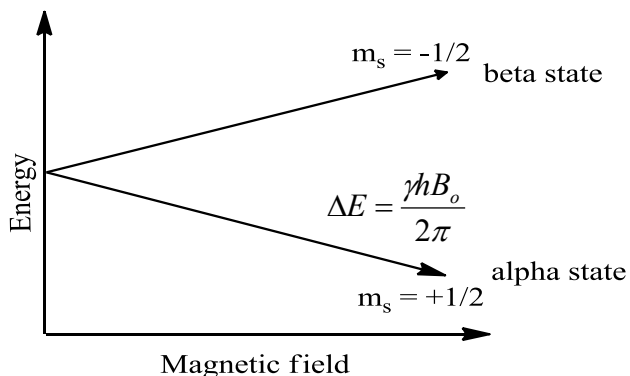


**Figure 1.36.** Splitting of energy levels in the presence of the external magnetic field ( $B_0$ ).<sup>96</sup>

It is possible to excite these nuclei into the higher level with electromagnetic radiation. The frequency of radiation needed is determined by the difference in energy between the energy levels. When the energy is removed, the energized nuclei relax back to the alpha state. The fluctuation of the magnetic field associated with this relaxation process is called resonance and this resonance can be detected and converted into the peaks that we see in an NMR spectrum.<sup>96-98</sup>

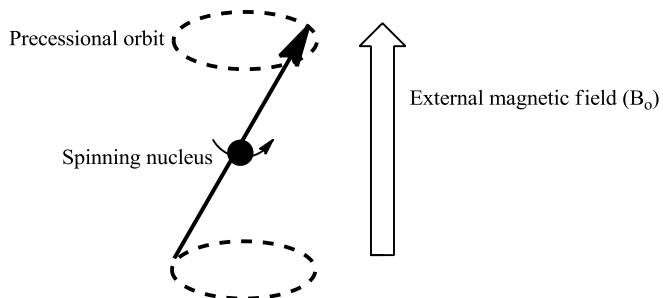


**Figure 1.37.** Axis of rotation of nucleus in the presence of the external magnetic field ( $B_0$ ).<sup>96-98</sup>

Let's consider the nucleus with nuclear spin  $\frac{1}{2}$ . In the absence of the external magnetic field, the nucleus spins in its own axis. However, in the presence of the external magnetic field, the axis of rotation of nucleus precesses around the magnetic field (shown in the **Figure 1.37**). The frequency of precession is called as Larmor frequency ( $\omega_0$ )<sup>96</sup> and is expressed in equation 15.

$$\omega_0 = -\gamma B_0 \quad (15)$$

When the sample is placed in the external magnetic field  $B_0$ , the net magnetic moments at equilibrium aligned in the direction of the external magnetic field (shown in **Figure 1.38**). This net magnetization can be fluctuated by applying a type of electromagnetic radiation (i.e. radio frequency waves) for a short period of time. The signals generated by the relaxation process (i.e. resonance) of the spins are detected and Fourier-transformed to yield a spectrum.

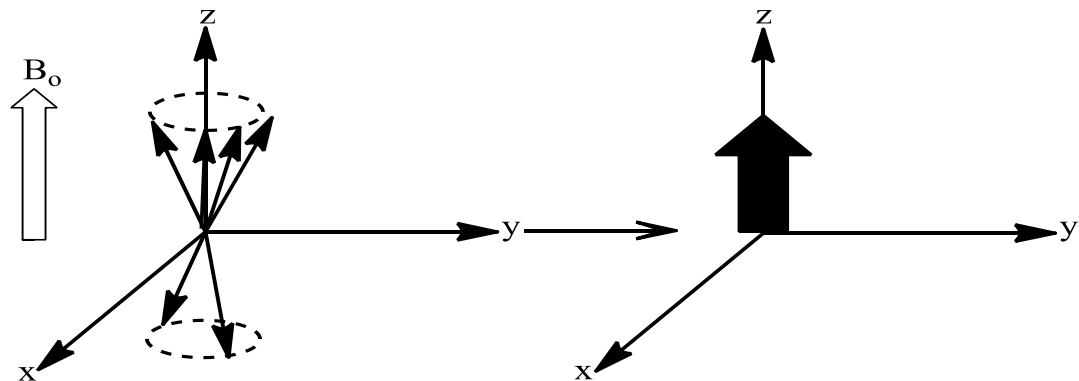


**Figure 1.38.** Bulk magnetization of the spins aligned in the direction of the external magnetic field.<sup>96, 97</sup>

Spins also experience internal interactions in addition to external. Consider two spin systems with nuclear spins  $\hat{I}_{z1}$  and  $\hat{I}_{z2}$  shown in **Figure 1.39**, the interactions between those nuclear spins could be a) dipole-dipole also called as “Dipolar coupling, b) Scalar coupling or J-coupling, c) Quadrupolar coupling, and d) Chemical shift. The dipolar interactions results from interaction of one nuclear spin with a magnetic field generated by another nuclear spin. This is a direct through space interaction. Dipolar Hamiltonian energy can be expressed in dipolar alphabet shown is equation 16. Notice that only term A contributes to heteronuclear spin pairs and both A and B contributes to homonuclear spin pairs (shown in equations 17 and 18). Other dipolar alphabets contribute to spin relaxation (shown in equations 19-22).

$$\hat{H}_D = \frac{\gamma_1 \gamma_2 \hbar^2 \mu_o}{4\pi r^3} [A + B + C + D + E + F] \quad (16)$$

$$A = -(I_{z1} I_{z2})(3 \cos^2 \theta - 1) \quad (17)$$

$$B = \left(\frac{1}{4}\right)(I_{1+} I_{2-} + I_{1-} I_{2+})(3 \cos^2 \theta - 1) \quad (18)$$

$$C = \left(-\frac{3}{2}\right)(\hat{I}_{z1} \hat{I}_{2+} + \hat{I}_{z2} \hat{I}_{1+}) [\sin \theta \cos \theta \exp(-i\phi)] \quad (19)$$

$$D = \left(-\frac{3}{2}\right) (\hat{I}_{z1} \hat{I}_{z2} + \hat{I}_{z2} \hat{I}_{z1}) [\sin \theta \cos \theta \exp(i\phi)] \quad (20)$$

$$E = \left(-\frac{3}{4}\right) (\hat{I}_{1+} \hat{I}_{2+}) [\sin^2 \theta \exp(-i2\phi)] \quad (21)$$

$$F = \left(-\frac{3}{4}\right) (\hat{I}_{1-} \hat{I}_{2-}) [\sin^2 \theta \exp(i2\phi)] \quad (22)$$

Where,  $\gamma_1$  and  $\gamma_2$  are the magnetogyric ratios of the nuclei;  $\hat{I}_{z1}$  and  $\hat{I}_{z2}$  are the nuclear spins;  $\hat{I}_{1+}$  and  $\hat{I}_{1-}$  are the spins down and up of nucleus 1;  $\hat{I}_{2+}$  and  $\hat{I}_{2-}$  are the spins down and up of the nucleus 2;  $\theta$  and  $\phi$  are the arrangement of the nuclear spins 1 and 2 in X-Y plane; and  $r$  is the internuclear distance between nuclei.

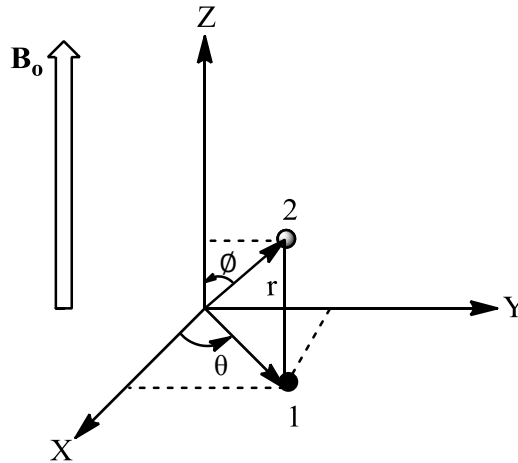


**Figure 1.39.** Two spin system in the magnetic field  $B_0$ .<sup>96,97</sup>

Dipolar Hamiltonian energy terms A and B contain  $(3\cos^2 \theta - 1)$ . To eliminate the dipolar coupling, the sample is placed at when  $\theta = 54.7^\circ$ ,  $(3\cos^2 \theta - 1)$  becomes zero. Hence, to eliminate the dipolar coupling, the sample is placed at  $\theta = 54.7^\circ$  (shown in **Figure 1.40**). Scalar coupling results from the indirect magnetic interactions of nuclear spins with each other through

the involvement of the electrons. Quadrupolar coupling results from the electric interactions of nuclei with nuclear spin  $> \frac{1}{2}$  with the surrounding electric fields.<sup>96,97</sup>

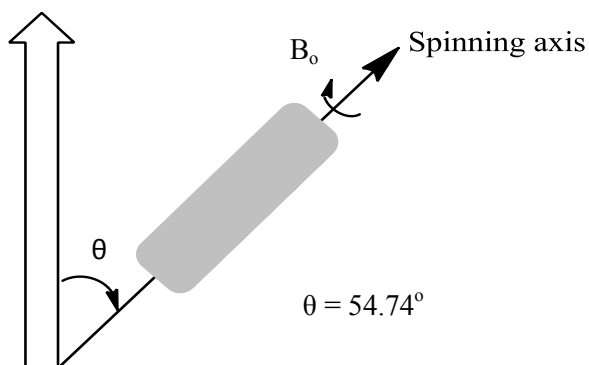


**Figure 1.40.** Sample rotor at magic angle with respect to applied magnetic field ( $B_0$ ).<sup>96,97</sup>

Since the nucleus responds to the external applied effective magnetic field. This change in the effective field on the nuclear spin causes the NMR signal frequency to shift. This shift is called as chemical shift ( $\delta$ ). It is calculated from the equation **23**. The magnitude of the shift depends upon the type of nucleus and the details of the electron motion in the nearby atoms and molecules.

$$\delta = \frac{\nu_s - \nu_r}{\text{operating frequency}} \times 10^6 \quad (23)$$

where,  $\nu_s$  and  $\nu_r$  are the frequencies of the sample and reference respectively.

### 1.9.7.1 Bloch decay experiments

It is a simple single pulse experiment for observing  $^{13}\text{C}$  carbon. The pulse diagram of Bloch decay experiment is shown in the **Figure 1.41**. The bulk magnetization of carbon atoms are switched to the Y axis by applying  $90^\circ$  radio frequency (r.f.) pulse on the carbon. The carbon signal is then detected while decoupling proton. This detected signal is called a free-induction decay which is then Fourier transformed to get the spectrum.



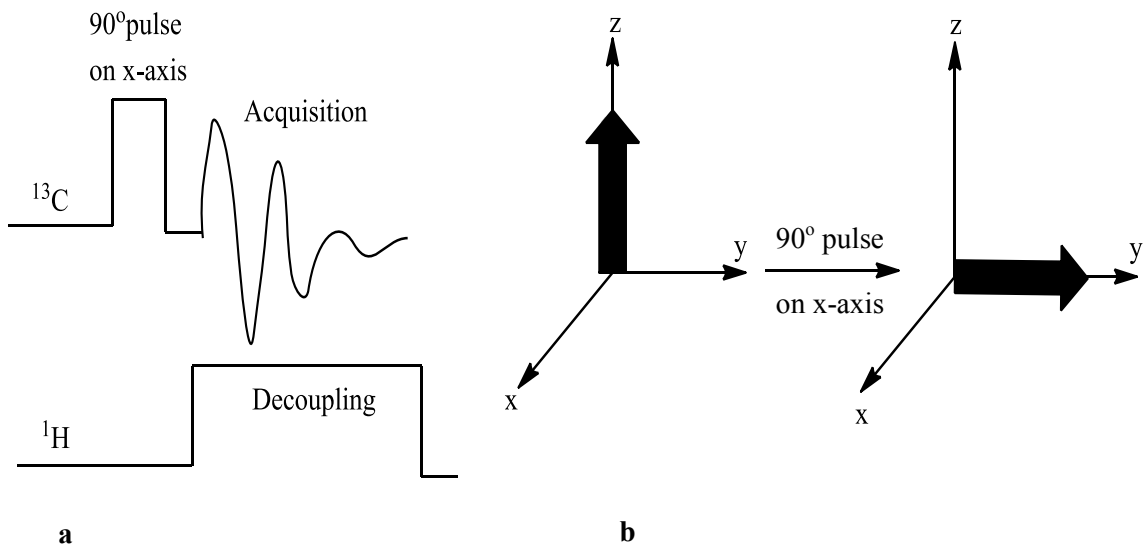


**Figure 1.41.** a) Pulse diagram of Bloch decay experiment and b) vector model representation of spins after  $90^\circ$  pulse.<sup>96, 97</sup>

### 1.9.7.2 Cross polarization experiment (CP/MAS NMR)

$^{13}\text{C}$  CP NMR coupled with MAS are the most commonly used NMR experiments. In this technique, the polarization from the abundant nuclei (such as  $^1\text{H}$ ,  $^{19}\text{F}$ , and  $^{31}\text{P}$ ) is transferred to the dilute spins (such as  $^{13}\text{C}$ ). CP/MAS NMR enhances the sensitivity of dilute nuclei but is not quantitative.

In order to transfer the polarization, one needs to match the Zeeman splitting (i.e.  $\Delta E$ ) of both abundant and rare nuclei (shown in **Figure 1.42**). The key to obtain efficient cross polarization is setting the Hartmann-Hahn match properly. In such cases, the radio frequency fields of the dilute spins are set equal to abundant spins by adjusting the pulse widths ( $\pi/2$ ) of protons and carbons. The two spin systems (abundant and rare) are coupled through dipolar interactions and since both spin types precess with the same frequencies, the energy can be transferred from abundant to dilute nuclei to enhance the signal.

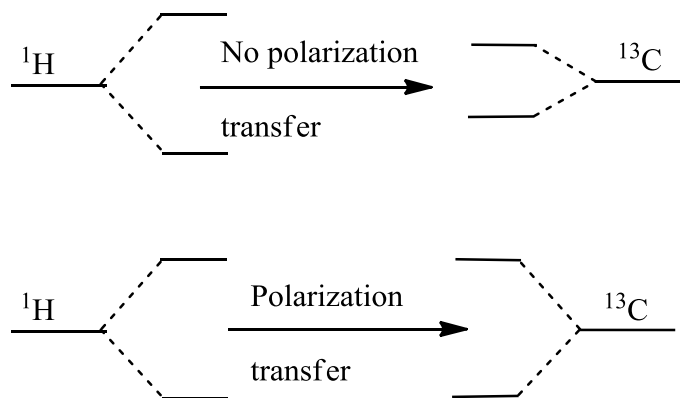


**Figure 1.42.** Zeeman splitting occurring at Hartmaan-Hahn condition.<sup>96-98</sup>

The pulse sequence of CP/MAS is shown in the **Figure 1.43**. The bulk magnetization of proton atoms is switched to y axis by applying the r.f. pulse. The phase of the proton is changed in order to lock the magnetization. Simultaneously, the r.f. pulse is turned on  $^{13}\text{C}$  channel. The polarization is transferred during the spin locking period.  $^{13}\text{C}$  carbon signals are then acquire while decoupling proton.

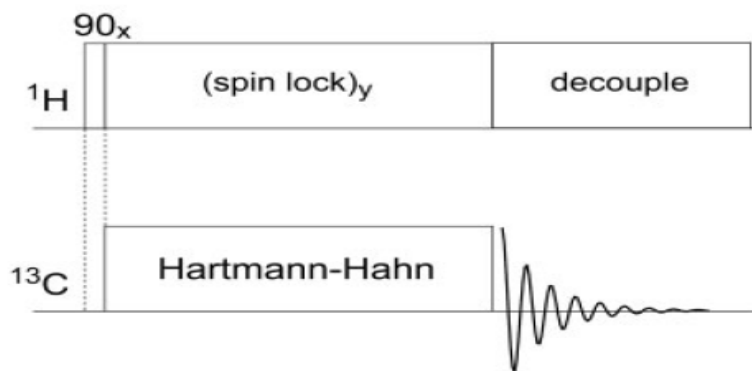


**Figure 1.43.** Pulse diagram of CP/MAS NMR.<sup>98</sup>

### 1.10 Structure of the dissertation

Chapter 2 discusses the first proof of concept which includes detailed synthesis and characterization of polymer silica nanocomposites using allyl functionalized pluronic P123 (aP123). Its limitation for generating composites with high organic content is also mentioned. Chapter 3 is an extension of the new strategy focusing on synthesizing two different surfmers (acrylated P123 and styrenatedP123) followed by preparing mesoporous silica/ polymer nanocomposites. Polymer mesoporous silica nanocomposites with different organic content were prepared and their rheological properties are studied. Chapter 4 focuses on application of approach on different surfmer that is biodegradable and biocompatible which is acrylated poly(ethylene oxide)-b-poly(caprolactone)-b-poly(ethylene oxide) triblock copolymer for the synthesis of mesoporous silica and generating nanocomposites networks from them.

### 1.11 References

1. Li, F. S.; Zhou, S. X.; Wu, L. M. Preparation and Characterization of UV-curable MPS-modified Silica Nanocomposite Coats. *J. Appl. Polym. Sci.* **2005**, *98*, 2274-2281.
2. Li, F. S.; Zhou, S. X.; Gu, G. X.; You, B.; Wu, L. M. Preparation and Characterization of Ultraviolet Curable Nanocomposite Coatings Initiated by Benzophenone/*n*-methyl diethanolamine. *J. Appl. Polym. Sci.* **2005**, *96*, 912-918.
3. Li, F. S.; Zhou, S. X.; Wu, L. M. Effects of Preparation Method on Microstructure and Properties of UV-curable Nanocomposite Coatings Containing Silica. *J. Appl. Polym. Sci.* **2005**, *98*, 1119-1124.
4. Li, F. S.; Zhou, S. X.; You, B.; Wu, L. M. Kinetic Investigations on the UV-induced Photopolymerization of Nanocomposites by FTIR Spectroscopy. *J. Appl. Polym. Sci.* **2005**, *99*, 1429-1436.

5. Sangermano, M.; Malucelli, G.; Amerio, E.; Priola, A.; Billi, E.; Rizza, G. Photopolymerization of Epoxy Coatings Containing Silica Nanoparticles. *Prog. Org. Coat.* **2005**, *54*, 134-138.
6. Su, Y. L. Preparation of polydiacetylene/silica nanocomposite for use as a chemosensor. *React. Funct. Polym.* **2006**, *66*, 967-973
7. Jang, J.; Ha, J.; Lim, B. Synthesis and Characterization of Monodisperse Silica-Polyaniline Core-Shell Nanoparticles. *Chem. Commun.* **2006**, 1622-1624.
8. Zou, H.; Wu, S.; Shen, J. Polymer/Silica Nanocomposites: Preparation, Characterization, Properties, and Applications. *Chem. Rev.* **2008**, *108*, 3893–3957.
9. Saheb, D. N.; Jog, J. P. Natural Fiber Polymer Composites: A Review. *Adv. Poly. Tech.* **1999**, *18*, 351-363.
10. Barkoula, N. M.; Piefis, T.; Schimanski, T.; Loos, J. Processing of Single Polymer Composites Using the Concept of Constrained Fibers. *Polym. Compos.* **2005**, *26*, 114-120.
11. J.Y. Sheikh-Ahmad, Introduction to Polymer composites, Machining of Polymer Composites. 2009 Chapter 1, 1-35.
12. Sant Kumar Malhotra, Koichi Goda, and Meyyarappallil Sadasivan Sreekela, Polymer composites Volume 1 Chapter 1 Advances in Polymer composites: Macro-and Microcomposites-State of Art, New Challenges, and Opportunities, 2012, 1-16
13. Kang, S.; Hong, S. I.; Choe, C. R.; Park, M.; Rim, S.; Kim, J. Preparation and Characterization of Epoxy Composites Filled with Functionalized Nanosilica Particles Obtained via Sol–Gel Process. *Polymer* **2001**, *42*, 879-887.
14. Sugimoto, H.; Daimatsu, K.; Nakanishi, E.; Ogasawara, Y.; Yasumura, T.; Inomata, K. Preparation and Properties of Poly(methylmethacrylate)–Silica Hybrid Materials Incorporating Reactive Silica Nanoparticles. *Polymer* **2006**, *47*, 3754-3759.
15. Liu, Y. L.; Hsu, C. Y.; Wang, M. L.; Chen, H. S. A Novel Approach of Chemical Functionalization on Nano-Scaled Silica Particles. *Nanotechnology* **2003**, *14*, 813-819.

16. Liu, Y. L.; Hsu, C. Y.; Hsu, K. Y. Poly(methylmethacrylate)-silica nanocomposites films from surface-functionalized silica nanoparticles. *Polymer* **2005**, *46*, 1851-1856.
17. Liu, Y.L.; Hsu, C. Y.; Su, Y. H.; Lai, J. Y. Chitosan-Silica Complex Membranes from Sulfonic Acid Functionalized Silica Nanoparticles For Pervaporation Dehydration of Ethanol-Water Solutions. *Biomacromolecules* **2005**, *6*, 368-373.
18. Su, Y. H.; Wei, T. Y.; Hsu, C. H.; Liu, Y. L.; Sun, Y. M.; Lai, J. Y. Using a Novel Sulfonated Silica Nanoparticles for Nafion® Membrane for Direct Methanol Fuel Cell. *Desalination* **2006**, *200*, 656-657.
19. Su, Y. H.; Liu, Y. L.; Sun, Y. M.; Lai, J. Y.; Wang, D. M.; Gao, Y.; Liu, B. J.; Guiver, M. D. Proton exchange membranes modified with sulfonated silica nanoparticles for direct methanol fuel cells. *J. Membr. Sci.* **2007**, *296*, 21-28.
20. Moncada, E.; Quijada, R.; Retuert, J. Nanoparticles Prepared by the Sol–Gel Method and Their Use in the Formation of Nanocomposites with Polypropylene. *Nanotechnology* **2007**, *18*, 335606-335612.
21. Wu, C. L.; Zhang, M. Q.; Rong, M. Z.; Friedrich, K. Silica Nanoparticles Filled Polypropylene: Effects of Particle Surface Treatment, Matrix Ductility and Particle Species on Mechanical Performance of the Composites. *Compos. Sci. Technol.* **2005**, *65*, 635-645.
22. Rong, M. Z.; Zhang, M. Q.; Zheng, Y. X.; Zeng, H. M.; Walter, R.; Friedrich, K. Irradiation Graft Polymerization on Nano-Inorganic Particles: An Effective Means to Design Polymer-Based Nanocomposites. *J. Mater. Sci. Lett.* **2000**, *19*, 1159-1161.
23. Rong, M. Z.; Zhang, M. Q.; Zheng, Y. X.; Zeng, H. M.; Walter, R.; Friedrich, K. Structure–Property Relationships of Irradiation Grafted Nano-Inorganic Particle Filled Polypropylene Composites. *Polymer* **2001**, *42*, 167-183.
24. Zhang, M. Q.; Rong, M. Z.; Zeng, H. M.; Schmitt, S.; Wetzel, B.; Friedrich, K. Atomic force microscopy study on structure and properties of irradiation grafted silica particles in polypropylene-based nanocomposites. *J. Appl. Polym. Sci.* **2001**, *80*, 2218-2227.

25. Rong, M. Z.; Zhang, M. Q.; Zheng, Y. X.; Zeng, H. M.; Friedrich, K. Improvement of Tensile Properties of Nano-SiO<sub>2</sub>/PP Composites In Relation to Percolation Mechanism. *Polymer* **2001**, *42*, 3301-3304.
26. Wu, C. L.; Zhang, M. Q.; Rong, M. Z.; Lehmann, B.; Friedrich, K. Deformation Characteristics of Nano-SiO<sub>2</sub> filled Poly(propylene) Composites. *Polym. Polym. Compos.* **2003**, *11*, 559-562.
27. Ruan, W. H.; Zhang, M. Q.; Rong, M. Z.; Friedrich, K. Polypropylene Composites Filled with In-Situ Grafting Polymerization Modified Nano-Silica Particles. *J. Mater. Sci.* **2004**, *39*, 3475-3478.
28. Rong, M. Z.; Zhang, M. Q.; Pan, S. L.; Friedrich, K. Interfacial Effects in Polypropylene–Silica Nanocomposites. *J. Appl. Polym. Sci.* **2004**, *92*, 1771-1781.
29. Ahn, S. H.; Kim, S. H.; Lee, S. G. Surface-Modified Silica Nanoparticle–Reinforced Poly(ethylene 2,6-naphthalate). *J. Appl. Polym. Sci.* **2004**, *94*, 812-818.
30. Lai, Y. H.; Kuo, M. C.; Huang, J. C.; Chen, M. On the PEEK Composites Reinforced by Surface-Modified Nano-Silica. *Mater. Sci. Eng. A.* **2007**, *458*, 158-169.
31. Ding, X. F.; Zhao, J. Z.; Liu, Y. H.; Zhang, H. B.; Wang, Z. C. Silica Nanoparticles Encapsulated by Polystyrene via Surface Grafting and In-situ Emulsion Polymerization. *Mater. Lett.* **2004**, *58*, 3126-3130.
32. Ding, X. F.; Wang, Z. C.; Han, D. X.; Zhang, Y. J.; Shen, Y. F.; Wang, Z. J.; Niu, L. An Effective Approach to Synthesis of Poly(methyl methacrylate)/Silica Nanocomposites. *Nanotechnology* **2006**, *17*, 4796-4801.
33. Reculusa, S.; Poncet-Legrand, C.; Ravaine, S.; Mingotaud, C.; Duguet, E.; Bourgeat-Lami, E. Syntheses of Raspberry-like Silica/Polystyrene Materials. *Chem. Mater.* **2002**, *14*, 2354-2359.
34. Mishra, J.; Hwang, K. J.; Ha, C. S. Preparation, Mechanical and Rheological Properties of a Thermoplastic Polyolefin (TPO)/Organoclay Nanocomposite with Reference to the Effect of

- Maleic Anhydride Modified Polypropylene as a Compatibilizer. *Polymer* **2005**, *46*, 1995–2002.
35. Ray, S. S.; Okamoto, M. Polymer/Layered Silicate Nanocomposites: A Review From Preparation to Processing. *Prog. Polym. Sci.* **2003**, *28*, 1539–1641.
36. Garcí'a, M.; Vliet, G.; Jain, S.; Schrauwen, B. A. G.; Sarkissov, A.; Zyl, W. E.; Boukamp, B. Poly(propylene)/ SiO<sub>2</sub> Nanocomposites with Improved Mechanical Properties. *Rev. Adv. Mater. Sci.* **2004**, *6*, 169-175.
37. Tanahashi, M.; Hirose, M.; Lee, J. C.; Takeda, K. Organic/Inorganic Nanocomposites Prepared by Mechanical Smashing of Agglomerated Silica Ultrafine Particles in Molten Thermoplastic Resin. *Polym. Adv. Technol.* **2006**, *17*, 981-990.
38. Kontou, E.; Anthoulis, G. The Effect of Silica Nanoparticles on the Thermomechanical Properties of Polystyrene. *J. App. Polym. Sci.* **2007**, *105*, 1723
39. Katsikis, N.; Zahradnik, F.; Helmschrott, A.; Muñstedt, H.; Vital, A. Thermal Stability of Poly(methyl methacrylate)/Silica Nano- and Microcomposites as Investigated by Dynamic-Mechanical Experiments. *Polym. Degrad. Stab.* **2007**, *92*, 1966-1976.
40. Tanahashi, M.; Hirose, M.; Watanabe, Y.; Lee, J. C.; Takeda, K. J. Silica/Perfluoropolymer Nanocomposites Fabricated by Direct Melt-Compounding: A Novel Method without Surface Modification on Nano-Silica. *Nanosci. Nanotechnol.* **2007**, *7*, 2433-2442.
41. Naderi, N.; Sharifi-Sanjani, N.; Khayyat-Naderi, B.; Faridi-Majidi, R. Preparation of organic–inorganic nanocomposites with core-shell structure by inorganic powders. *J. Appl. Polym. Sci.* **2006**, *99*, 2943-2950.
42. Zhang, Q.; Archer, L. A. Poly(ethylene oxide)/Silica Nanocomposites: Structure and Rheology. *Langmuir* **2002**, *18*, 10435-10442.
43. Zhang, Q.; Archer, L. A. Optical Polarimetry and Mechanical Rheometry of Poly(ethylene oxide)-Silica Dispersions. *Macromolecules* **2004**, *37*, 1928-1936.

44. Odian, G. *Principles of Polymerization*. 4<sup>th</sup> edition, John Wiley & Sons, Inc.: New Jersey, **2004**.
45. Allcock, H. R.; Lampe, F. W.; Mark, J. E. *Contemporary Polymer Chemistry*, 3<sup>rd</sup> edition, Pearson Prentice Hall: New Jersey, **2003**.
46. <http://www.custompartnet.com/wu/InjectionMolding>
47. [http://www.substech.com/dokuwiki/doku.php?id=compression\\_molding\\_of\\_polymers](http://www.substech.com/dokuwiki/doku.php?id=compression_molding_of_polymers)
48. <http://archive.nrc-cnrc.gc.ca/eng/ibp/irc/cbd/building-digest-157.html>
49. Pal, N.; Bhaumik, A. Soft Templating Strategies for the Synthesis of Mesoporous Materials: Inorganic, Organic–Inorganic Hybrid and Purely Organic Solids. *Adv. in Colloid. Inter. Sci.* **2013**, *189–190*, 21–41.
50. Naik, B.; Ghosh, N. N. A Review on Chemical Methodologies for Preparation of Mesoporous Silica and Alumina Based Materials. *Recent Pat Nanotechnol.* **2009**, *3*, 213-224.
51. Wu, S. H.; Mou, C. Y.; Lin, H. P. Synthesis of Mesoporous Silica Nanoparticles. *Chem. Soc. Rev.* **2013**, *42*, 3862-3875.
52. Hench, L. L.; West, J. L. The Sol-Gel Process. *Chem. Rev.* **1990**, *90*, 33–72.
53. Soler-Illia, G. J.; Azzaroni, O. Multifunctional Hybrids by Combining Ordered Mesoporous Materials and Macromolecular Building Blocks. *Chem Soc Rev.* **2011**, *40*, 1107-1150.
54. Wan, Y.; Zhao, D. On the Controllable Soft-Templating Approach to Mesoporous Silicates *Chem. Rev.* **2007**, *107*, 2821-2860.
55. Hoffmann, F.; Cornelius, M.; Morell, J.; Fröba, M. Silica-Based Mesoporous Organic–Inorganic Hybrid Materials. *Angew. Chem. Int. Ed.* **2006**, *45*, 3216 – 3251.
56. Kresge, C. T.; Leonowicz, M. E.; Roth, W. J.; Vartuli, J. C.; Beck, J. S. Ordered Mesoporous Molecular Sieves Synthesized by a Liquid-Crystal Template Mechanism. *Nature* **1992**, *359*, 710–712.
57. Beck, J. S.; Vartuli, J. C.; Roth, W. J.; Leonowicz, M. E.; Kresge, C. T.; Schmitt, K. D.; Chu, C. T.-W.; Olson, D. H.; Sheppard, E. W.; McCullen, S. B.; Higgins, J. B., Schlenker, J. L. A



- New Family of Mesoporous Molecular Sieves Prepared with Liquid Crystal Templates. *J. Am. Chem. Soc.* **1992**, *114*, 10834–10843.
58. Che, S.; Alfonso, E.; Bennett, G.; Yokoi, T.; Sakamoto, K.; Kunieda, H.; Osamu T.; Tatsumi, T. A Novel Anionic Surfactant Templating Route for Synthesizing Mesoporous Silica with Unique Structure. *Nature Mater.* **2003**, *2*, 801 – 805.
59. Zhao, D.; Feng, J.; Huo, Q.; Melosh, N.; Fredrickson, G. H.; Chmelka, B. F.; Stucky, G. D. Triblock Copolymer Syntheses of Mesoporous Silica with Periodic 50 to 300 Angstrom Pores. *Science* **1998**, *279*, 548-552.
60. Attard, G. S.; Glyde, J. C.; Goltner, C. G. Liquid-Crystalline Phases as Templates for the Synthesis of Mesoporous Silica. *Nature* **1995**, *378*, 366-368.
61. Selvam, P.; Bhatia, S. K.; Sonwane, C. G. Recent Advances in Processing and Characterization of Periodic Mesoporous MCM-41 Silicate Molecular Sieves. *Ind. Eng. Chem. Res.* **2001**, *40*, 3237–3261.
62. Asefa, T.; Tao, Z. Mesoporous Silica and Organosilica Materials — Review of their Synthesis and Organic Functionalization. *Can. J. Chem.* **2012**, *90*, 1015-1031.
63. Eric, M.; Muñoz, R.; Acuña, R. H. Sol Gel-Derived SBA-16 Mesoporous Material. *Int. J. Mol. Sci.* **2010**, *11*, 3069–3086.
64. Steel, A; Carr S.W.; Anderson, M.W. <sup>14</sup>N NMR Study of Surfactant Mesophases in the Synthesis of Mesoporous silicates. *J.Chem. Soc.Chem.Commun.* **1994**, *13*, 1571-1572.
65. Huo, Q.; Margolese, D. I.; Ciesla, U.; Demuth, D. G.; Feng, P.; Gier, T. E.; Sieger, P.; Firouzi, A.; Chmelka, B. F.; Schu"th, F.; Stucky, G. D. Organization of Organic Molecules with Inorganic Molecular Species into Nanocomposite Biphase Arrays. *Chem. Mater.***1994**, *6*, 1176–1191.
66. a) Li, J. G.; Chang, Y. H.; Lin, Y. S.; Kuo, S. W. Templating Amphiphilic Poly(ethylene oxide-b-ε-caprolactone) Diblock Copolymers Provides Ordered Mesoporous Silicas With Large Tunable Pores. *RSC Adv.* **2012**, *2*, 12973-12982. b) Li, J. G.; Kuo, S. W. Phase

- Behaviour of Mesoporous Nanostructures Templated by Amphiphilic Crystalline Diblock Copolymers of Poly(ethylene oxide-*b*- $\epsilon$ -caprolactone). *RSC Advances* **2011**, *1*, 1822–1833.
67. Abdalla, Z. E. A.; Li, B.; Tufail, A. Direct Synthesis of Mesoporous (C<sub>19</sub>H<sub>42</sub>N)<sub>4</sub>H<sub>3</sub>(PW<sub>11</sub>O<sub>39</sub>)/SiO<sub>2</sub> and its Catalytic Performance in Oxidative Desulfurization. *Colloids Surfaces A: Physicochem. Engineer. Aspects* **2009**, *341*, 86-92.
68. Ooi, Y.S.; Bhatia, S. Aluminum-Containing SBA-15 as Cracking Catalyst for the Production of Biofuel from Waste Used Palm Oil. *Microporous Mesoporous Mat.* **2007**, *102*, 310-317.
69. Pasqua, L., Cundari, S.; Ceresa, C.; Cavaletti, G. Recent Development, Applications and Perspectives of Mesoporous Silica Particles in Medicine and Biotechnology. *Current Med. Chem.* **2009**, *16*, 3054-3063.
70. Zornoza, B., S.; Irusta, C.; Tellez; Coronas, J. Mesoporous Silica Sphere Polysulfone Mixed Matrix Membranes for Gas Separation. *Langmuir*, **2009**, *25*, 5903-5909.
71. Sayari, A. Novel Synthesis of High-Quality MCM-48 Silica. *J. Am. Chem. Soc.* **2000**, *122*, 6504-6505.
72. Wang, X.; Wang, P.; Dong, Z.; Dong, Z.; Ma, Z.; Jiang, J.; Li, R.; Ma, J. Highly Sensitive Fluorescence Probe Based on Functional SBA-15 for Selective Detection of Hg<sup>2+</sup> Nanoscale. *Res Lett.* **2010**, *5*, 1468–1473.
73. Ji, X.; Hampsey, J. E.; Hu, Q.; He, J.; Yang, Z.; Lu, Y. Mesoporous Silica-Reinforced Polymer Nanocomposites. *Chem. Mater.* **2003**, *15*, 3656-3662.
74. Burkett, S. L.; Sims, S. D.; Mann, S. Synthesis of Hybrid Inorganic-Organic Mesoporous Silica by Co-condensation of Siloxane and Organosiloxane Precursors. *Chem. Commun.* **1996**, 1367–1368
75. Macquarrie, D. J. Direct Preparation of Organically Modified MCM-41 type Materials. Preparation and Characterization of aminopropyl-MCM and 2-Cyanoethyl-MCM. *Chem. Commun.* **1996**, 1961 – 1962.

76. Lim, M. H.; Blanford, C. F.; Stein, A. Synthesis and Characterization of Reactive Vinyl-Functionalized MCM-41: Probing the Internal Pore Structure by a Bromination Reaction. *J. Am. Chem. Soc.* **1997**, *119*, 4090 – 4091.
77. Kruk, M.; Dufour, B.; Celer, E. B.; Kowalewski, T.; Jaroniec, M.; Matyjaszewski, K. Grafting Monodisperse Polymer Chains from Concave Surfaces of Ordered Mesoporous Silicas. *Macromolecules* **2008**, *41*, 8584-8591.
78. Audouin, F.; Blas, H.; Pasetto, P.; Beaunier, P.; Boissière, C.; Sanchez, C.; Save, M.; Charleux, B. Structured Hybrid Nanoparticles via Surface-Initiated ATRP of Methyl Methacrylate from Ordered Mesoporous Silica. *Macromol. Rapid Comm.* **2008**, *29*, 914-921.
79. Anwender, R.; Nagl, I.; Zapilko, C.; Widenmeyer, M. Methyl Methacrylate Polymerization at Samarium(II)-Grafted MCM-41. *Tetrahedron* **2003**, *59*, 10567-10574.
80. Lunn, J.D.; Shantz, D.F. Peptide Brush-Ordered Mesoporous Silica Nanocomposite Materials. *Chem. Mater.* **2009**, *21*, 3638-3648.
81. Tong, X.; Tang, T.; Zhu, N.; Feng, Z. L.; Huang, B. T. Polymer/Silica Nanoscale Hybrids through Sol-Gel Method Involving Emulsion Polymers. *Chem. J. Chin. Univ.* **2002**, *23*, 306-309.
82. Tong, X.; Tang, T.; Zhang, Q. L.; Feng, Z. L.; Huang, B. T. Polymer/Silica Nanoscale Hybrids through Sol-Gel Method Involving Emulsion Polymers. I. Morphology of Poly(butyl methacrylate)/SiO<sub>2</sub>. *J. Appl. Polym. Sci.* **2002**, *83*, 446-454.
83. Tong, X.; Tang, T.; Feng, Z. L.; Huang, B. T. Preparation of Polymer/Silica Nanoscale Hybrids through Sol-Gel Method Involving Emulsion Polymers. II. Morphology of Poly(ethyl methacrylate)/SiO<sub>2</sub>. *J. Appl. Polym. Sci.* **2002**, *86*, 3532-3536.
84. <http://cnx.org/content/m38278/latest/?collection=col10699/latest>
85. Gary Attard and Colin Barnes; Surfaces Oxford Science Publications
86. Tompsett, G. A.; Krogh, L.; Griffin, D. W.; Conner, W. C. Hysteresis and Scanning Behaviour of Mesoporous Molecular Sieves. *Langmuir* **2005**, *21*, 8214-8225.

87. Barrett, E. P.; Joyner, L. G.; Halenda, P. P. The Determination of Pore Volume and Area Distributions in Porous Substances. *J. Am. Chem. Soc.* **1951**, *73*, 373-380.
88. Maglara, E.; Kaminski, R.; Conner, W. C. In *Characterization of Porous Solids IV*; McEnaney, B., Mays, T.J., Rouquerol, J., Rodrigues-Reinoso, F., Sing, K. S. W., Unger, K. K.; Royal Society of Chemistry:London, **1997**.
89. Wolfinger, M. G. Influence of the Emissivity of the Sample on Differential Scanning Calorimetry Measurements. *Thermochimica Acta* **2001**, *372*, 11-18.
90. <http://www.pslc.ws/macrog/mpm/analysis/dsc.htm>
91. Hwang, D. H.; Lee, J. I.; Cho, N. S.; Shim, H. K. Light-emitting Properties of a Germyl-Substituted PPV Derivative Synthesized *via* a Soluble Precursor. *J. Mater. Chem.* **2004**, *14*, 1026-1030.
92. [http://www.malvern.com/labeng/technology/gel\\_permeation\\_chromatography\\_theory/universal\\_calibration\\_gpc\\_theory.htm](http://www.malvern.com/labeng/technology/gel_permeation_chromatography_theory/universal_calibration_gpc_theory.htm)
93. Tardos, T. F. *Rheology of Dispersions: Principles and Applications*; Wiley-VCH, Weinheim, Germany; **2010**.
94. Walberer, J. A.; McHugh, A. J. The Linear Viscoelastic Behavior of Highly Filled Poly(dimethylsiloxane) Measured in Shear and Compression. *J. Rheol.* **2001**, *45*, 187-201.
95. <http://iramis.cea.fr/scm/lions/techniques/saxs/>
96. Levitt, M. H. *Spin Dynamics: Basics of Nuclear Magnetic Resonance*; 2<sup>nd</sup> edition; Wiley: The University of Southampton, UK; **2008**.
97. Deur, M. J. *Introduction to Solid-State NMR Spectroscopy*; Blackwell: Department of Chemistry, University of Cambridge, **2004**.
98. Taylor, R.E. Setting Up <sup>13</sup>C CP/MAS Experiments. *Concepts in Magnetic Resonance Part A*, **2004**, *22A*, 37-49.

## CHAPTER II

### POLYMERIZABLE STRUCTURE DIRECTING AGENTS THAT ENABLE IN-SITU SYNTHESSES OF COMPOSITE MATERIALS

**Abstract.** The triblock copolymer of ethylene oxide (EO) and propylene oxide (PO) EO<sub>20</sub>-PO<sub>70</sub>-EO<sub>20</sub> commercially known as pluronic P123 have been used in synthesizing mesoporous silica as surfactant. Synthetic modifications to block-copolymer structure directing agents lead to polymerizable macromers suitable for templating the growth of mesoporous silica particles, and which can subsequently react in-situ to form an extended nanocomposite network. This chapter focuses on functionalization of pluronic P123 with allyl chloride and it was investigated whether allyl functionalized P123 preserved the structure-directing capabilities of the triblock polymer for templating ordered mesoporous silica growth. The in-situ polymerization of the triblock templates following silica particle growth results in a true single-phase nanocomposite, characterized by intimately mixed organic-inorganic fractions and interpenetrating/interconnecting chains in and between the inorganic particles.

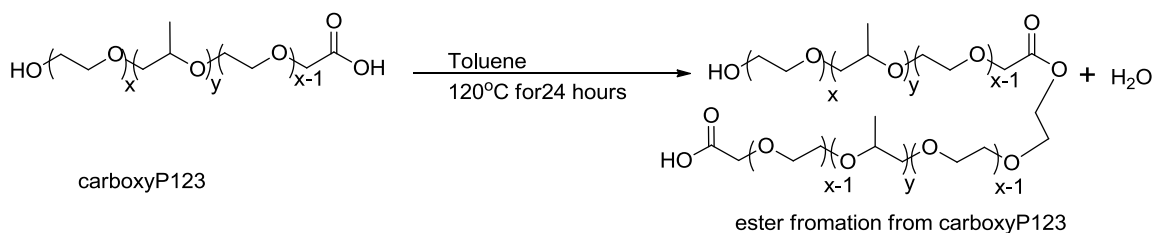
## 2.1 Introduction

Polymer composites lie at the interface between organic and inorganic realms and combine the distinct properties of each in one single component. Composites have been targeted as promising materials due to the advantages that the organic and inorganic components bring into one system.<sup>1,2</sup> Most commonly, composites are prepared via sequential synthetic schemes, in which the inorganic component is prepared separately, and then mixed with the organic components to create the composite. Mesoporous silica SBA15 has been used by material scientists to use it as an inorganic filler in polymer nanocomposites because of its high surface area, thick walls, and well-ordered hexagonal pores. The most common routes for the synthesis of polymer nanocomposites is by introducing the monomer and completing the polymerization in the presence of the inorganic reinforcing agent,<sup>3-7</sup> by post-synthetic grafting,<sup>8</sup> or by simply grafting the mesoporous silica particles together using the monomer and ATRP routes.<sup>9,10</sup> Co-condensation is another one-pot synthetic route to prepare organically modified mesoporous silica. Organic groups such as acrylate, vinyl, allyl, or styryl can be polymerized to form mesoporous silica/polymer nanocomposites.<sup>11</sup>

In this contribution, we investigated an alternative approach to polymer composites that used polymerizable structure-directing agents that can template formation of high-surface area mesoporous silica, and then react with other template molecules to generate an organic network through, around, and in between the silica particles in an in-situ approach. The concept of functional and reactive surfactants,<sup>12</sup> often referred to as “surfmers”,<sup>13-15</sup> is not new in the field of micelle polymerization, but the successful application to synthesis of ordered siliceous-based nanocomposites has not been demonstrated.

The surfactant generally used for synthesis of mesoporous silica SBA15, is as triblock copolymer of poly(ethylene oxide)-b-poly(propylene oxide)-b-poly(ethylene oxide) that is referred to as pluronic P123. Synthetic end-group modification of pluronic P123 is required to make it a polymerizable structure directing agent. There are many reports in literature about end-

group modification (with thiol, acrylic, cyano, carboxylic acid) of pluronic P123 focusing on either hydrogel materials or critical micellar properties of surfactants.<sup>16-19</sup> Carboxylic acid functionalized pluronic P123 (carboxyP123) has been demonstrated to have the structure directing capabilities for ordered mesoporous silica. However, there are some problems associated with its use in polymer nanocomposites: 1) The polymerization of carboxyP123 involves longer reaction times in the presence of solvent, which can remove the carboxyP123 from mesoporous silica and 2) If the water is not removed from the reaction mixture, the degree of polymerization will be lower (shown in **Scheme 2.1**). The structural and surface properties of mesoporous silica made using carboxyP123 are provided in appendix **A1-A4**.



**Scheme 2.1.** Formation of ester linkage.

In this contribution, we describe the synthesis and use of polymerizable surfactants based on allylic modified ethylene oxide/propylene oxide (Pluronic P123) triblock copolymers that serve the dual function of template and macromer, to create organic/inorganic composite materials.

## 2.2 Experimental

### 2.2.1 Materials

Pluronic P123 was purchased from Sigma Aldrich and used as such for functionalization reactions. Allyl bromide was purchased from Alfa Aesar and purified before use. All organic solvents were obtained from Pharmco-AAPER.

### 2.2.2 Characterization

Surface area of mesoporous silica SBA15 and their analogues were determined on Nova2200e Quantachrome instruments. Transmission electron micrographs were acquired on JEOL JEM-2100 with Evex EDS.

600 MHz liquid NMR spectrometer (Varian) was used to determine  $^{13}\text{C}$  NMR (in  $\text{CDCl}_3$ ) to determine the functionalized pluronic P123 at  $40^\circ\text{C}$  at the spinning speed of 20Hz. The solution temperature was equilibrated for 10 minutes before the measurements.

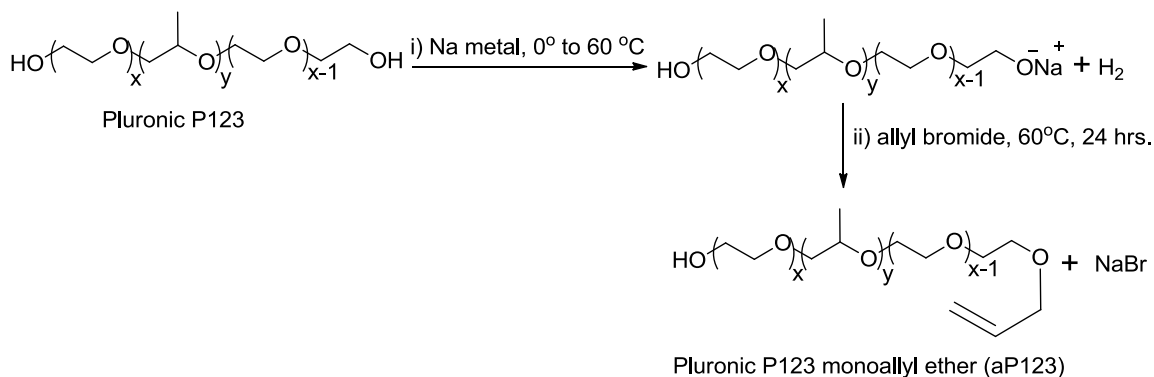
$^{13}\text{C}$  CP/MAS experiments were performed on the composites on 300MHz solid state NMR spectrometer (Bruker) equipped with 4mm probe at spinning speed of 5 kHz at room temperature. Percentage organic content was determined by heating the samples on TA instruments Hi-ResTGA2950 from room temperature to  $600^\circ\text{C}$  with the ramp rate of  $20^\circ\text{C}/\text{min}$  under air flow.

Molecular weights were determined using Agilent 1100 series equipped with refractive index detector. 5 mg of polymer material was dissolved in 1 ml of tetrahydrofuran (THF). Polyethylene glycol standards were utilized as reference. THF was eluting solvent at a flow rate of 1 ml/min, and two PLgel Mixed-C columns in series were used for separation of polymeric material.

**2.2.3 Synthesis of monoallyl Pluronic P123 (aP123).** In a 250 ml two-necked flask, Pluronic P123 (1mmol) was dissolved in 100 mL anhydrous tetrahydrofuran (THF) in an inert atmosphere. The solution was cooled to  $0^\circ\text{C}$  and stirred at 400 rpm. The sodium metal (1.5 mmol), sliced into small pieces, was added to the above solution and heated at  $60^\circ\text{C}$  till all the sodium reacts with the hydroxyl groups. The allyl bromide (1.25 mmol) was then added dropwise into the reaction mixture which was then stirred at  $60^\circ\text{C}$  for 24 hours. The precipitated sodium bromide was removed by filtration. The product was obtained by evaporating the THF in a rotary evaporator and was subsequently purified by extraction into dichloromethane. The solvent was then removed



in a rotary evaporator. Functionalized allyl P123 with 90% yield was isolated. The reaction scheme is shown below in **Scheme 2.2**.

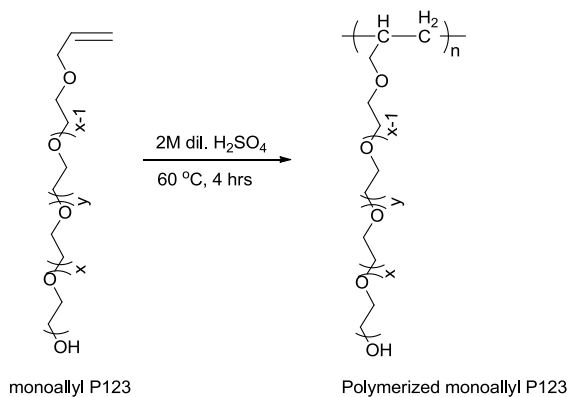


**Scheme 2.2.** Functionalization of pluronic P123 with allyl group.

**2.2.4 Synthesis of SBA-15 and SBA-15 analogues.** The molar composition for the synthesis of SBA-15 or SBA-15 type materials was TEOS:P123/aP123 :HCl:H<sub>2</sub>O = 1: 0.0016 : 5.54 : 182.82, where TEOS is tetraethylorthosilicate. In a typical synthesis, 4 g of P123 or aP123 was dissolved in 30 mL of de-ionized water and stirred for 3 hours at room temperature, and 112 mL of 2.133 M HCl was added drop-wise and the mixture was stirred for 2 hours. The resulting solution was then heated to 40 °C and 9 g of TEOS was added drop-wise and stirring was continued for 20 hours. The reaction mixture was then aged at 100°C for 24 hours under static conditions. The solution was divided into two equal quantities: half of the solution was kept at the same pH and other half was adjusted to neutral pH. The materials from each solution were washed with excess de-ionized water, dried overnight, and calcined at 550°C for 7 hours using a temperature ramp of 1°C/min. Using TGA, XRD, and BET analyses verified that crystalline mesoporous SBA-15 siliceous materials were formed in the presence of either P123 or aP123.

**2.2.5 Polymerization of pluronic P123 monoallyl ether (aP123).** 2ml of 2M dil. H<sub>2</sub>SO<sub>4</sub> was added to 1 gram of aP123 and the reaction mixture was heated to 60°C for 4 hours. The polymerization scheme is shown in **Scheme 2.3**. As described in the text (*vide infra*), GPC

analysis of the polymeric component revealed that a high molecular weight organic phase formed by cationic polymerization.



**Scheme 2.3.** Polymerization of allyl group.

**2.2.6 Characterization of extent of end-group functionalization in aP123.** Shown below in Figure 1 is the 600-MHz solution  $^{13}\text{C}$  NMR spectrum of aP123. The spectrum was obtained with gated decoupling to minimize Nuclear Overhauser effects. In order to preserve the structure-directing capabilities of P123, we targeted ca. 50% conversion of hydroxyl groups to olefinic/allyl groups in the allylbromide reaction. In other words, we wanted an average of one olefinic and one hydroxyl chain end per aP123 molecule. From **Figure 2.1**, which compares the starting P123 spectrum to the product aP123 spectrum, one observes based on the relative intensities of the 60, 67, 116, and 136 ppm end-group peaks in the two spectra that this target was achieved. Note that the starting P123 in Figure 1 has only the characteristic 60-ppm end group peak for the methylene group adjacent the terminal hydroxyl.

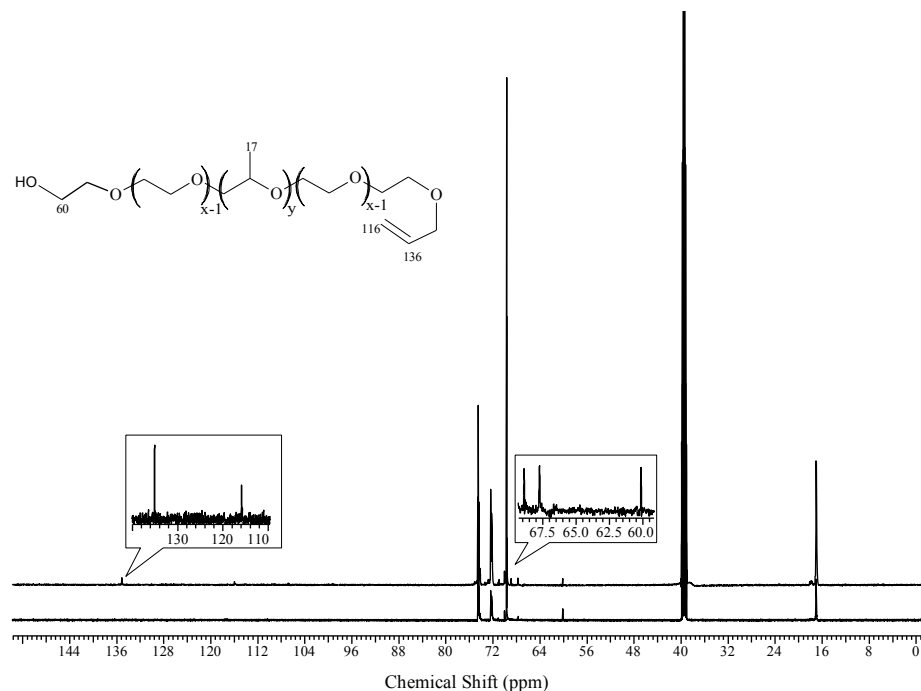


**Figure 2.1.** 600 MHz  $^{13}\text{C}$  solution NMR spectrum acquired with  $^1\text{H}$  decoupling of **(bottom)** pure P123 starting material and **(top)** allyl-functionalized **aP123** following reaction according to Scheme 1. End group signals are shown in the **aP123** inset.

### 2.2.7 Extraction of polymerized aP123 from SBA15\_aP123

Polymerized aP123 was extracted by refluxing 1 g of SBA15\_aP123 composite with ethanol for 2 days. The mixture was filtered and the solvent was then removed by rotary evaporator. GPC analysis of the polymeric component revealed that a high molecular weight organic phase formed in the composite.

## 2.3 Results and Discussion

### 2.3.1 Generating functionalized templates.

Nonionic triblock copolymers based on polyethylene oxide and a central polypropylene oxide block) denoted here as PEO-PPO-PEO (commonly referred to by their Pluronic trade name, have garnered widespread attention for the synthesis of SBA-15 mesoporous silicas.<sup>20, 21</sup> Here, we use Pluronic P123 (P123), HO-(PEO)<sub>20</sub>-(PPO)<sub>70</sub>-(PEO)<sub>20</sub>-H, as the template for SBA-15 formation, but employ functionalization methods to convert one end group to a reactive olefinic moiety. Allyl bromide, when reacted with P123 in

the presence of sodium metal and THF in an inert atmosphere, leads to a monoallyl-functionalized P123 as described above in **Figure 2.1**. Reaction stoichiometries were selected to convert approximately one hydroxyl end-group per P123 chain to an olefinic end group, as depicted schematically in **Figure 2.2**. In this way, each modified P123 is rendered bifunctional, and capable of acid-catalyzed polymerization through the olefinic end groups with surrounding template molecules as shown in **Figure 2.2**. Given that the structure-directing characteristics of the allyl-modified P123, denoted in this paper as aP123, are not known, the fact that **aP123** preserves P123's mesoporous silica structure-directing capabilities were first established. Standard literature synthesis conditions<sup>20</sup> for SBA-15 preparation, using in separate experiments P123 or aP123, yielded materials both before and after calcination that are by all measures identical. **Figure 2.3** compares the powder XRD results from materials synthesized using the control P123 and the modified aP123, prior to calcination, both of which contain characteristic diffraction peaks consistent with published SBA-15 topologies. TGA results in **Figure 2.4** indicate that the P123 and aP123 content of the respective ordered silica products is the same at 33 mass percent, as is the decomposition temperature at 200°C, albeit with the caveat that the aP123 material exhibits a sharper mass loss. The sharper mass-loss transition in the aP123 material is reproducible over many runs, but at this time, we are not certain why this behavior is observed.

While our goal is not creating calcined mesoporous silicas, the BET surface area following calcination is the key indicator of the ordering induced by each template. Table 3.1 shows the physicochemical properties of mesoporous silica using pluronic P123 and aP123. Experimental results for the calcined aP123 SBA material and SBA15 was 921 m<sup>2</sup>/g and 945 m<sup>2</sup>/g surface area respectively. This result was replicated, and the essentially identical surface area for aP123 SBA-15 was also observed for experiments in which the solution was neutralized to a pH = 7 prior to drying. Clearly, the olefinic group on one end of the aP123 templates does

not alter the ability to form micelles in the aqueous environment, or to template crystallization of ordered mesoporous silica. However, separate experiments revealed that P123 modified to contain an olefinic group on both chain ends, i.e., di-allyl with no hydroxyl groups, did not lead to SBA synthesis (*vide infra*).

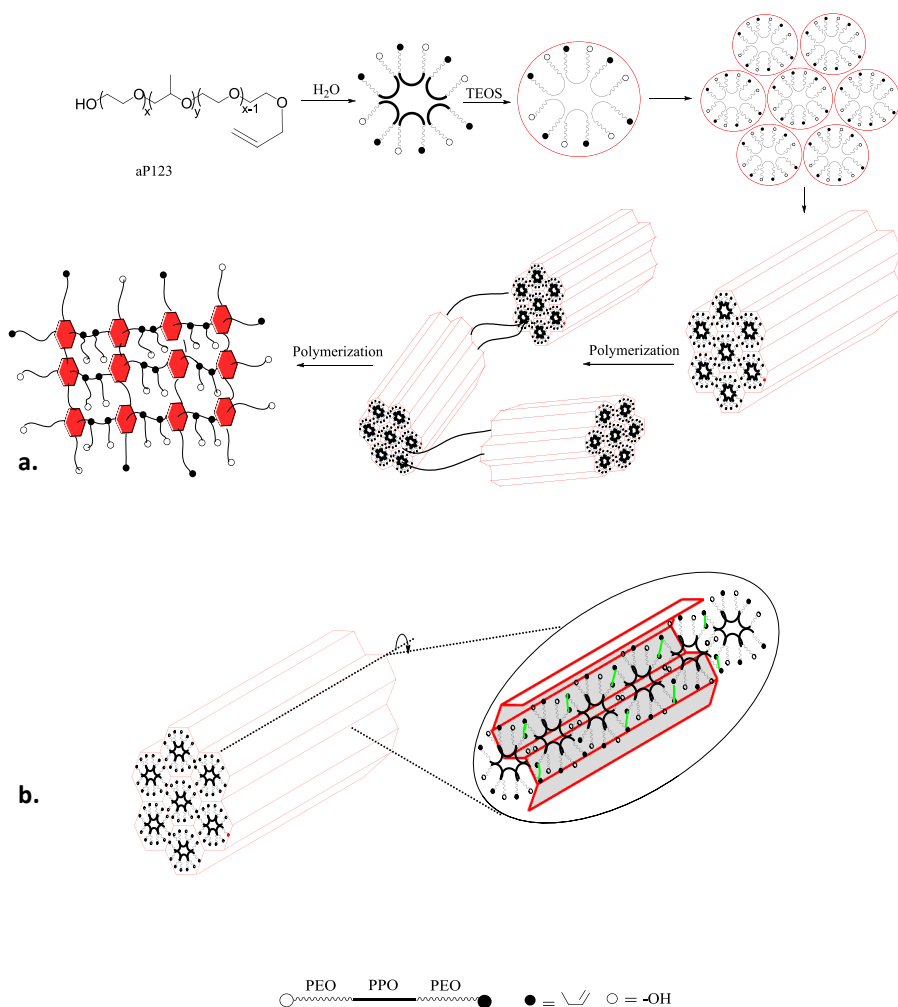


**Figure 2.2.** a) Schematic representation of synthesis of mesoporous materials and polymer composite networks using the allyl-modified P123 surfactant, and b) Expanded view of channel interior showing reaction (denoted by green lines) between olefinic ends of neighboring template molecules. The small orange hexagons in the last frame of 2a represent individual SBA particles in the network.

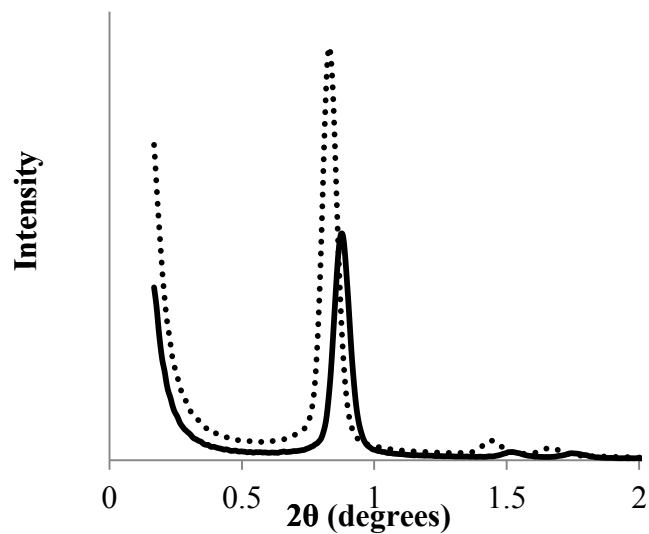


**Figure 2.3.** Small-Angle X-Ray Scattering of SBA15P123 and SBA15\_aP123, denoted by solid and dotted lines respectively

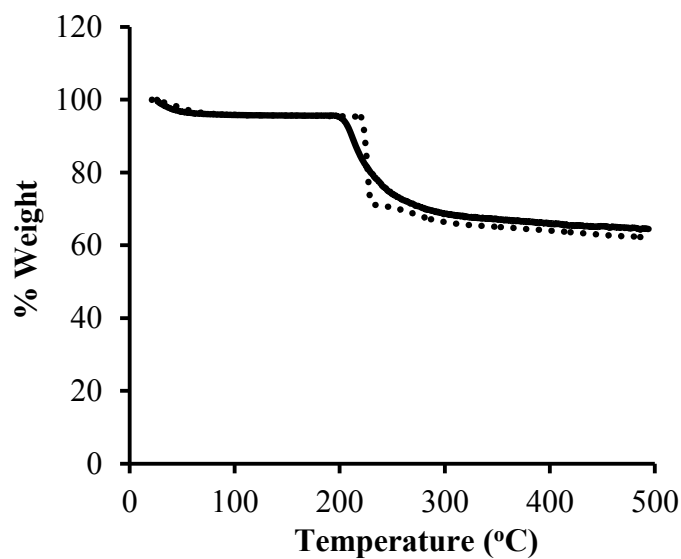


**Figure 2.4.** TGA data of SBA15P123 and SBA15\_aP123, denoted by solid and dotted lines respectively. Mass loss for each is 33 wt%.

**Table 2.1** Physicochemical properties of mesoporous silica prepared using pluronic P123 and aP123. SAXS was used to determine the d-spacing. Pore size distributions and BET surface area were determined using N<sub>2</sub>-adsorption-desorption experiments.

Mesoporous silica	d-spacing (100) Å	BET Surface area (m <sup>2</sup> /g)	Pore size (Å)
SBA15_P123	100.40	945	32
SBA15_aP123	106.50	921	33

**2.3.2 Polymerizing the reactive template.** Dilute sulfuric acid addition to the **aP123**/mesoporous silica product mixture following SBA crystallization catalyzed the in-situ polymerization of the **aP123** through the olefinic groups, as depicted in Figure 2. To confirm that polymerization took place, the resulting polymeric fraction was extracted by dissolving the final organic/silica composite material in 50°C ethanol for 48 hours. As controls, GPC analysis of pure P123 and pure aP123 prior to any reaction are shown in Figures **2.5a** and **2.5b**. Monodisperse poly(ethylene glycol) (PEG) standards were used to calibrate the GPC, and the resulting elution time for the pure P123 agreed with its known molecular weight (5700 g/mole). In another control experiment, pure aP123 was reacted with sulfuric acid at the same concentration to ensure that their polymerization occurred, and the high molecular weight peak (broad signal near 6 minutes) shown in Figure **2.5c** indicates that the chemistry leads to polymerization of the aP123 macromers. Finally, Figure **2.5d** shows the GPC result for the polymeric fraction extracted from the final organic/silica composite material, after crystallization and polymerization. The results are similar to **2.5c**, indicating that higher molecular weight species (up to 115,000 g/mol) are formed from the reaction of the aP123 structure directing agent molecules in the composite. TGA analysis of the washed and dried composite, after extraction of the polymer used to generate Figure **2.5d**, revealed that 13 wt% of the polymer remained in the SBA channels after extraction, consistent with formation of higher molecular species like those depicted in **Figure 2.2**.

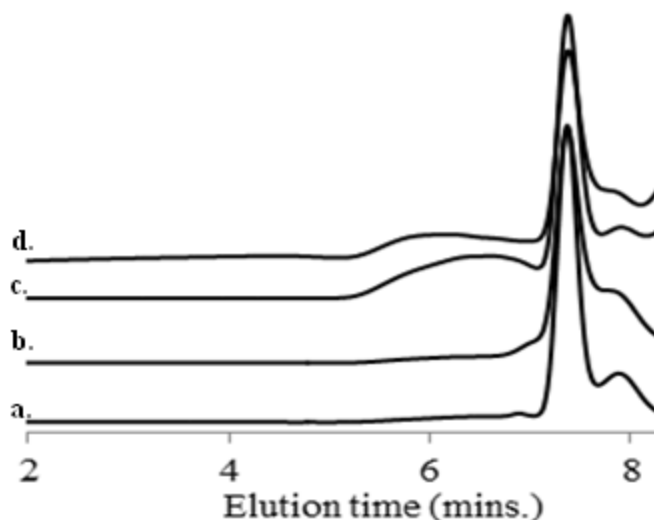


**Figure 2.5.** GPC chromatograms of a) pure P123, b) aP123, c) polymerized aP123, and d) polymer extracted from the composite following polymerization of aP123 template molecules in-situ. No change in molecular weight was observed for control experiments involving pure P123 in the same acid-catalyzed reaction. GPC flow rates were 1 ml/min

The 33 wt% organic content of the material described above is defined by the initial surfactant/TEOS reaction stoichiometry. However, adding additional aP123 at the time the sulfuric acid catalyst is added (to the dried aP123/SBA-15 product described in **Figures 2.3** and **2.4**) can create final products with much higher organic content. As depicted in **Figure 2.5a**, the polymerization proceeds through the olefinic groups, resulting in highly branched structures. One could easily add aP123 that contained olefinic groups on each chain end, i.e. a di-olefinic aP123, and then the entire chain backbone would be incorporated into the growing network. However, this could only be added after formation of SBA-15 using mono-olefinic aP123, i.e., at the point of acid addition to effect polymerization, since di-olefinic aP123 does not lead to stable micelle formation and SBA crystallization.

Solid-state NMR spectra for the washed and dried aP123 composite unequivocally indicate that polymerization of the functionalized templates occurs. **Figure 2.6** below compares



the  $^{13}\text{C}$  CP/MAS data for the P123 molecules in as-synthesized SBA-15, versus that for the aP123/SBA-15 route followed by polymerization. The peak at 31 ppm in Figure 2.6b indicates that polymerization through the olefinic end groups has occurred in the composite synthesis, thereby generating a series of aliphatic  $\text{CH}_2$  groups in the chain. Single-pulse  $^{13}\text{C}$  MAS spectra confirm this assignment (not shown); the same peaks are present albeit with slightly different relative intensities as expected for cross-polarization versus one-pulse experiments.

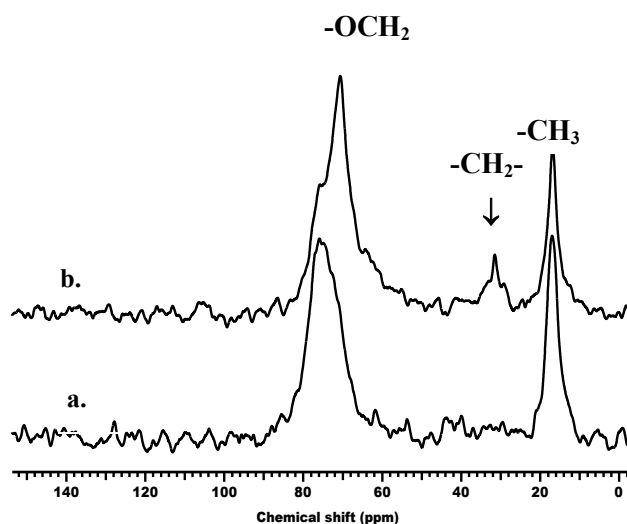


**Figure 2.6.** Solid-state  $^1\text{H}\rightarrow^{13}\text{C}$  CP (cross-polarization)/MAS spectra for (a) the P123 surfactants in normal uncalcined SBA-15 following synthesis, and (b) the organic fraction generated by polymerizing the aP123 structure-directing agents inside and around the SBA-15 following crystallization. The arrow denotes the new aliphatic  $\text{CH}_2$  moieties formed from the reaction.

**2.3.3 Inter-particle versus intra-particle polymerizations and bulk properties.** The minimum organic content in the composite, as defined by the initial stoichiometry required to crystallize SBA-15 from solution, is 33 wt% aP123. While adding more aP123 at the point of catalytic acid addition can easily increase this value, our experiments indicate that even at this lower limit, polymerization occurs between aP123 macromers both inside and outside of the SBA particle channels. Polymerization outside of the channels is required for inter-particle connectivity and true composite properties. To assess the degree to which inter-particle polymerization occurred,

two different materials were pressed into cylindrical pellets at room temperature using a Carver press. The two samples were chemically identical, composed of the aP123/SBA-15 mixture following crystallization, washing, and drying. However, one of the two samples was polymerized, while the other was not. Figures 2.4c, 2.4d, and 2.5b prove polymerization occurs, and if that polymerization is only limited to the interior of the mesoporous silica, then pellets formed from unpolymerized (but still filled with unreacted aP123) and the polymerized material should exhibit essentially identical physical properties. **Figure 2.7a** and **2.7b** compares the images of the pellets formed from each material at 3000-psi plate pressure and room temperature. The unpolymerized material, which exhibits the white color expected for silica, does not form a stable pellet at this pressure, as indicated by the large crack through the bulk material. Indeed, the pellet crumbled when removed from the mold. In contrast, the darker colored polymerized composite pellet forms a tough, stable pellet that may be removed and handled. The color change itself is indicative of polymerization, as this color change is also observed in control experiments involving polymerization of the pure aP123 in the absence of the silica. Similar results were obtained in multiple experiments. If the plate pressure was increased to 5000 psi, then an apparently stable pellet could be made from the unpolymerized sample, but its surface was chalky and easily removed by simply rubbing one's finger across it. More importantly, solvent exposure experiments clearly demonstrated that inter-particle connectivity occurred in the polymerized aP123/SBA-15 sample. When the 5000-psi unpolymerized pellet was dropped into dichloromethane, it immediately rose to the surface while simultaneously releasing visible air bubbles. After a few minutes, no more bubbles were observed and the pellet settled to the bottom of the beaker. In marked contrast, the 3000-psi polymerized aP123/SBA-15 pellet, like that shown in Figure 2.6a, immediately settled to the bottom of beaker filled with dichloromethane, and no air bubbles were ever released. The pellet was stable in the solution for several hours, with little change in its shape or color. The unpolymerized pellet, formed at the higher 5000-psi pressure, developed multiple cracks and began to disintegrate after only one hour in solvent.

**Figure 2.7c** and **2.7d** show the polymerized versus unpolymerized aP123/SBA-15 pellets in dichloromethane, respectively. In total, these experiments prove that polymerization occurs between the particles, and not just within their intracrystalline channels, even for the minimum 33 wt% organic content.

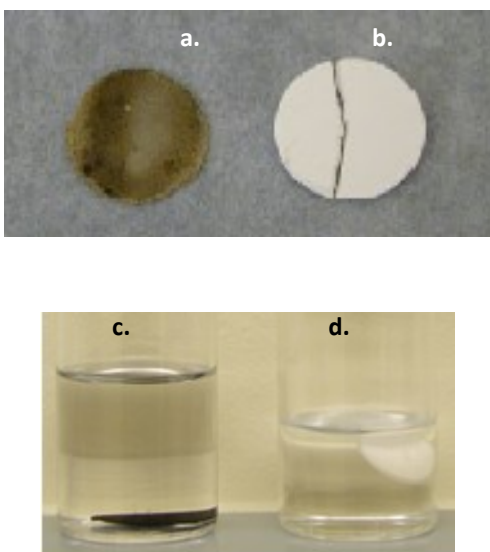


**Figure 2.7.** Pellets formed from (a) polymerized aP123/SBA-15 composite versus (b) versus aP123/SBA-15 without the polymerization step. Both pellets contain ca. 33 wt% organic content. (c) Pellet from polymerized composite in  $\text{CH}_2\text{Cl}_2$ , at the bottom of the vial, and (d) the corresponding unpolymerized control pellet floating near the surface. The two pellets were placed in each solvent container at exactly the same time, which was 1 minute prior to taking the photo.

## 2.4 Conclusions

A novel route to organic/inorganic composite materials has been described, which utilizes end-group functionalization of existing structure-directing agents to enable in-situ synthetic methods. Using allyl-functionalized P123 as a template, we have shown that crystallization of SBA-15 is preserved but that following the crystallization, the template readily polymerizes to form a composite containing high molecular weight polymer filling and surrounding the SBA-15 crystallites in an intimately mixed arrangement. However, the extent of polymerization is low. Therefore, there is a need of reactive monomeric unit on triblock surfactant.

## 2.5 References

1. Limm M.H.; Blanford, C.F.; Stein, A. Synthesis and Characterization of a Reactive Vinyl-Functionalized MCM41: Probing the Internal Pore Structure by a Bromination Reaction. *J. Am. Chem. Soc.* **1997**, *119*, 4090-4091.
2. Bitinis, N.; Hernandez, M.; Verdejo, R.; Kenny, J. M.; Lopez-Manchado, M. A. Recent Advances in Clay/Polymer Nanocomposites. *Adv. Mater.* **2011**, *23*, 5229-5236.
3. He, J.; Shen, Y.; Evans, D. G.; Duan, X. Nanocomposite Structure Based on Silylated MCM-48 and Poly(vinyl acetate). *Chem. Mater.* **2003**, *15*, 3894-3902.
4. Landry, C. J. T.; Coltrain, B. K.; Brady, B. K. In-situ Polymerization of Tetraethylorthosilane in Poly(methyl methacrylate): Morphology and Dynamic Mechanical Properties. *Polymer* **1992**, *33*, 1486-1495.
5. Xu, L.; Hiroyoshi, N.; Evangelos, M.; Ramanan, K. Tailored Nanocomposites of Polypropylene with Layered Silicates. *Macromolecules* **2009**, *42*, 3795-3803.
6. Rovira-Truitt, R.; Patil, N.; White, J. L. Synthesis and Characterization of Biopolymer Composites from the Inside Out. *Macromolecules* **2009**, *42*, 7772-7780.
7. Choi, M.; Kleitz, F.; Liu, D.; Lee, H. Y.; Wha-Seung, A.; Ryoo, R. Controlled Polymerization in Mesoporous Silica Toward the Design of Organic-Inorganic Composite Nanoporous Materials. *J. Am. Chem. Soc.* **2005**, *127*, 1924-1932.
8. Lunn, J. D.; Shantz, D. F. Peptide Brush-Ordered Mesoporous Silica Nanocomposite Materials. *Chem. Mater.* **2009**, *21*, 3638-3648.
9. Kruk, M.; Dufour, B.; Celer, E. B.; Kowalewski, T.; Jaroniec, M.; Matyjaszewski, K. Grafting Monodisperse Polymer Chains from Concave Surfaces of Ordered Mesoporous Silica. *Macromolecules* **2008**, *41*, 8584-8591.
10. Pasetto, P.; Blas, H.; Audouin, F.; Boissière, C.; Sanchez, C.; Save, M.; Charleux, B. Mechanistic Insight into Surface- Initiated Polymerization of Methyl methacrylate and

- Styrene via ATRP from Ordered Mesoporous Silica Nanoparticles. *Macromolecules* **2009**, *42*, 5983-5995.
11. El Kadib, A.; Katir, N.; Finiels, A.; Castel, A.; Marcotte, N.; Molvinger, K.; Biolley, C.; Gaveau, P.; Bousmina, M.; Brunel, D. Mesostructured Fatty Acid-Tethered Silicas: Sustaining the Order by Co-templating with Bulky Precursors. *Dalton Trans.* **2013**, *42*, 1591-1602.
  12. Hsu, Y-C.; Hsu, Y-T.; Hsu, H-Y.; Yang, C-M. Facile Synthesis of Mesoporous Silica SBA-15 with Additional Intra-Particle Porosities. *Chem. Mater.* **2007**, *19*, 1120-1126.
  13. Summers, M.; Eastoe, J. Applications of Polymerizable Surfactants. *Adv. Colloid Interface Sci.* **2003**, 100–102, 137-152.
  14. Dreja, M.; Tieke, B. Microemulsions with Polymerizable Surfactants  $\gamma$ -ray Induced Copolymerizations of Styrene and 11-(acryloyloxy)undecyltrimethyl ammonium bromide in Three Component Cationic Microemulsion. *Macromol. Rapid Commun.* **1996**, *17*, 825-833.
  15. Li, T. D.; Gan, L. M.; Chew, C. H.; Teo, W. K.; Gan, L. H. Preparation of Ultrafiltration Membranes by Direct Microemulsion Polymerization Using Polymerizable Surfactants. *Langmuir* **1996**, *12*, 5863-5868.
  16. Bromberg, L. Polyether-Modified Poly(acrylic acid): Synthesis and Applications. *Ind. Eng. Chem. Res.* **1998**, *37*, 4267-4274.
  17. Custers, J. P. A.; van den Broeke, L. J. P.; Keurentjes, J. T. F. Phase Behavior and Micellar Properties of Carboxylic Acid End Group Modified Pluronic Surfactants. *Langmuir* **2007**, *23*, 12857-12863.
  18. Niu, G.; Zhang, H.; Song, L.; Cui, X.; Cao, H.; Zheng, Y.; Zhu, S.; Yang, Z.; Yang, H. Thiol/Acrylate-Modified PEO-PPO-PEO Triblocks Used as Reactive and Thermosensitive Copolymers. *Biomacromolecules* **2008**, *9*, 2621–2628.
  19. Elluru, M.; Ma, H.; Hadjiargyrou, M.; Hsiao, B. S.; Chu, B. Synthesis and Characterization of Biocompatible Hydrogel using Pluronics-based Block Copolymers. *Polymer* **2013**, *54*, 2088-2095.

20. Zhao, D.; Feng, J.; Huo, Q.; Melosh, N.; Fredrickson, G. H.; Chmelka, B. F.; Stucky, G. D. Triblock Copolymer Syntheses of Mesoporous Silica with Periodic 50 to 300 Angstrom Pores. *Science* **1998**, *279*, 548-552.
21. Ruthstein, S.; Schmidt, J.; Kesselman, E.; Talmon, Y.; Goldfarb, D. Resolving Intermediate Solution Structures During the Formation of Mesoporous SBA-15. *J. Am. Chem. Soc.* **2006**, *128*, 3366-3374.

## CHAPTER III

### SELF-ASSEMBLED POLYMER NANOCOMPOSITES AND THEIR NETWORKS

**Abstract.** In this research, we functionalized the triblock copolymer pluronic P123 with reactive monomeric units such as acryl and styryl groups. Nanocomposite networks prepared using acryl/styryl modified pluronic P123 via self-assembly shown improved storage and loss modulus. It was observed that the storage and loss modulus of nanocomposites obtained were independent of frequency in rheological experiments indicating the formation of perfect networks.

### 3.1 Introduction

Polymer silica nanocomposites are a promising class of hybrid materials and have found applications in catalysis, drug delivery, sensor technology, and gas storage.<sup>1-5</sup> Polymer composite properties largely depend on homogenous distribution of the inorganic component in the polymer matrix. There are three approaches for synthesis of mesoporous silica polymer nanocomposites. One approach is to form organically modified mesoporous silica by co-condensation method followed by polymerization of the organic groups.<sup>6,7</sup> Another approach is to anchor the polymer either by the “grafting to” or the “grafting from” method on the mesoporous silica via hydroxyl groups.<sup>8-10</sup> The third approach is to mix polymer with the silica or silica precursors.<sup>11, 12</sup>

In Chapter 2, we showed the successful application of self-assembled approach to synthesize polymer nanocomposites networks using polymerizable structure directing agent allyl P123 (aP123). However, the degree of polymerization of the allyl group was found to be low. Hence, there is a necessity to functionalize triblock copolymer with reactive monomeric moieties to create nanocomposite networks.

In this chapter, we detail the end-group functionalization of the Pluronic<sup>®</sup>-based copolymers to attach either one or two reactive end groups, which in this case are either styryl- or acrylate-based as shown in Scheme 1. Based on the choice of end-group, final products can be made which are either (1) nanocomposites that contain only physical chain entanglements, or (2) chemically cross-linked nanocomposite networks. In either case, the organic to inorganic composition ratios may be systematically varied in the final materials, as shown by several chemical, spectroscopic, and microscopic characterization methods described herein. The following sections will describe the polymeric surfactant functionalization chemistry, templating and growth of ordered mesoporous SBA-type silica using the modified surfactants, reactions of the modified surfactants with one another to create the continuous organic phase within and between the mesoporous silica particles, and network formation.



## 3.2 Experimental

### 3.2.1 Materials

Pluronic P123 was purchased from Sigma Aldrich and used as such for functionalization reactions. Acryloyl chloride and vinyl benzyl chloride was purchased from Alfa Aesar and Aldrich. All organic solvents were obtained from Pharmco-AAPER.

### 3.2.2 Characterization

Surface area of mesoporous silica SBA15 and their analogues were determined on Nova2200e Quantachrome instruments. Transmission electron micrographs were acquired on JEOL JEM-2100 with Evex EDS.

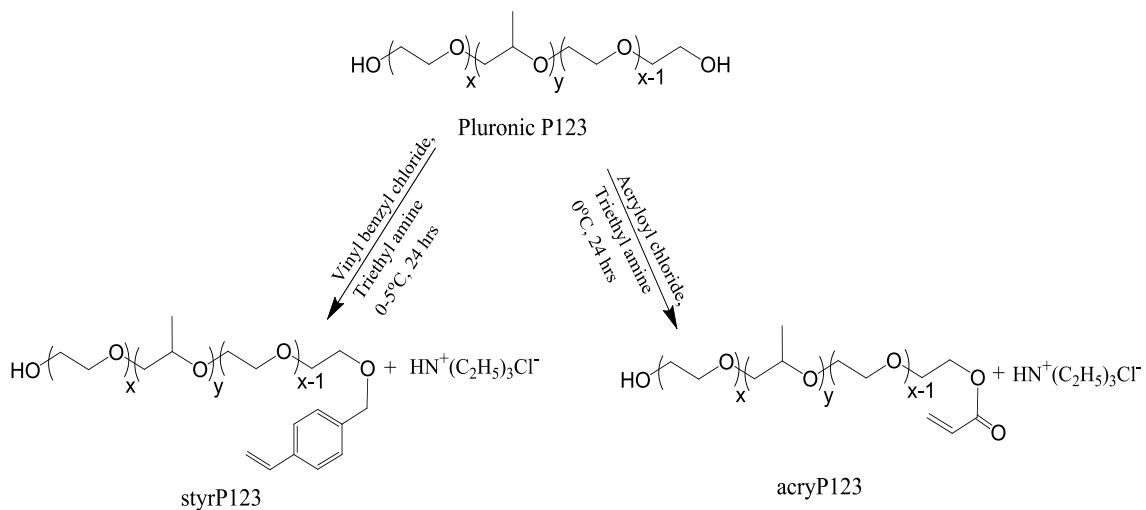
600 MHz liquid NMR spectrometer (Varian) was used to determine  $^{13}\text{C}$  NMR (in deuterated dimethyl sulfoxide) to determine the functionalized pluronic P123 at 40°C at the spinning speed of 20Hz. The solution temperature was equilibrated for 10 minutes before the measurements.

$^{13}\text{C}$  CP/MAS experiments were performed on the composites on 300MHz solid state NMR spectrometer (Bruker) equipped with 4mm probe at spinning speed of 5 kHz at room temperature. Percentage organic content were determined on TA instruments Hi-ResTGA2950.

### 3.2.3 Synthesis of acrylated- and styrenated-functionalized Pluronic P123 (denoted as

**acryP123 and styrP123, respectively).** Pluronic P123 was purchased from Sigma Aldrich and used as such for functionalization reactions. All organic solvents were obtained from Pharmco-AAPER. In a 250 ml two-necked flask, Pluronic P123 (1mmol) was dissolved in 100 mL anhydrous tetrahydrofuran (THF) in an inert atmosphere. The solution was cooled to 0° C and stirred at 400 rpm. 1.25 mmol of acryloyl chloride or 1.25 mmol of Vinyl benzyl chloride (VBC) and triethyl amine (1.25 mmol) were added to the stirred solution. The reagents were reacted for 24 hours (shown in **Scheme 3.1**). The triethyl ammonium chloride salt formed was separated by

filtration. Dichloromethane was removed by rotary vaporization. The product was dried in a vacuum oven for 24hrs at 60°C. Functionalized pluronic P123 with 95% yield was isolated. Chloride ion test was performed to check the formation of triethyl ammonium chloride by adding silver nitrate solution to the recovered salt. Yellow colored precipitate of silver chloride that turns brown upon exposure of light confirms the formation of product.



**Scheme 3.1.** Reaction scheme for the formation of acryP123 and styrP123

**3.2.4 Synthesis of SBA-15 and SBA-15 analogues (acryP123 and styrP123).** The molar composition for the synthesis of SBA-15 or SBA-15 type materials is TEOS: P123 (or acryP123 or styrP123): HCl : H<sub>2</sub>O = 1: 0.016 : 5.54 : 182.82. In a typical synthesis, 4 g of P123 was dissolved in 30 mL of de-ionized water and stirred for 3 hours at room temperature. 112 mL of 2.133 M of HCl was added drop-wise and kept under stirring for 2 hours. The above solution was then heated to 40°C and 9 g of TEOS was added drop-wise and stirred for 20 hours. The reaction mixture was aged at 100°C for 24 hours under static conditions. The mesoporous silica was filtered and rinsed with excess de-ionized water, dried on bench overnight, and calcined at 550 °C for 7 hours at the ramp of 1°C/min. As described in the text, TGA, SAXS, pore size distributions,

and BET analysis verified that crystalline mesoporous SBA-15 siliceous materials were formed in the presence of either P123 or acryP123 or styrP123 (**Table 3.1**).

**Table 3.1** Physicochemical properties of mesoporous silica prepared using pluronic P123 and aP123. SAXS was used to determine the d-spacing. Pore size distributions and BET surface area were determined using N<sub>2</sub>-adsorption-desorption experiments.

Block copolymer	d-spacing (100) Å	BET Surface area (m <sup>2</sup> /g)	Pore size (Å)
SBA15_P123	100.40	945	32
SBA15_acryP123	113.10	930	30
SBA15_styrP123	108.90	1146	32

**3.2.5 Characterization of end-group functionalization in acryP123 and styrP123.** Shown below in **Figure 3.1** is the 600-MHz solution <sup>13</sup>C NMR spectrum of acryP123 following a typical conversion of the type shown in the right side of Scheme 1. The spectrum was obtained with gated decoupling to minimize Nuclear Overhauser effects. In order to preserve the structure-directing capabilities of P123, we targeted ca. 50% conversion of hydroxyl groups to acrylate or styrenate groups in the respective acryloyl chloride or vinyl benzyl chloride reactions. In other words, we wanted an average of one acrylate/styrenate unit and one hydroxyl chain end per acryP123 or styrP123 molecule. From **Figure 3.1**, which compares the starting P123 spectrum to the product acryP123, one observes based on the relative intensities of the 60, 67, 124, and 128 ppm end-group peaks in the two spectra that this target was, on average, achieved. Note that the starting P123 in **Figure 3.1** has only the characteristic 60-ppm end group peak for the methylene group adjacent the terminal hydroxyl. FTIR spectra (not shown here) clearly showed the acrylate carbonyl stretch at 1725 cm<sup>-1</sup> after functionalization and purification.

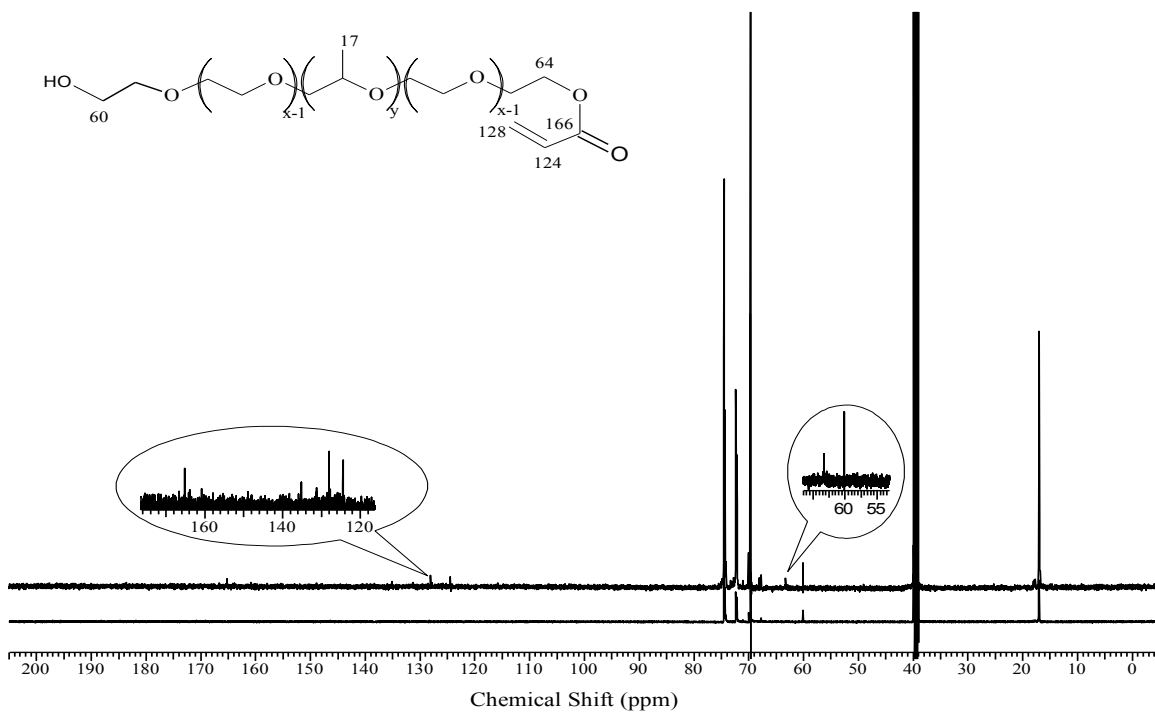


**Figure 3.1.** 600 MHz  $^{13}\text{C}$  solution NMR spectrum acquired with  $^1\text{H}$  decoupling of **(bottom)** pure P123 starting material and **(top)** acrylate-functionalized **acryP123** following reaction according to Scheme 1. End group signals are shown in the **acryP123** inset, exhibiting the characteristic vinyl signals between 120 and 130 ppm.

Similarly, **Figure 3.2** shows the comparable 600-MHz solution  $^{13}\text{C}$  NMR spectrum of styP123 following a typical conversion of the type shown in the right side of Scheme 1. The peaks in the inset demonstrate that on average, the reaction conditions yielded about 50% functionalization of the hydroxyl end groups on P123.

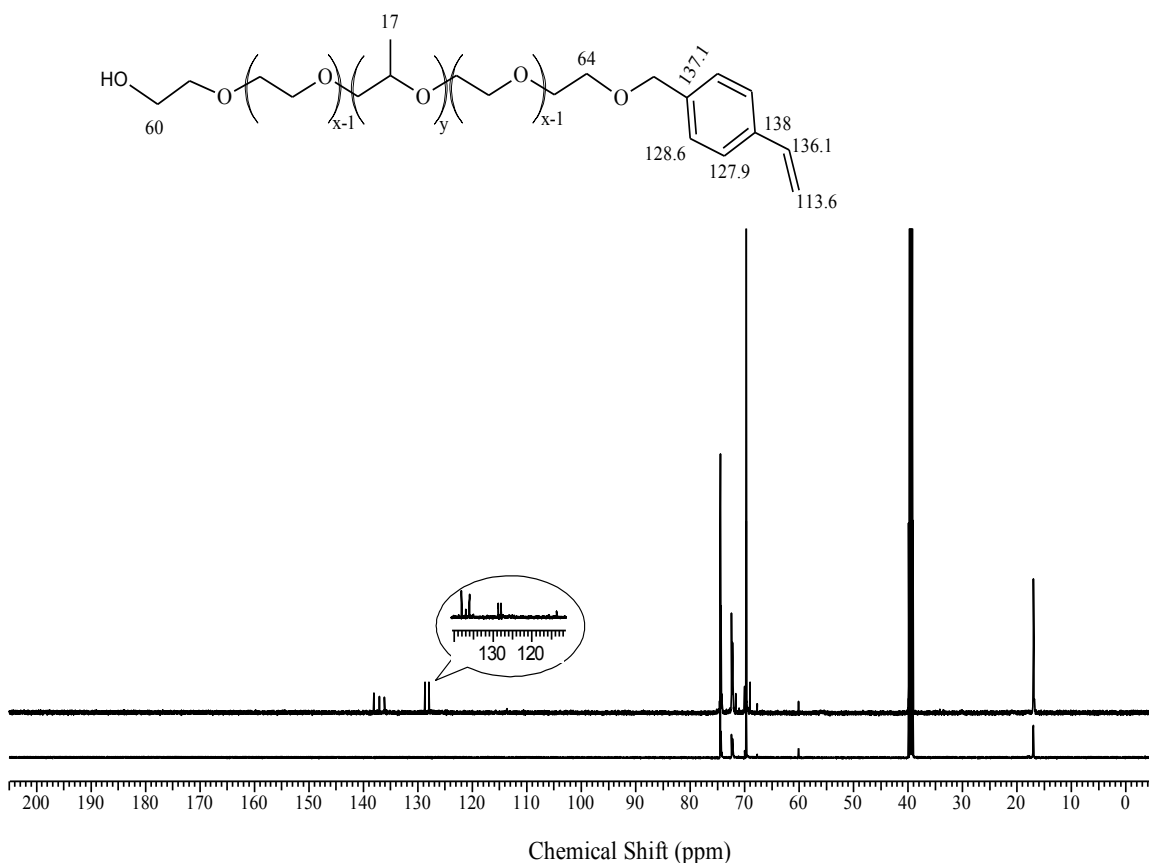


**Figure 3.2.** 600 MHz  $^{13}\text{C}$  solution NMR spectrum acquired with  $^1\text{H}$  decoupling of **(bottom)** pure P123 starting material and **(top)** styrene-functionalized **styrylP123** following reaction according to Scheme 1. End group signals are shown in the **styrylP123** inset, exhibiting the characteristic styrene between 125 and 140 ppm.

### 3.2.6 Preparation of polymer nanocomposites from acryP123 (or styrylP123) and SBA15acryP123 or SBA15styrylP123.

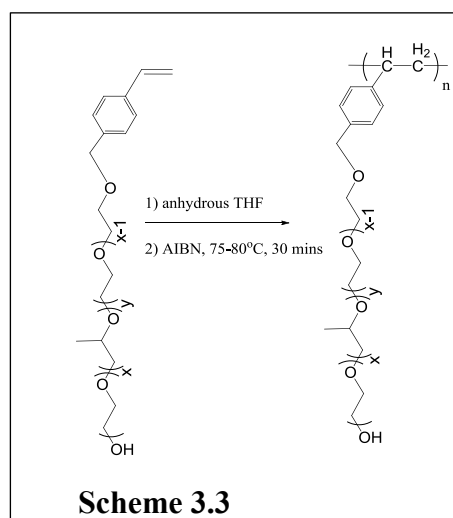
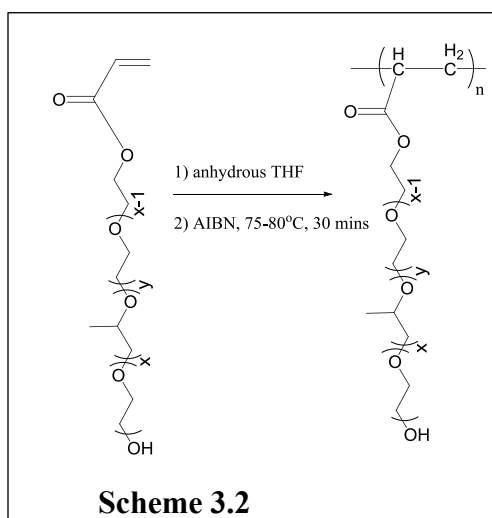
Polymer nanocomposites were obtained by polymerization of acrylate (shown in **Scheme 3.2**) or styrenated- P123 (shown in **Scheme 3.3**) via free radical polymerization method. To prepare control materials of reacted acrylated-P123 or styrenated P123 in the absence of mesoporous silica SBA15, 1 g of acrylated-P123 (or styrenated-P123) was dissolved in 1 ml of dry THF. The vial was purged with ultra-high purity argon to remove any oxygen. To this, 0.1 wt. % (with respect to the organic content) azobisisobutyronitrile (AIBN) was added and the temperature was then raised to 75-80°C. The reaction mixture was stirred for 30 minutes. The solvent was evaporated and the trace amount of solvent

was removed in vacuum oven at room temperature. As described below, a cross-linked polymer network was obtained from this control reaction. Table 3.2 below shows the composition of the silica and acryP123 to synthesize polymer nanocomposite with different organic contents.

**Table 3.2** Composition of polymer nanocomposites

<b>Composites from SBA15_acryP123</b>	<b>SBA15_acryP123 (g)</b>	<b>acryP123 (g)</b>
Polymer composite with 30% organic content	0.1	-
Polymer composite with 80% organic content	0.1	0.18
Polymer composite with 90% organic content	0.1	0.60
Polymerized acryP123	-	0.1

An essentially identical procedure was used when generating the composites or composite networks, except that the starting material was the dried as-synthesized SBA15acryP123 or SBA15styrP123 product. As synthesized, SBA15acryP123 or SBA15styrP123 contains 30-wt. % acrylated- or styrenated- P123, to which was added additional acryP123 or styrP123 in dry THF that would react with the silica-bound template molecules to generate the desired organic content nanocomposite. Subsequently, 0.1 wt. % (with respect to the organic content) azobis-isobutyronitrile (AIBN) was added and the temperature was then raised to 75-80°C. The reaction mixture was stirred for 15 minutes. We successfully prepared 10 and 20 wt% silica content composites/composite networks using this one-pot strategy.



**3.3 Linear Viscoelastic Measurements.** Linear viscoelastic measurements were performed with a Rheometric Scientific RSA II to measure loss and storage moduli as a function of strain using oscillating compression geometry. 10-mm parallel plate fixtures were used and measurements were made at room temperature with a gap size of ca.1.2 mm dimensions which are in the range where such measurements are expected to give  $G'$  and  $G''$ .<sup>13</sup> Walberer and McHugh describe how force data from this type of measurement was converted to  $G'$  and  $G''$  by making the lubrication approximation;<sup>12</sup> however no instrumental inertia correction was required for this diameter plate according to instrument readings as well as data supplied by the manufacturer.

**3.4 Small-Angle X-ray Scattering Measurements.** Small-angle X-ray scattering measurements were made in transmission with a SMax-3000 from Rigaku equipped with a  $\text{CuK}\alpha$  source and a 10 cm x 10 cm 2-D wire detector placed approximately 150 cm from the sample position. Silver behenate was used to determine the exact pixel to  $q$  ( $q=4\pi\sin\theta/\lambda$ ;  $\theta=0.5*\text{scattering angle}$ ,  $\lambda=1.54$  Å) conversion. Data were also corrected for pixel-to-pixel intensity variations as measured via exposing the plate to radiation emanating from an  $^{55}\text{Fe}$  source.

## 3.5 Results and Discussion

### 3.5.1 Generating mesoporous silica from the functionalized non-ionic template/macromers.

Nonionic triblock copolymers based on polyethylene oxide and a central polypropylene oxide block, denoted here as PEO-PPO-PEO and commonly referred to by their Pluronic trade name, have garnered widespread attention for synthesis of SBA-15 mesoporous silicas.<sup>14,15</sup> Here, we use Pluronic P123 (P123), HO-(PEO)<sub>20</sub>-(PPO)<sub>70</sub>-(PEO)<sub>20</sub>-H, as the template for SBA-15 formation, but employ functionalization methods to convert one end group to a reactive olefinic moiety. Vinyl benzyl chloride or acryloyl chloride, when reacted with P123 as described above in Scheme 1 and in the Experimental section, yields bifunctional styrP123 or acryP123, respectively. Reaction stoichiometries were selected to convert approximately one hydroxyl end-group per P123 chain, as described in **Figures 3.1** and **3.2**. In this way, each modified P123 is rendered bifunctional, and capable of subsequent polymerization through the olefinic end groups with surrounding template molecules, effectively as macromers. Given that the structure-directing characteristics of styrP123 and acryP123 are not known, we first established that both non-ionic surfactant macromers preserves P123's mesoporous silica structure-directing capabilities. Standard literature synthesis conditions<sup>14</sup> for SBA-15, using in separate experiments P123 versus styrP123 versus acryP123, yielded mesoporous materials both before and after calcination that are by all measures have shown the similar peaks. **Figure 3.3** compares the powder SAXS results from materials synthesized using the control P123 (**3.3a**, **3.3d**), the modified styrP123 (**3.3b**), and acryP123 (**3.3e**) prior to calcinations. Both the styrP123 and acryP123 materials exhibit the specific diffraction peaks consistent with published SBA-15 topologies. Finally, **Figures 3.3c** and **3.3f** show the results for the X-ray scattering in the polymerized composite, i.e., after reaction in which the styrP123 or acryP123 template macromers form the polymeric phase as shown in **Schemes 3.2** and **3.3**. Clearly, the mesoporous ordered silica structure is preserved following polymerization. Additional information about the polymerization step is discussed below.



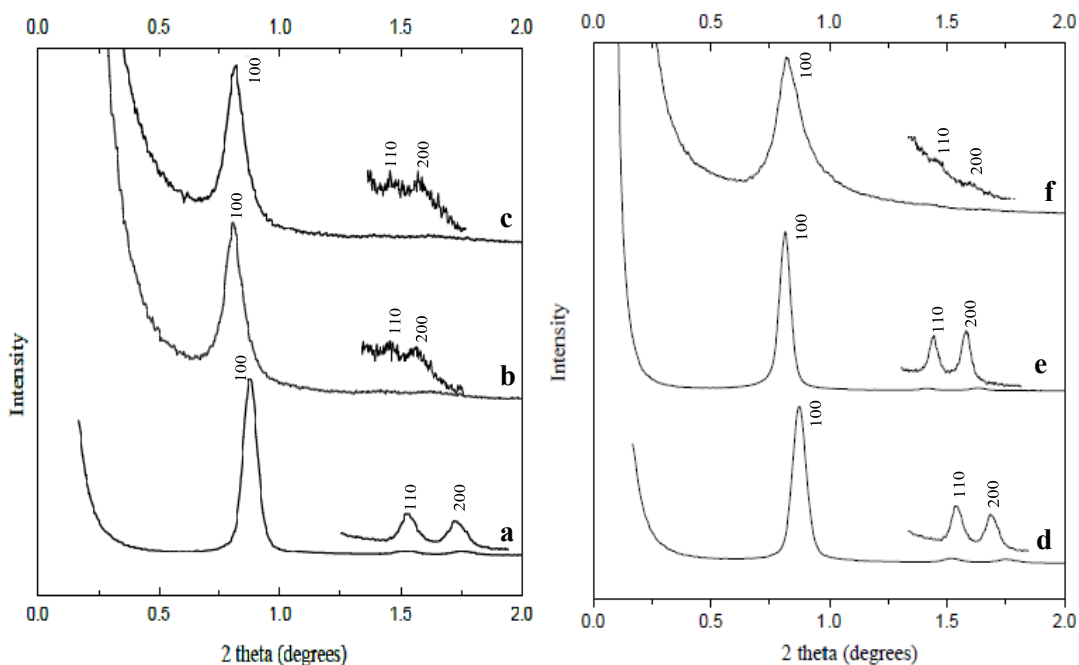


**Figure 3.3.** SAXS data for (a) SBA15P123; (b) SBA15\_styrP123; (c) SBA15\_styrP123 after polymerization of the astyrP123; (d) same as (a); (e) SBA15\_acryP123; and (f) SBA15\_acryP123 following polymerization. Diffractograms in (c) and (f) were acquired without calcination, and thus in the presence of the polymer product in and around the silica mesopores.

While creating calcined mesoporous silicas is not the end goal, the BET surface areas and pore size distributions following calcination are key indicators that the modified templates still function as templates, and compliment the SAXS data discussed above. The styrenic group on one end of the styrP123 templates does not alter the ability to form micelles in the aqueous environment, or to template crystallization of ordered mesoporous silica due to the fact that it produces the high surface of the calcined and dried styrP123SBA material.

For acryP123 template synthesis, the resulting mesoporous silica surface area was 930 m<sup>2</sup>/g which is similar to that expected for SBA-15 structures synthesized from the unfunctionalized P123. Average pore diameters, and pore size distributions, were measured via BJH N<sub>2</sub> adsorption/desorption experiments<sup>16</sup> and were essentially similar for P123, styrP123, and acryP123-templated silicas. Average pore diameters were 3.2, 3.2, and 3.0 nm, respectively.

**Figure 3.4** shows the adsorption-desorption profiles (on left) and pore size distribution (on right) of mesoporous silica SBA15, SBA15\_acryP123, and SBA15\_styrP123.

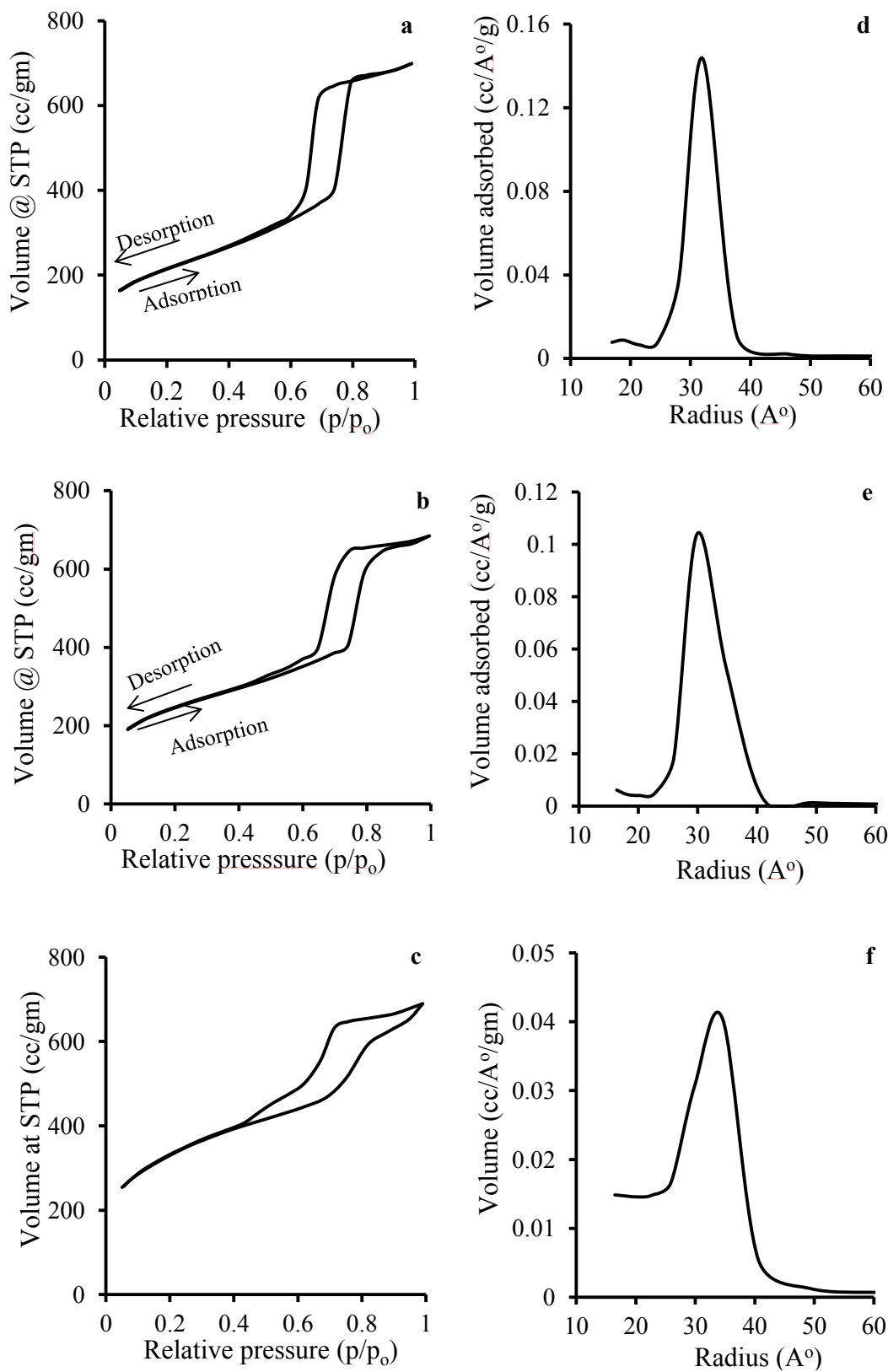


**Figure 3.4.** Adsorption-desorption curves (on left) and pore size distribution (on right) of SBA15\_P123 (a, d); SBA15\_acryP123 (b, e); and SBA15\_styrP123 (c, f) respectively.

**Figures 3.5a-c** shows representative TEM results for SBA-15 prepared from P123 in the traditional manner (SBA15\_P123), SBA-15 prepared from acryP123 (SBA15\_acryP123), and SBA-15 prepared from styrP123 (SBA15\_styrP123). In all three cases, the characteristic ca. 4 nm hexagonally-arrayed channels are observed. Again, the goal with these detailed characterizations is to show that modified surfactant macromers preserve SBA-15 templating, while providing the added post-synthetic polymerization capability needed to form a continuous organic phase both within and outside of the mesoporous silica particles. Note that the scale for **Figure 3.5b** and **3.5c** is twice that shown in **3.5a**.

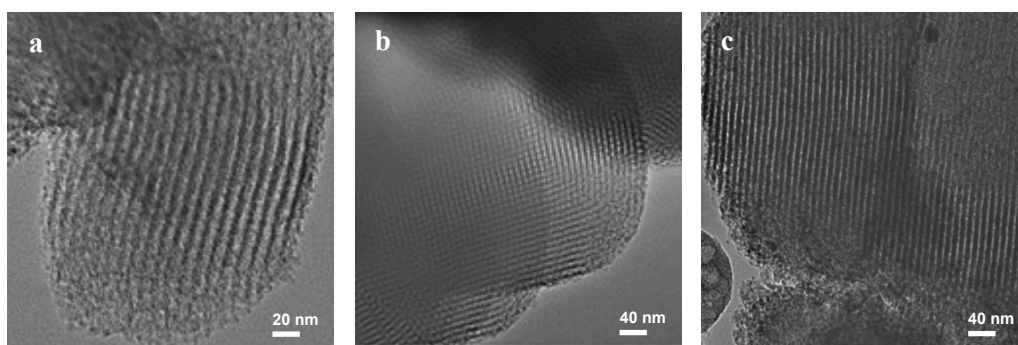


**Figure 3.5.** TEM micrographs for **(a)** SBA15P123, **(b)** SBA15\_acryP123, and **(c)** SBA15\_styrP123. Images (a) is at , at 100,000 $\times$  magnification, while (b) and (c) is at 50,000 $\times$

The SBA15\_acryP123 and SBA15\_styrP123 composites, as synthesized, contain 30 wt% organic content as defined by the initial surfactant/TEOS reaction stoichiometry. However, adding additional acryP123 or styrP123 added at the time of polymerization yields final products with much higher organic content. In this way, we have systematically and repeatedly generated composites with up to 20 wt% silica content, as verified by TGA analysis on the final washed and dried products. Representative TGA results for the composites made from SBA15\_acryP123 (i.e., the same dried starting materials used to generate the swollen samples in **Figure 3.7**) are shown in **Figure 3.6**, with silica contents of 0, 10, 20, and 70 wt%. Figure 3.6a also shows the control experiment for the polymerization of pure acryP123; similar results were obtained for styrP123-generated composites.

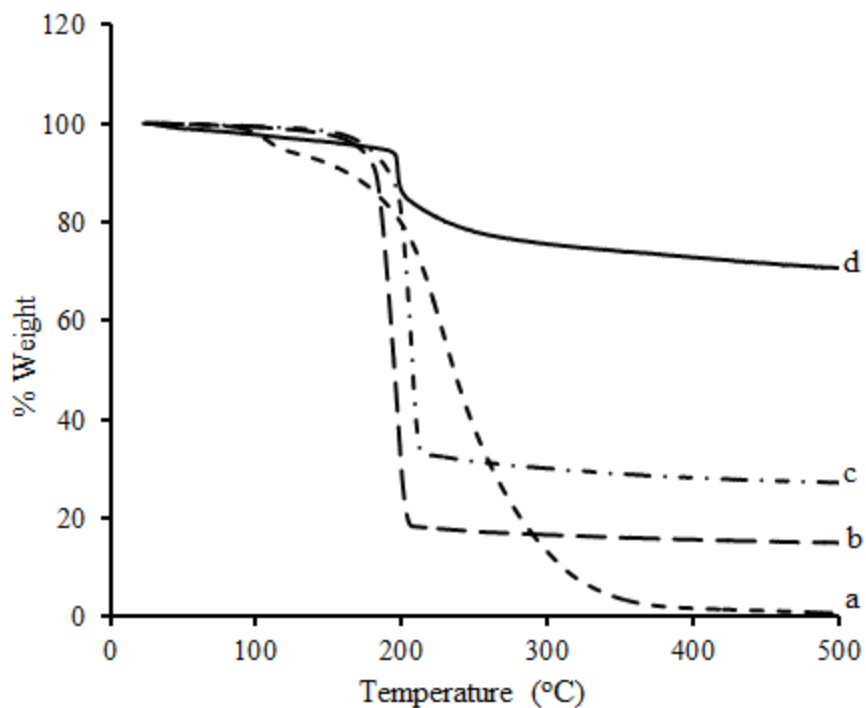


**Figure 3.6.** TGA results for polymer nanocomposites made using acryP123 composites with **a)** 0% **b)** 10 % ; **c)** 20 %; and **d)** 70 wt% silica content.

Shown in **Figure 3.7** are a series of solvent-swelling images in tetrahydrofuran, comparing pure acryP123 and composites derived from polymerizing acryP123 in the mesoporous host. From **Figure 3.7a**, we observe that there is essentially no swelling for acryP123, but polymerized acryP123 (**3.7b**) exhibits a large volume-swelling ratio. The organic/inorganic composites prepared from the polymerization of the acryP123 are shown in **3.7c-3.7e**; all exhibit significant solvent swelling and none were soluble in any common solvent.

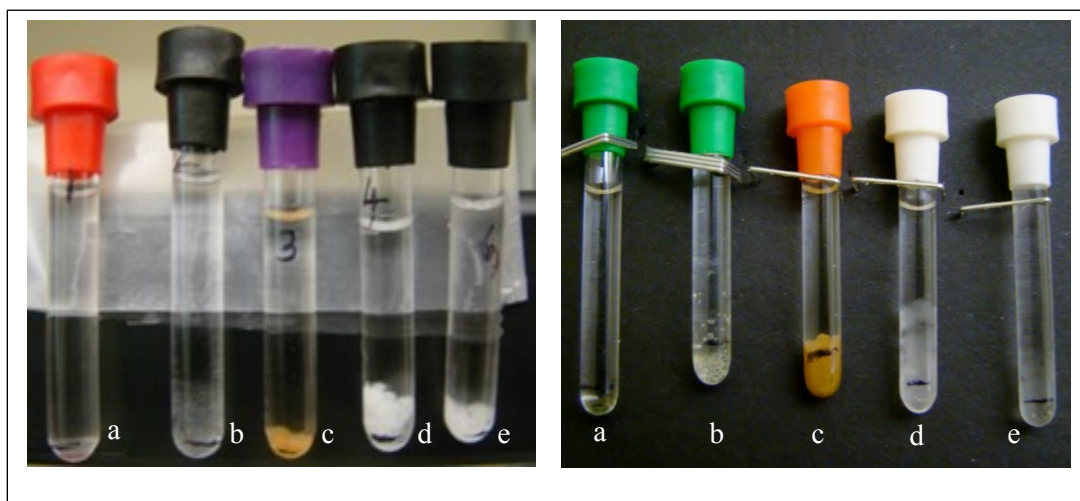


**Figure 3.7.** Images acquired for THF-swollen of polymer nanocomposites using acryP123 (**on left**) and styP123 (**on right**) of **a**) respective functionalized P123 i.e. acryP123 on left and styP123 on right **b**) 0% **c**) 70 % t; **d**) 10 %; and **e**) 20 wt% silica content

**Figure 3.8** shows a similar set of CP/MAS results for the acryP123/SBA15 system reveals that polymerization of the acryP123 templates takes place inside and around the SBA-15. The 30 wt% composite in **3.8b** exhibits a complex, broad signal for the carbonyl group, ranging from 164-180 ppm, which is absent in the unpolymerized sample (**3.8a**), and is also not visible in the higher organic content composite in **3.8c**. This indicates that the polymerization does occur between adjacent macromers within the constrained SBA-15 channels in the as-prepared composite, prior to adding any additional acryP123, which is important since polymer chain connectivity through the SBA-15 channels is required if the organic phase is to be continuous throughout the material. Again, the swollen network results in Figure **3.7c** clearly indicate that polymerization has also occurred outside of the SBA-15 channels as well even for the 30 wt% composite to which no additional acryP123 was added prior to polymerization. The carbonyl signals are not observed in the CP spectrum of composite with 80 wt% of organic content as the bulk-averaged behavior of organic phase is much more mobile than the 30 % material, the latter of which has the majority of its chain density within the SBA-15 channels.

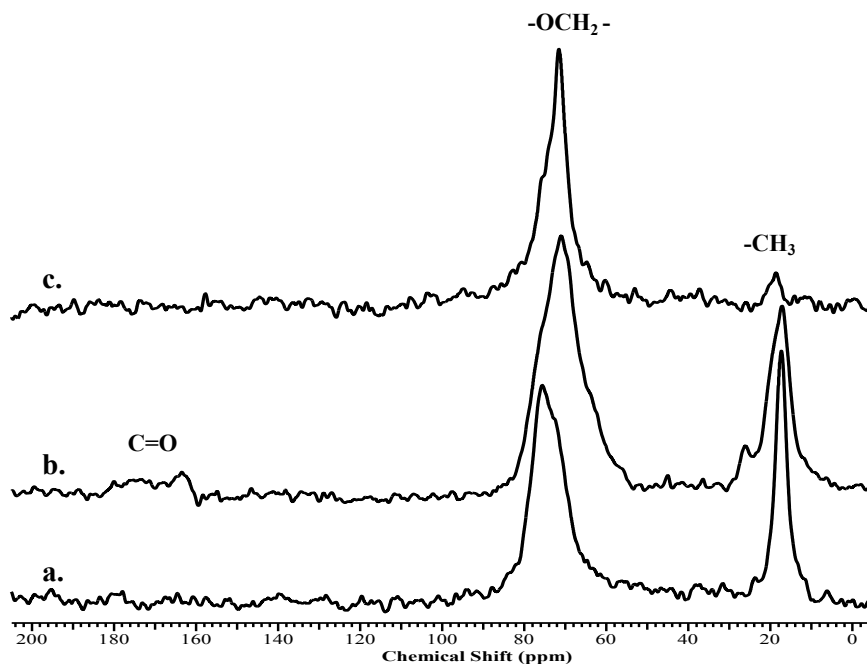


**Figure 3.8.** Solid-state  $^1\text{H}\rightarrow^{13}\text{C}$  CP (cross-polarization)/MAS spectra for (a) the acryP123 template in uncalcined SBA-15 following synthesis but prior to polymerization, (b) the organic fraction generated by polymerizing the acryP123 structure-directing agents inside and around the SBA-15 following crystallization, corresponding to a 30 wt% polymer composite, and (c) same starting material as in (a) but with additional acryP123 added prior to polymerization, resulting in a polymerized composite with 80 wt % organic fraction .

The rheological experiments i.e. strain sweep and frequency sweep were performed at room temperature on a parallel plate RSAII rheometer from TA instruments on both acryP123 (**Figure 3.9**) and styrP123 (**Figure 3.10**) nanocomposites. Linear viscoelastic regimes (LVR) were experimentally determined at 1Hz frequency with variable strain measurements (0.01 to 10%). The top row of **Figure 3.9** shows that the LVR of the nanocomposites are in between 0.01% to 0.15% strain of acryP123 nanocomposites. In accordance with the strain sweep data, frequency sweep data was then collected at 0.15% strain and is shown in the bottom row of **Figure 3.9**. The frequency sweep data indicates that the modulus increases as the increase in content of silica of polymer nanocomposites. Also, the storage and loss modulus of the

nanocomposites are independent of the frequency which draws the conclusion that the chemistry leads to the formation of perfectly network nanocomposites.

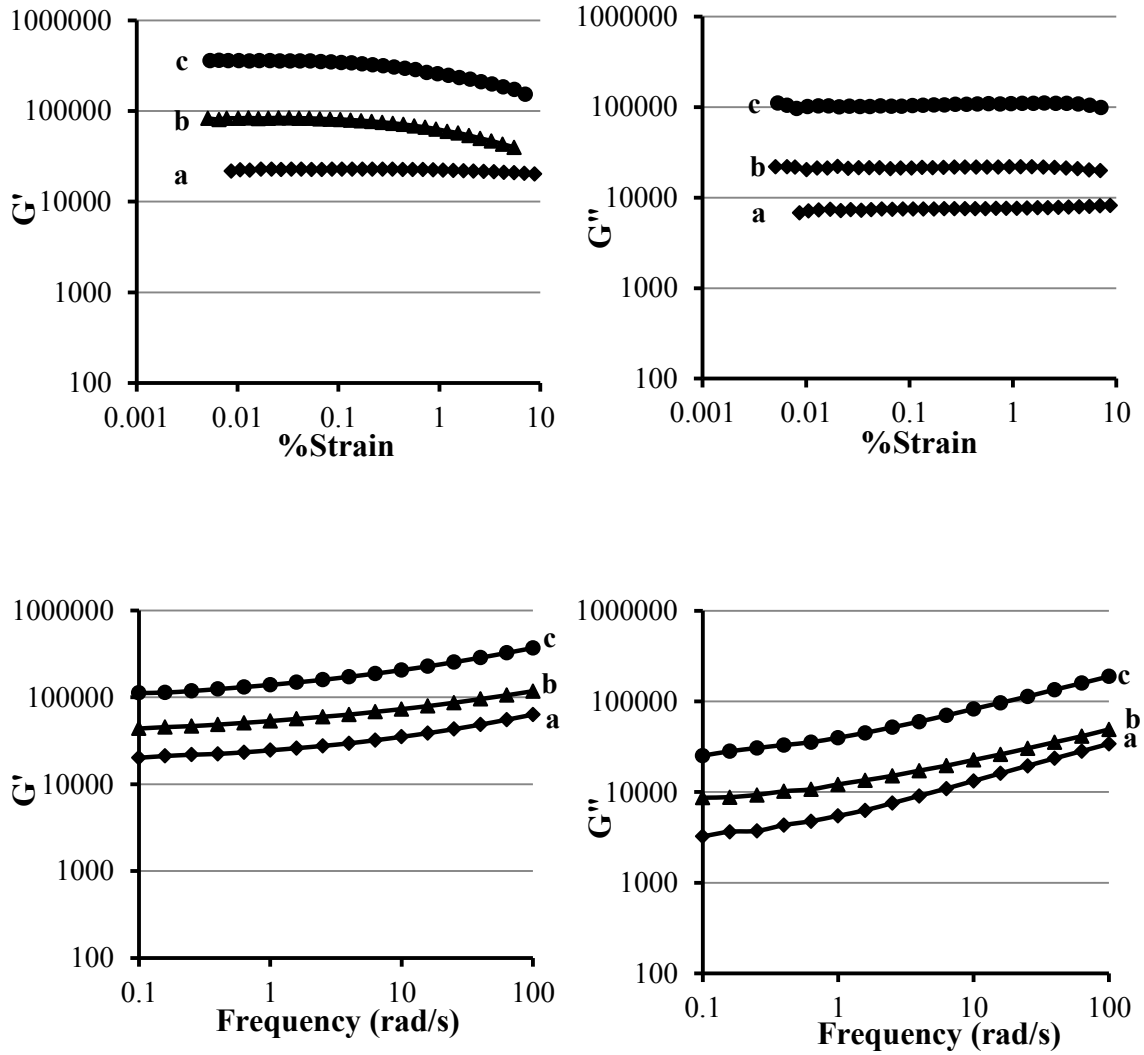


**Figure 3.9.** Storage moduli ( $G'$ ) and loss moduli ( $G''$ ) collected from strain sweep (**top row**) and frequency sweep (**bottom row**) of acryP123 nanocomposite networks with a) 0%, b) 10%, and c) 20 wt% silica content.

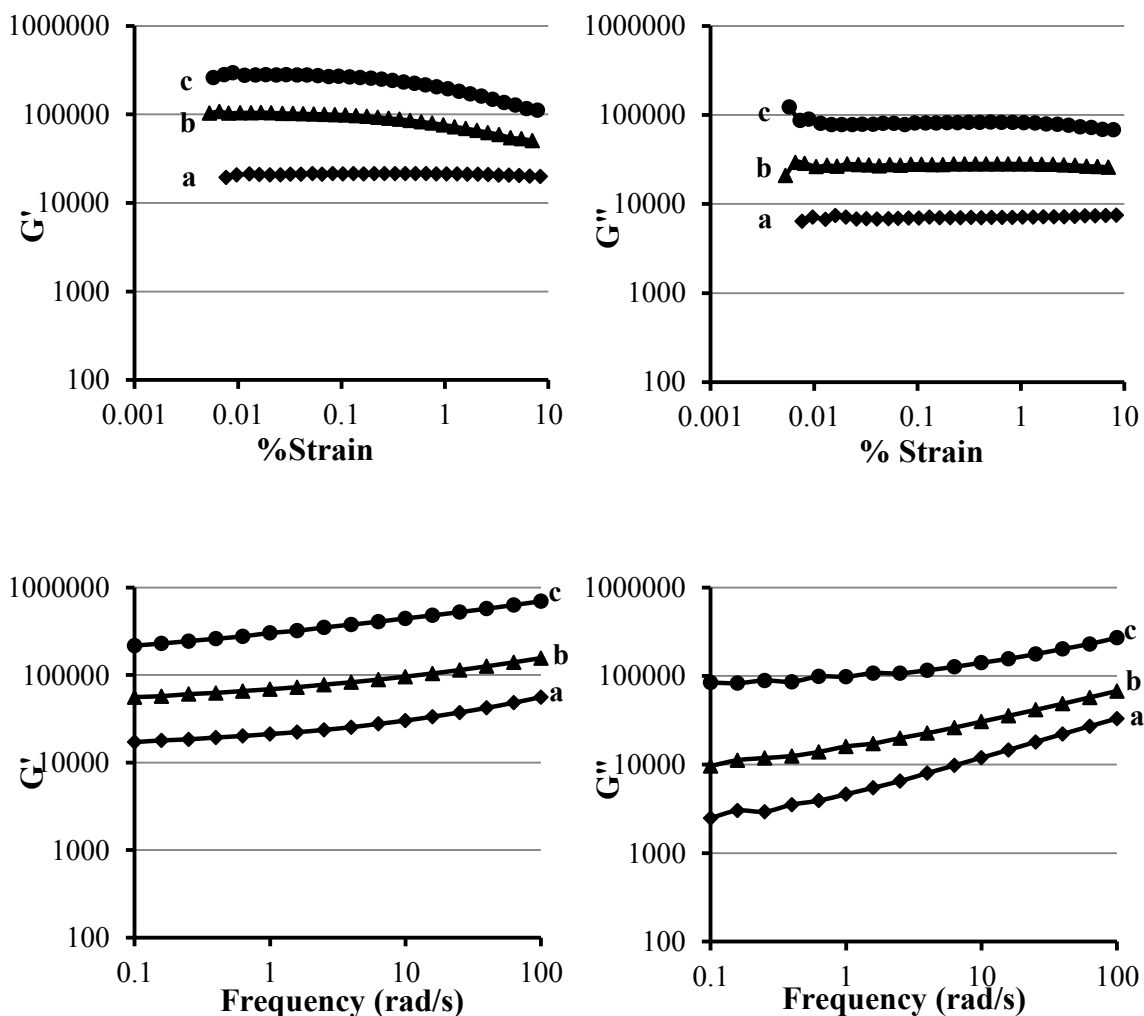


**Figure 10.** Storage moduli ( $G'$ ) and loss moduli ( $G''$ ) collected from strain sweep (**top row**) and frequency sweep (**bottom row**) of styrene-poly(2-vinylpyridine) (styrP123) nanocomposite networks with a) 0%, b) 10%, and c) 20 wt% silica content.

### 3.6 Conclusions

A novel route to organic/inorganic composite materials has been introduced, which utilizes end-group functionalization of existing structure-directing agents to enable self-assembly synthetic methods that generate intimately-mixed nanocomposites. Using acrylate- or styrenate-functionalized P123 as a template, we have shown that crystallization of SBA-15 is preserved but that following the crystallization, the template readily polymerizes to form a composite



containing high molecular weight polymer filling and surrounding the SBA-15 crystallites in an intimately mixed arrangement. The acrylate-functionalized P123/styrenated-functionalized P123 route also introduces network properties to the nanocomposites. The network showed increase in storage and loss modulus with increase in silica content. This new self-assembly approach has driven us to synthesize new non-ionic polymer surfactant molecules that are not based on P123, but include polyethylene oxide, polycaprolactone, and polylactide blocks with end group functionalization to telechelic macromers. Such telechelics should enable synthesis of polymer composites that are both biocompatible and truly bioremedial. These new materials, as well as thorough investigations of physical and mechanical properties for the composites described here, will be discussed in the next chapter.

### 3.7 References

1. Abdalla, Z. E. A.; Li, B.; Tufail, A. Direct Synthesis of Mesoporous  $(C_{19}H_{42}N)_4H_3(PW_{11}O_{39})/SiO_2$  and its Catalytic Performance in Oxidative Desulfurization. *Colloids Surfaces A: Physicochem. Engineer. Aspects* **2009**, *341*, 86-92.
2. Ooi, Y.S.; Bhatia, S. Aluminum-Containing SBA-15 as Cracking Catalyst for the Production of Biofuel from Waste Used Palm Oil. *Microporous Mesoporous Mat.* **2007**, *102*, 310-317.
3. Pasqua, L., Cundari, S.; Ceresa, C.; Cavaletti, G. Recent Development, Applications and Perspectives of Mesoporous Silica Particles in Medicine and Biotechnology. *Current Med. Chem.* **2009**, *16*, 3054-3063.
4. Zornoza, B., S.; Irusta, C.; Tellez; Coronas, J. Mesoporous Silica Sphere Polysulfone Mixed Matrix Membranes for Gas Separation. *Langmuir*, **2009**, *25*, 5903-5909.
5. Zou, H.; Wu,S.; Shen, J. Polymer/Silica Nanocomposites: Preparation, Characterization, Properties, and Applications. *Chem. Rev.* **2008**, *108*, 3893–3957.

6. Burkett, S. L.; Sims, S. D.; Mann, S. Synthesis of Hybrid Inorganic-Organic Mesoporous Silica by Co-condensation of Siloxane and Organosiloxane Precursors. *Chem. Commun.* **1996**, 1367–1368.
7. Macquarrie, D. J. Direct Preparation of Organically Modified MCM-41 type Materials. Preparation and Characterization of aminopropyl-MCM and 2-Cyanoethyl-MCM. *Chem. Commun.* **1996**, 1961 – 1962.
8. Kruk, M.; Dufour, B.; Celer, E. B.; Kowalewski, T.; Jaroniec, M.; Matyjaszewski, K. Grafting Monodisperse Polymer Chains from Concave Surfaces of Ordered Mesoporous Silicas. *Macromolecules* **2008**, *41*, 8584-8591.
9. Audouin, F.; Blas, H.; Pasetto, P.; Beaunier, P.; Boissière, C.; Sanchez, C.; Save, M.; Charleux, B. Structured Hybrid Nanoparticles via Surface-Initiated ATRP of Methyl Methacrylate from Ordered Mesoporous Silica. *Macromol. Rapid Comm.* **2008**, *29*, 914-921.
10. Anwender, R.; Nagl, I.; Zapilko, C.; Widenmeyer, M. Methyl Methacrylate Polymerization at Samarium(II)-Grafted MCM-41. *Tetrahedron* **2003**, *59*, 10567-10574.
11. Landry, C. J. T.; Coltrain, B. K.; Brady, B. K. In-Situ Polymerization of Tetraethylorthosilane in Poly(methyl methacrylate): Morphology and Dynamic Mechanical Properties. *Polymer* **1992**, *33*, 1486-1495.
12. Petrovic, Z. S.; Javni, I.; Waddon, A.; Banhegyi, G. Structure and Properties of Polyurethane–Silica Nanocomposites. *J. Appl. Polym. Sci.* **2000**, *76*, 133-151.
13. Walberer, J. A.; McHugh, A. J. The Linear Viscoelastic Behavior of Highly Filled Poly(dimethylsiloxane) Measured in Shear and Compression. *J. Rheol.* **2001**, *45*, 187-201.
14. Zhao, D.; Feng, J.; Huo, Q.; Melosh, N.; Fredrickson, G. H.; Chmelka, B. F.; Stucky, G. D. Triblock Copolymer Syntheses of Mesoporous Silica with Periodic 50 to 300 Angstrom Pores. *Science* **1998**, *279*, 548-552.

15. Ruthstein, S.; Schmidt, J.; Kesselman, E.; Talmon, Y.; Goldfarb, D. Resolving Intermediate Solution Structures During the Formation of Mesoporous SBA-15. *J. Am. Chem. Soc.* **2006**, *128*, 3366-3374.
16. Tompsett, G. A.; Krogh, L.; Griffin, D. W.; Conner, W. C. Hysteresis and Scanning Behaviour of Mesoporous Molecular Sieves. *Langmuir* **2005**, *21*, 8214-8225.

## CHAPTER IV

### CREATING POLYMER TEMPLATES AND THEIR USE IN THE IN-SITU SYNTHESIS OF BIODEGRADABLE NANOCOMPOSITES

**Abstract.** A biodegradable polyethyleneoxide-polycaprolactone-polyethyleneoxide (PEO-PCL-PEO or PECE) triblock polymer was synthesized as a structure-directing agent for high-surface area silica formation. Systematic end-group functionalization of the triblock polymer, prior to its use as a structure-directing agent for high-surface area silica growth, imparts an additional reactive function that is exploited to grow a continuous organic phase within and around the silica particles. With this strategy, the biodegradable triblock is both a template and a macromer whose dual function leads to in-situ generation of an intimately mixed biopolymer/nanoporous-silica nanocomposite that is biodegradable and in theory biocompatible, and whose modulus is comparable to other non-biodegradable materials.

## 4.1 Introduction

Creating new hybrid materials able to satisfy multiple performance constraints in engineering, biomedical, and consumer product applications requires novel synthetic strategies. Polymer composites, or nanocomposites, composed of natural or synthetic polymers and natural or synthetic siliceous sources, including clays, have been targeted as promising materials during the last decade.<sup>1,2</sup> Most commonly, silica-based composites are prepared via sequential synthetic schemes, in which the silica component is prepared separately, and then mixed with the organic components to create the composite. Achieving homogeneous and intimately mixed distributions of the organic and inorganic constituents is challenging, especially for cases where the polymer (at its final molecular weight) and inorganic reinforcing agent of choice are combined via melt- or solvent-mixing. This limitation may be addressed by introducing the monomer and completing the polymerization in the presence of the inorganic reinforcing agent<sup>3-7</sup> or by grafting the mesoporous silica particles together using the organic-phase monomer.<sup>9-11</sup> One area where composites are poised to have increased impact is in the design of materials that are biocompatible and biodegradable. New synthetic routes for in-situ/self-assembled preparation of composites from constituent precursors could enable new applications.

In this contribution, we propose an alternative approach where both the inorganic and organic phases self-assemble from their respective building blocks, each in the presence of the other, thereby ensuring an intimately mixed homogeneous product that cannot phase segregate. Unlike previous reports, there is no chemical grafting to the interior or exterior of the nanoporous silica surface, nor is there any separation of the components at any time during the synthesis. A key component of this work is the creation of polymerizable biodegradable structure-directing agents that can template formation of high-surface area mesoporous silica, and react with other template molecules to generate a biodegradable organic network through, around, and in between the silica particles in an in-situ approach. The concept of functional and reactive surfactants,<sup>12</sup>

often referred to as “surfmers”,<sup>13-15</sup> is not new in the field of micelle polymerization, but their successful application to synthesis of ordered silica-based composite materials has been limited to ionic small-molecule templates.<sup>16,17</sup> Non-ionic, biodegradable, biocompatible macromolecular surfactants that serve both the structure-directing and “monomer” role, and whose structure and reactivity can be controlled through rational end-group chemistries, have not been reported. In this contribution, we describe the synthesis and application of end-group functionalized EO<sub>23</sub>-CL<sub>16</sub>-EO<sub>23</sub> (polyethylene oxide-polycaprolactone-polyethylene oxide or **PECE-4K**, where 4K denotes the molecular weight of the template) and EO<sub>45</sub>-CL<sub>16</sub>-EO<sub>45</sub> (**PECE-6K**) triblock polymers, which serve the dual function of both template and macromer in chemistry that leads to hybrid nanocomposite biomaterials. After nanoporous silica particles form around the triblock polymer micelles, the triblock polymer chains can react to yield a high molecular-weight continuous phase originating from within the mesoporous silica channels. Details for the triblock synthesis, functionalization, and nanocomposite formation are given in the following sections, as well as preliminary information on the overall physical properties of the biopolymer nanocomposite.

## **4.2 Experimental**

### **4.2.1 Materials**

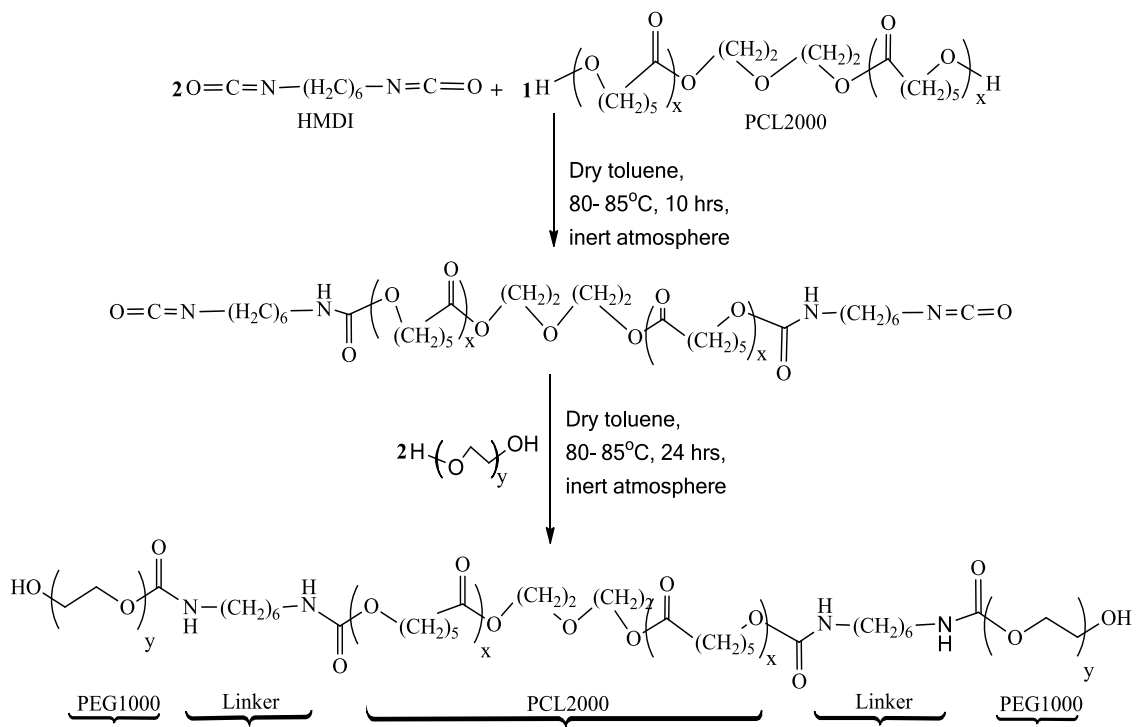
Polyethylene glycols of  $M_n=2000$  g/mol and  $M_n=1000$  g/mol were purchased from Alfa Aesar. Polycaprolactone diol ( $M_n=2000$ ) was purchased from Sigma Aldrich and used as received for triblock copolymer synthesis. Acryloyl chloride was purchased from Alfa Aesar. All organic solvents were obtained from Pharmco-AAPER.

### **4.2.2 Characterization**

Surface area of mesoporous silica was determined on Nova2200e Quantachrome instruments. Transmission electron micrographs were acquired on JEOL JEM-2100 with Evex EDS. Scanning electron micrographs were acquired from FEI Quanta 600 field emission gun

ESEM with Evex EDS and HKL EBSD. 400 MHz liquid NMR spectrometer (Varian) was used to determine  $^1\text{H}$  NMR (in  $\text{CDCl}_3$ ) to determine the functionalized PECE at room temperature at the spinning speed of 20Hz.

**4.2.3 Synthesis of PECE-4K and PECE-6K triblock polymers.** PECE synthesis was carried out in solution, using as-received polycaprolactone diol (Sigma, molecular weight = 2000 g/mol) and polyethylene glycol (Alfa Aesar, molecular weight = 1000 for PECE-4K and molecular weight = 2000 g/mol for PECE-6K) as the primary reagents.<sup>18-20</sup> In a typical synthesis, 2 mmol of hexamethylene diisocyanate (HMDI) and 15 ml of dry toluene were mixed and heated to 60-65°C under stirring and in an argon atmosphere. Then, 50 ml of a 1-mmol polycaprolactone-diol solution was added drop wise for one hour. The reaction was heated to 80-85°C and held for 10 hours. This reaction produced polycaprolactone terminated on each chain end with a reactive hexamethylene isocyanate group. Subsequent addition of 50 ml of a 2 mmol polyethylene glycol solution, at temperature, yielded the triblock copolymer after 24 hours. (A one-pot synthesis easily avoids the problem of moisture contamination and reaction of the polycaprolactone hexamethylene isocyanate prepolymer, which leads to cross-linked gels). After isolation by precipitation into diethyl ether, the polymer was dissolved in dichloromethane and re-precipitated by slowly adding diethyl ether. The solvent was removed by rotary evaporation, followed by 24 hours at 50°C in a vacuum oven to remove any residual solvent. The triblock copolymer PECE with 95% yield was isolated. The key step in the reliable synthesis of the triblock is the use of the hexamethylene diisocyanate linker. The overall reaction is shown in **Scheme 4.1** for the PECE-4K system, and was similar for the PECE-6K synthesis.



**Scheme 4.1.** Synthesis of triblock copolymer PECE

Infrared spectroscopy on the isolated polycaprolactone product after reaction with HDMI, but prior to ethylene glycol addition, showed the characteristic peak for the  $-\text{N}=\text{C}=\text{O}$  stretch at  $2280 \text{ cm}^{-1}$ , which disappeared after reaction with the ethylene oxide blocks.  $^1\text{H}$  solution NMR confirmed that the triblock had been formed. Specifically, the ratio of the PEG  $\text{CH}_2$  hydrogen signal to that of the  $\text{CH}_2$  group alpha to the PCL carbonyl carbon was 5.7:1, which is statistically identical to the expected ratio of 5.65:1 for the  $\text{EO}_{23}\text{-CL}_{16}\text{-EO}_{23}$  (PECE-4K) product. The molecular weight from NMR analysis of the PECE-6K also agreed with the theoretical expectation for an  $\text{EO}_{45}\text{-CL}_{16}\text{-EO}_{45}$  triblock, in that the ratio of PEG  $\text{CH}_2$  hydrogen signal to that of the  $\text{CH}_2$  group alpha to the PCL carbonyl carbon in PECE-6K was 11.25:1, statistically identical to the expected 11.3:1. Complete infrared and quantitative NMR data are provided in the appendix C1. Analysis of the peak areas for the amide hydrogen signal in the HDMI linker



confirms that there are four such hydrogens per polymer, again in agreement with expectations for the triblock product as shown in **Scheme 4.1**.

**4.2.4 PECE end-group functionalization to form acrylated-PECE.** In order to render each PECE chain reactive, the hydroxyl end groups were converted to an acrylate moiety. One millimole of PECE (4K or 6K) was dissolved in 100 ml of dry toluene under a dry argon atmosphere in a two-necked round bottom flask, to which was added 1.1 mmol of acryloyl chloride and 1.1 mmol of triethyl amine. This reaction mixture was refluxed for 24 hours in inert atmosphere. Triethylammonium chloride salt formed by the reaction was removed via filtration. The filtrate containing acrylated PECE (4K or 6K) was then precipitated in cold hexane, followed by dissolution in toluene and re-precipitation in cold hexane. The product was dried at room temperature overnight in a vacuum oven. Functionalized PECE with 85% yield was isolated. NMR data provided in the appendix **C2** confirm the presence of the acrylate moiety on the PECE's. The molar ratios were selected such that on average, one hydroxyl end-group per chain would be functionalized, but of course the final product will be a mixture of chains containing zero, one, and two acrylate end groups per chain.

**4.2.5 PECE-templated porous-silica formation.** The molar composition for the targeted synthesis of mesoporous silica was tetraethoxyorthosilicate (TEOS) : PECE/acrylated-PECE : HCl : H<sub>2</sub>O = 1 : 0.016 : 5.54 : 182.82. PECE (2.76 gms for PECE4K and 4.14 gms for PECE6K) was dissolved in 40 ml of tetrahydrofuran (THF), as this weight of copolymer is not completely soluble in water. To this mixture was added 30 ml of deionized water, which was then stirred for three hours. Subsequently, 113 ml of 2.1 M HCl was added dropwise to the solution. After stirring for two hours, the solution was heated to 40°C and 9 g of TEOS was added, followed by an additional 48 hours stirring. The mixture was then transferred to a Parr reactor and heated under static conditions for 24-48 hours at 100°C. After cooling, the silica product was filtered and washed with 40 milliliters of THF, excess deionized water, and then dried on the bench

overnight. The same procedure was followed for pure PECE or acrylated-PECE. TGA measurements showed that the as-prepared silica contained 14 wt% PECE6K. For the surface-area and porosity characterization of the nanoporous silica discussed below, the PECE or acrylated-PECE template was removed by calcination at 550°C.

**4.2.6 Preparation of polymer nanocomposites from PECE/silica products.** To prepare control materials of reacted acrylated-PECE6K in the absence of porous silica, 1 g of acrylated-PECE6K was dissolved in 1 ml of dry THF. The vial was purged with ultra-high pure argon to remove any oxygen. To this, 0.1 wt. % (with respect to the organic content) azobis-isobutyronitrile (AIBN) was added and the temperature was then raised to 75-80°C. The reaction mixture was stirred for 15 minutes. The solvent was evaporated and the trace amount of solvent was removed in vacuum oven at room temperature. As described below, a cross-linked polymer network was obtained from this control reaction. Table 4.1 below shows the composition of the silica and acryPECE to synthesize polymer nanocomposite with different inorganic contents.

**Table 4.1.** Composition of polymer nanocomposites

Polymer composites with silica contents	MSacryPECE6k (g)	acryPECE6k (g)
0	-	1
7.5	0.1	3.34
5	0.1	1.62
10	0.1	0.76
12.5	0.1	0.588
15	0.1	0.473

An essentially identical procedure was used when generating the composites or composite networks, except that the starting material was the dried as-synthesized PECE6K/silica product. As synthesized, the starting composites contained 14-wt. % acrylated-PECE6K, to which was added additional acrylated-PECE6K that would react with the silica-bound template molecules to generate the desired organic content nanocomposite. Subsequently, 0.1 wt. % (with

respect to the organic content) azobis-isobutyronitrile (AIBN) was added and the temperature was then raised to 75-80°C. The reaction mixture was stirred for 30 minutes. We successfully prepared 5, 7.5, 10, 12.5, and 15 wt. % silica content composites/composite networks using this one-pot strategy.

**4.3 Linear Viscoelastic Measurements.** Linear viscoelastic measurements were performed with a Rheometric Scientific RSA II to measure loss and storage moduli as a function of temperature using oscillating compression geometry. 10-mm parallel plate fixtures were used and measurements were made at 60°C with a gap size of 1.2 mm, dimensions which are in the range where such measurements are expected to give  $G'$  and  $G''$ .<sup>21</sup> Walberer and McHugh describe how force data from this type of measurement was converted to  $G'$  and  $G''$  by making the lubrication approximation;<sup>21</sup> however no instrumental inertia correction was required for this diameter plate according to instrument readings as well as data supplied by the manufacturer.

**4.4 Small-angle X-ray Scattering Measurements.** Small-angle x-ray scattering measurements were made in transmission with a SMax-3000 from Rigaku equipped with a  $\text{CuK}\alpha$  source and a 10 cm x 10 cm 2-D wire detector placed approximately 150 cm from the sample position. Silver behenate was used to determine the exact pixel to  $q$  ( $q=4\pi\sin\theta/\lambda$ ;  $\theta=0.5*\text{scattering angle}$ ,  $\lambda=1.54 \text{ \AA}$ ) conversion. Data were also corrected for pixel-to-pixel intensity variations as measured via exposing the plate to radiation emanating from an  $^{55}\text{Fe}$  source.

## 4.5 Results and Discussion

Two key questions must be addressed in order to determine if the in-situ and dual structure-directing agent/macromer approach is a successful method for general application. First, does the end group-functionalized PECE copolymer template the formation of high-surface area silica?<sup>22,23</sup> Second, are the acrylate end-groups sufficiently reactive and accessible to generate a continuous organic phase using reasonable chemistry? In addition, one would like to

know if the overall organic content can be varied systematically, if the physical properties are attractive, and if they track the composition distribution in a predictable manner. Triblock copolymers made from ethylene-oxide and propylene oxide segments, known commercially as Pluronics<sup>®</sup>, are well known as structure-directing agents in the synthesis of ordered mesoporous silica, including SBA-15.<sup>17-19</sup> These templates are usually removed from the porous silica following its synthesis either by high-temperature calcination or chemical methods, and more importantly, they are neither biocompatible, biodegradable, nor polymerizable macromolecules.

As described in the experimental section and Scheme 1, PECE molecular weights of 4K and 6K were assembled from their constituents. Two different values were used to determine if the average pore diameter of the resulting high-surface area silica could be varied, based on the assumption that the size of the micelle formed by the PECE template depended on the molecular weight. Results from nitrogen adsorption BET surface area measurements and BJH average pore diameter calculations are given in Table 1 for silica made from the PECE and the acrylated PECE macromers. The PECE templates were removed via calcination prior to surface area and porosity characterization. **Table 4.2** clearly shows the PECE structure-directing agents template the formation of high-surface area silica, and the average pore diameter for the PECE-6K induced synthesis exceeds that of the PECE-4K process. The surface areas reported in Table 1 are in the expected range for mesoporous silicas; surface areas for known systems like MCM-41<sup>24-27</sup> and SBA-15<sup>28,29</sup> are reported in the literature ranging from 700-1100 m<sup>2</sup>/g, depending on synthesis conditions.

**Table 4.2.** BET surface area and pore volume results from nitrogen adsorption and desorption techniques.

<b>Silica product from:</b>	<b>Surface area (m<sup>2</sup>/g)</b>	<b>Pore diameter (Å)<sup>a</sup></b>
MS_PECE6K	730	36
MS_PECE4K	848	32
MS_acryPECE6K	952	40
MS_acryPECE4K	831	36

a. values calculated using BJH model.<sup>31</sup>

**Figure 4.1** shows a representative adsorption/desorption isotherm and pore size distribution for the silica product templated by the acrylated PECE-6K macromer. Similar results were obtained for PECE-4K materials. The isotherm in 1a is consistent with Type IV behavior and displays the characteristic hysteresis indicative of mesoporosity.<sup>30</sup> Figure 1b indicates that the average pore diameter is 38-39 Å, calculated using a BJH model to analyze the data.<sup>31,32</sup> In answer to the first posed question above, this new non-ionic surfactant PECE generates high-surface area mesoporous silica with a narrow pore size distribution. To be more specific, the width of the pore size distribution as measured by the width at half-height of the distribution in 1b was 2.5 Å in radius, or 5 Å in pore/channel diameter. For the materials made with the PECE4K template, the width at half-height of the pore diameter distribution was larger at 14 Å.

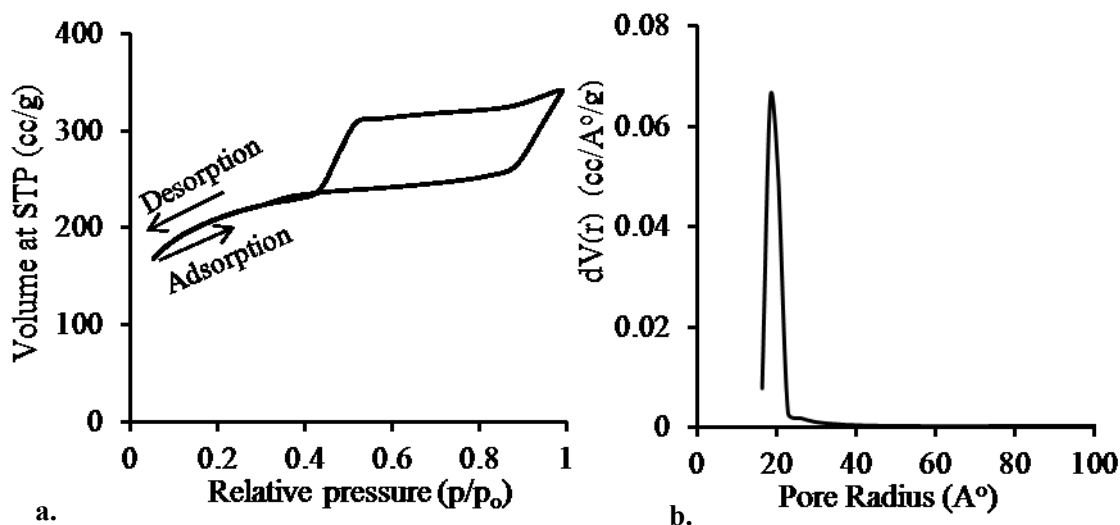


**Figure 4.1.** (a) Nitrogen adsorption-desorption isotherm for calcined silica synthesized using the non-ionic PECE-6K template, and (b) pore size distribution for the same material as in (a).

The results in **Figure 4.1** are supported by representative TEM images of both the PECE4K- and PECE6K-templated silicas, as shown in **Figures 4.2a** and **4.2b**, in which 30-40 Å channels (dark) and 150-160 Å thick walls are clearly distinguished. Small angle x-ray scattering (SAXS) experiments were completed using an SMax3000 instrument, which has the ability to detect scattering vectors in the range of 0.008-0.24 Å<sup>-1</sup>. For the PECE6K silica, a principal scattering peak ( $2\theta = 0.30^\circ$ ) is observed as shown in **Figure 4.2d**, which corresponds to the scattering vector  $q = 0.021 \text{ Å}^{-1}$  or a long period spacing of 290 Å assuming Bragg's law. Similarly, the  $2\theta = 0.46^\circ$  scattering angle for the PECE4K silica corresponds to a scattering vector  $q = 0.033 \text{ Å}^{-1}$  or a long period spacing of 190 Å (**Figure 4.2c**). Together, these results indicate an increased wall thickness for the silicas prepared from the new PECE templates, as compared to traditional mesoporous SBA15, which exhibits a scattering vector  $q = 0.06 \text{ Å}^{-1}$  and average pore diameters of 38-40 Å.

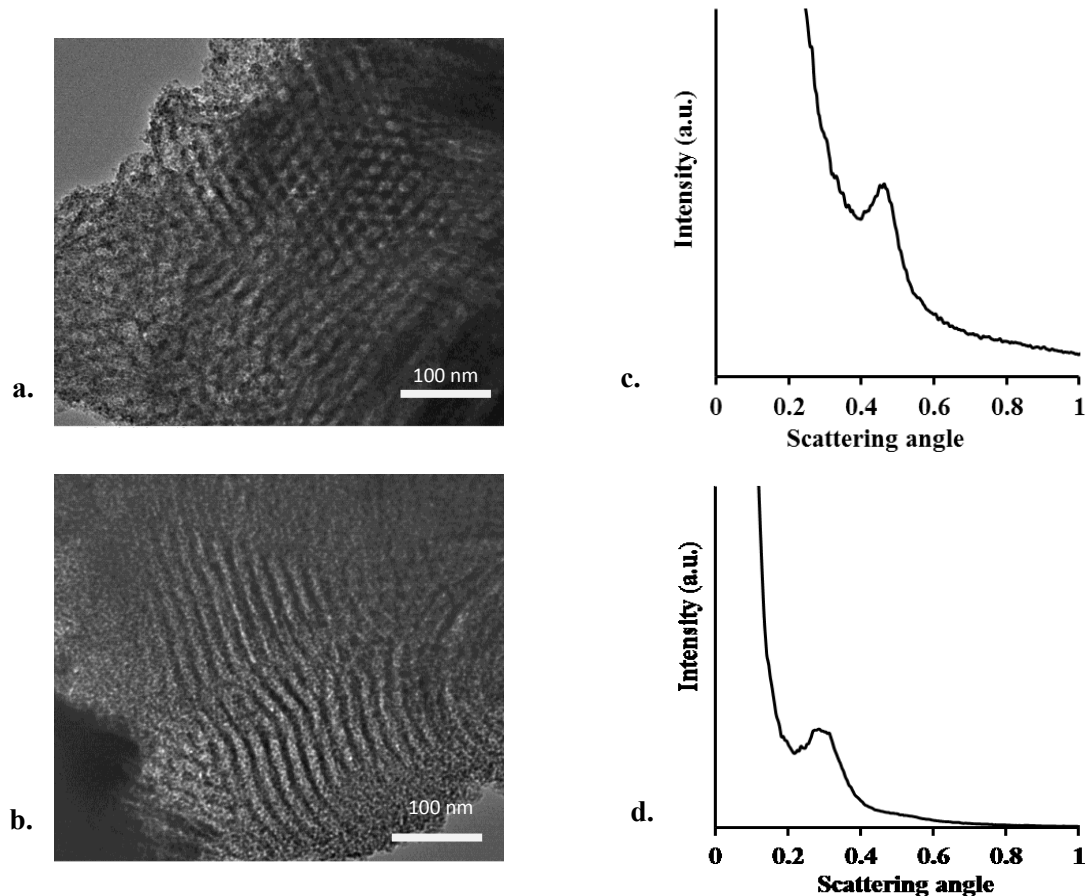


**Figure 4.2.** TEM images for silica templated by (a) the PECE4K macromer and (b) the PECE6K macromer, obtained following calcination to remove the PECE. The open channels/pores appear dark in the image. SAXS results (wavelength = 1.54 Å) for silica (c) templated by PECE4K, and (d) templated by PECE6K.

A typical scanning electron microscopy (SEM) result is shown in **Figure 4.3** for the same PECE6K shown in **Figure 4.2b**, i.e., after calcination to remove the PECE6K template. Again, to avoid confusion, the PECE template is only removed for analysis of the resulting silica by surface area, SAXS, and microscopy methods. To make composites, the acrylated-PECE template is left inside the channels of the silica so that it can react with other acrylated-PECE in order to form the continuous organic phase. In the low magnification image shown in **Figure 4.3a**, one observes a highly anisotropic particle shape, as was observed in most images. Typically, particle dimensions

appeared to range from 1-10  $\mu\text{m}$ 's. More interesting is the high magnification image in **4.3b**, in which one observes porosity defined by wall dimensions (30-33 nm) that generally agree with those reported in **Figure 4.2**, albeit with reduced accuracy relative to the TEM and SAXS results. The key conclusion is that the acrylated-PECE templates the formation of a mesoporous silica, and unless the PECE is removed by calcination, it will remain inside the mesoporous silica available for subsequent polymerization reactions.

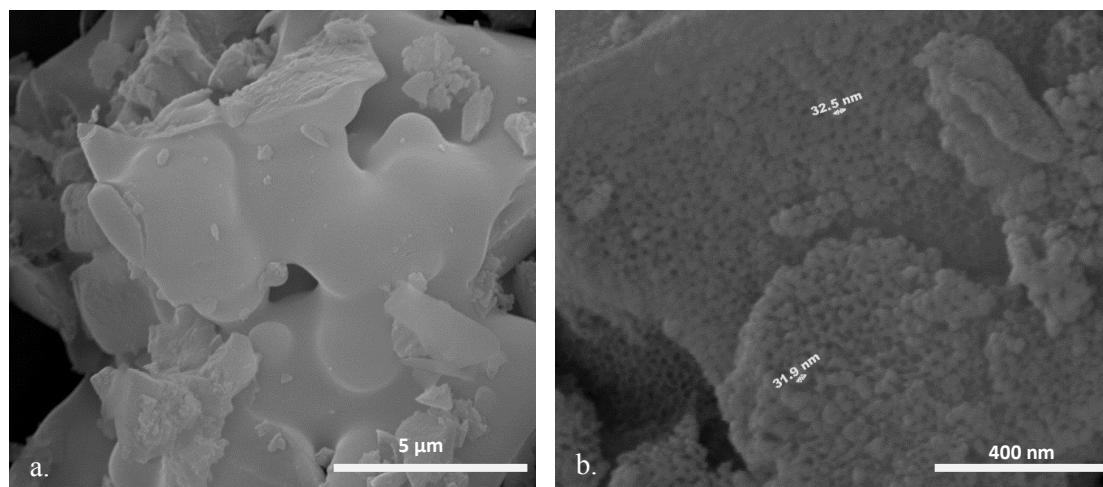


**Figure 4.3.** SEM images for silica templated by the acrylated-PECE6K macromer at **(a)** 20,000 $\times$  and **(b)** 210,000 $\times$  magnification.

Control reactions using pure acrylated-PECE4K and acrylated-PECE6K were used to address the second question, regarding reactivity of functionalized PECE surfactants. If AIBN-initiated end-group chemistry does not lead to polymerization in the pure acrylated-PECE, then polymerization of the PECE template/silica composites to form the extended nanocomposite network will not work. The control reactions generated a viscous gel that was not soluble in common solvents, but swelled in a manner consistent with formation of a cross-linked polymer network. Such network formation is expected, given the presence of some di-acrylated PECE chains, and similarly, there may also exist some completely unreacted chains due to template molecules with no acrylate end groups. Given the successful end-group reactions in the pure



PECE controls, free radical polymerization of the PECE templates that are present within and around the mesoporous silica hosts following silica synthesis generated a crosslinked nanocomposite network in which the high-surface area silica particles were distributed throughout the matrix. In all cases, as shown in **Figure 4.4a**, the resulting PECE/silica nanocomposites swelled, but the overall swell ratio and solvent uptake capacities decreased with increasing mesoporous silica incorporation.

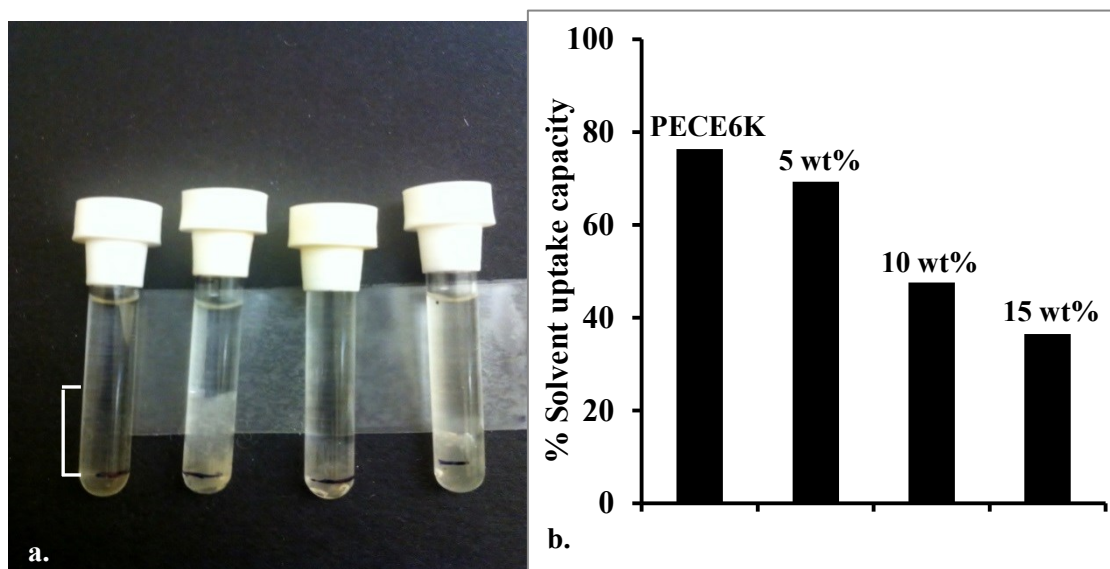


**Figure 4.4.** (a) Images acquired for 1,4-dioxane swollen polymerized acrylated-PECE6K (far left) and (proceeding to the right) its 5, 10, and 15 wt% silica nanocomposites following polymerization. The black mark on each vial indicates the starting volume of the networked material before swelling. (b) Solvent uptake capacities for polymerized pure acrylated-PECE6K and its nanocomposite networks, where solvent uptake capacity is defined as (solvent mass/mass swollen network)\*100.

Linear viscoelastic regimes for rheological experiments were determined at 1 Hz frequency with variable strain measurements (0.01 to 10%). The top row of **Figure 4.5** shows that the linear viscoelastic region of the nanocomposite materials is in the 0.01% to 1% strain region. In accordance with the strain sweep data, frequency sweep data was then collected at 0.15% strain and is shown in the bottom of **Figure 4.5**. The frequency sweep data indicates that the modulus increases almost 2 orders of magnitude with the addition of 15 wt. % silica. Considering the case of no added silica, the terminal behavior at low frequency does not reach that of a linear polymer ( $G' \sim \omega^2$  and  $G'' \sim \omega$  on a log scale) but also does not reach that of a highly crosslinked polymer either. Also, there is no evidence of a percolation transition in this data, as shown in **Figure 4.6**, since the modulus increases almost linearly with loading in the logarithmic plot. Adding silicas of various types are known to improve the modulus in polymers; at this first stage in the project it appears that having the silica formed in-situ in the composite does not necessarily result in a lower percolation threshold relative to traditional mixing. Theoretical calculations predict that 30 wt. % silica is required to reach the percolation threshold, which is above the 15 % limit here, but reports vary widely as to actual amounts required.<sup>33</sup>

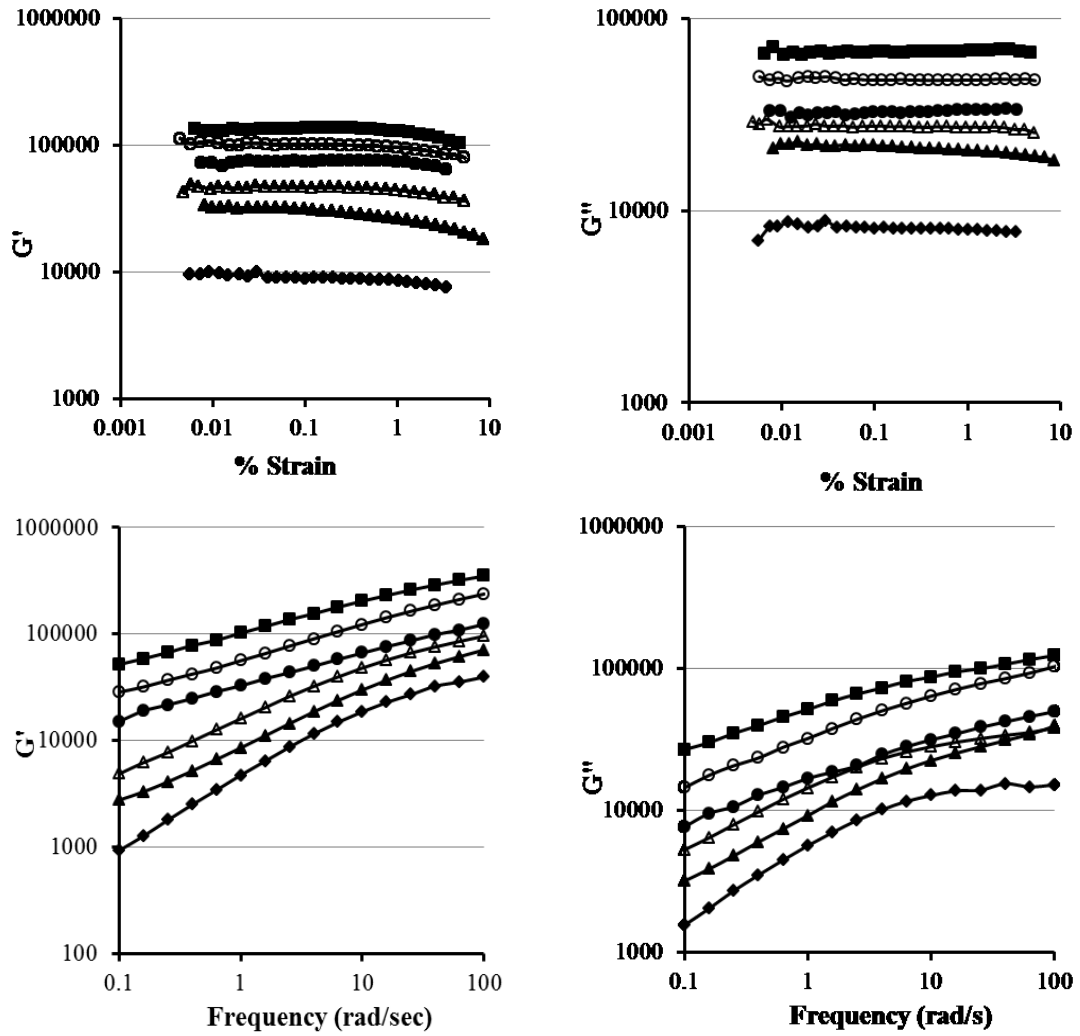


**Figure 4.5.** Storage moduli ( $G'$ ) and loss moduli ( $G''$ ) collected from strain sweep (**top row**) and frequency sweep (**bottom row**) of ( $\blacklozenge$ ) polymerized PECE6K; ( $\blacktriangle$ ) polymer nanocomposite network with 5, ( $\triangle$ ) 7.5, ( $\bullet$ ) 10, ( $\circ$ ) 12.5, and ( $\blacksquare$ ) 15 wt. % silica content.

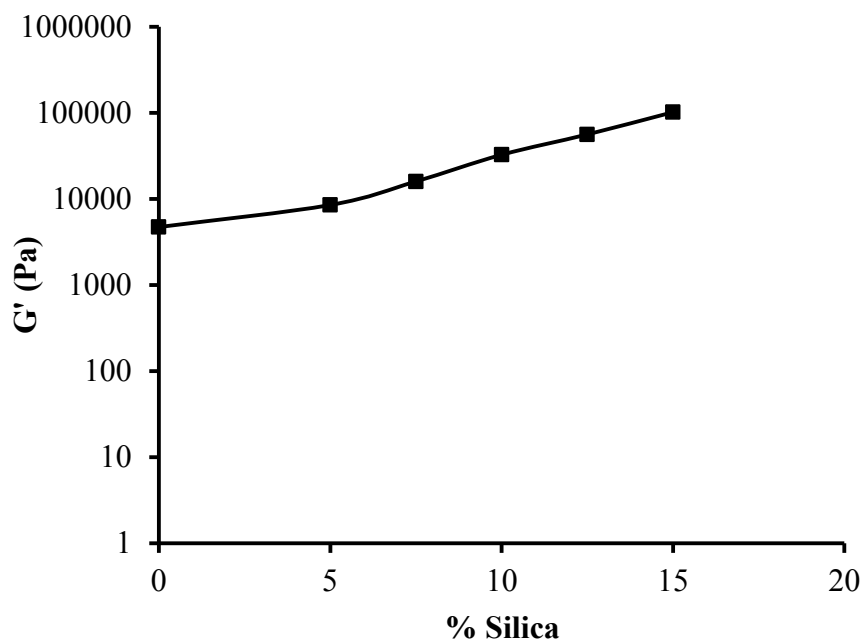


**Figure 4.6.** Plot of storage modulus  $G'$  (log scale) taken at 1 rad/s versus weight percentage of silica for nanocomposites prepared in-situ using the PECE6K template. Data were acquired at 60°C.

From the experimental results described above, we propose the schematic in **Figure 4.7** to depict a molecular view of the chemistry leading to the nanocomposite network formation. TEOS molecules organize around the PECE polymer micelles in the synthesis gel, and slowly react in the acidic solution to form the covalent silica network. The PECE polymer molecules remain in the channels and voids of the silica, and react with one another and additional PECE polymers (depending on the desired organic content) at the time the AIBN initiator is added. Because both monofunctional and bifunctional acrylated-PECE polymers exist in the reaction mixture, the organic phase is a branched and cross-linked network, as illustrated in **Figure 4.7**. Again, if the PECE is removed prior to network reactions via calcination, then the ca. 900 m<sup>2</sup>/g silica is available for other uses.

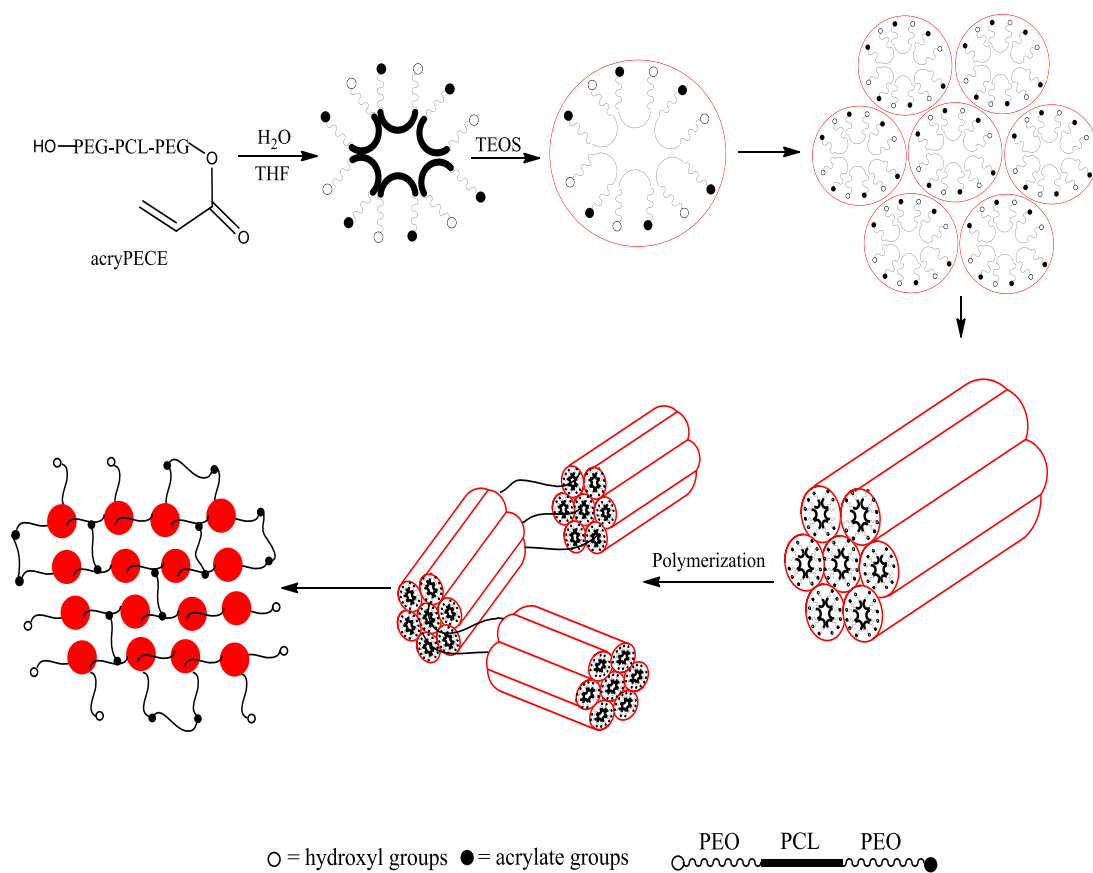


**Figure 4.7.** General schematic representation of self-assembly and synthesis of polymer composites using acrylated-PECE macromer templates. After organization of the mesoporous silica matrix occurs, polymerization between PECE macromers takes place within and outside of those particles. The small orange circles in the lower left frame of the reaction scheme are an idealized representation of individual particles in the network, which of course are not regularly arrayed as shown. Cross-linking to form networks occurred due to the reactivity of macromers that contain acrylate groups on both chain ends.

#### 4.6 Conclusions

A new ethylene oxide/caprolactone based biomacromolecular surfactant was synthesized and converted to a reactive macromer via acrylate end group functionalization. The resulting triblock polymers organize the formation of high-surface area silica around their micelles, ultimately leading to the growth of hybrid organic/inorganic building blocks that can react via free-radical polymerization to form nanocomposite networks. Crosslinking occurs due to the presence of diacrylate-functionalized triblocks, and when this occurs in the presence of the

macromer/high-surface area silica products, the resulting nanocomposite network has a distribution of purely covalent nodes as well as nodes formed by the functional silica particles themselves. The resulting storage and loss moduli show significant increases as the silica content increases. The final composite should be both biodegradable and biocompatible given that its constituents are based on ethylene oxide and caprolactone, and future work will focus on exploring applications that exploit these properties.

#### 4.7 References

1. Wight, A. P.; Davis, M. E. Design and Preparation of Organic-Inorganic Hybrid Catalysts. *Chem. Rev.* **2002**, *102*, 3589-3614.
2. Bitinis, N.; Hernandez, M.; Verdejo, R.; Kenny, J. M.; Lopez-Manchado, M. A. Recent Advances in Clay/Polymer Nanocomposites. *Adv. Mater.* **2011**, *23*, 5229-5236.
3. He, J.; Shen, Y.; Evans, D. G.; Duan, X. Nanocomposite Structure Based on Silylated MCM-48 and Poly(vinyl acetate). *Chem. Mater.* **2003**, *15*, 3894-3902.
4. Landry, C. J. T.; Coltrain, B. K.; Brady, B. K. In-situ Polymerization of Tetraethylorthosilane in Poly(methyl methacrylate): Morphology and Dynamic Mechanical Properties. *Polymer* **1992**, *33*, 1486-1495.
5. Xu, L.; Hiroyoshi, N.; Evangelos, M.; Ramanan, K. Tailored Nanocomposites of Polypropylene with Layered Silicates. *Macromolecules* **2009**, *42*, 3795-3803.
6. Rovira-Truitt, R.; Patil, N.; White, J. L. Synthesis and Characterization of Biopolymer Composites from the Inside Out. *Macromolecules* **2009**, *42*, 7772-7780.
7. Choi, M.; Kleitz, F.; Liu, D.; Lee, H. Y.; Wha-Seung, A.; Ryoo, R. Controlled Polymerization in Mesoporous Silica Toward the Design of Organic-Inorganic Composite Nanoporous Materials. *J. Am. Chem. Soc.* **2005**, *127*, 1924-1932.
8. Lunn, J. D.; Shantz, D. F. Peptide Brush-Ordered Mesoporous Silica Nanocomposite Materials. *Chem. Mater.* **2009**, *21*, 3638-3648.

9. Kruk, M.; Dufour, B.; Celer, E. B.; Kowalewski, T.; Jaroniec, M.; Matyjaszewski, K. Grafting Monodisperse Polymer Chains from Concave Surfaces of Ordered Mesoporous Silica. *Macromolecules* **2008**, *41*, 8584-8591.
10. Pasetto, P.; Blas, H.; Audouin, F.; Boissière, C.; Sanchez, C.; Save, M.; Charleux, B. Mechanistic Insight into Surface- Initiated Polymerization of Methyl methacrylate and Styrene via ATRP from Ordered Mesoporous Silica Nanoparticles. *Macromolecules* **2009**, *42*, 5983-5995.
11. El Kadib, A.; Katir, N.; Finiels, A.; Castel, A.; Marcotte, N.; Molvinger, K.; Biolley, C.; Gaveau, P.; Bousmina, M.; Brunel, D. Mesostructured Fatty Acid-Tethered Silicas: Sustaining the Order by Co-templating with Bulky Precursors. *Dalton Trans.* **2013**, *42*, 1591-1602.
12. Hsu, Y-C.; Hsu, Y-T.; Hsu, H-Y.; Yang, C-M. Facile Synthesis of Mesoporous Silica SBA-15 with Additional Intra-Particle Porosities. *Chem. Mater.* **2007**, *19*, 1120-1126.
13. Summers, M.; Eastoe, J. Applications of Polymerizable Surfactants. *Adv. Colloid Interface Sci.* **2003**, 100–102, 137-152.
14. Dreja, M.; Tieke, B. Microemulsions with Polymerizable Surfactants  $\gamma$ -ray Induced Copolymerizations of Styrene and 11-(acryloyloxy)undecyltrimethyl ammonium bromide in Three Component Cationic Microemulsion. *Macromol. Rapid Commun.* **1996**, *17*, 825-833.
15. Li, T. D.; Gan, L. M.; Chew, C. H.; Teo, W. K.; Gan, L. H. Preparation of Ultrafiltration Membranes by Direct Microemulsion Polymerization Using Polymerizable Surfactants. *Langmuir* **1996**, *12*, 5863-5868.
16. Li, G. T.; Bhosale, S.; Li, F. T.; Zhang, Y. H.; Guo, R. R.; Zhu, H.; Fuhrhop, J. H. Template Synthesis of Functionalized Polystyrene in Ordered Silicate Channels *Chem. Comm.* **2004**, *15*, 1760-1761.
17. Li, G. T.; Bhosale, S.; Li, F. T.; Wang, T. Y.; Zhang, Y.; Zhu, H.; Fuhrhop, J. H. Gram-Scale Synthesis of Submicrometer-Long Polythiophene Wires in Mesoporous Silica Matrices. *Angew. Chem. Int. Ed.* **2003**, *42*, 3818-3821.

18. Petrova, S.; Miloshev, S.; Mateva, R.; Iliev, I. Synthesis of amphiphilic PEG-PCL-PEG triblock copolymers. *J. Univ. Chem. Tech. and Metallurgy* **2008**, *43*, 199.
19. Hwang, M. J.; Joo, M. K.; Choi, B. G.; Park, M. H.; Hamley, I. W.; Jeong, B. Multiple Sol-Gel Transitions of PEG-PCL-PEG Triblock Copolymer Aqueous Solution *Macromol. Rapid Commun.* **2010**, *31*, 2064.
20. Hwang, M. J.; Suh, M. J.; Bae, Y. H.; Kim, S.W.; Jeong, B. Caprolactonic Poloxamer Analog: PEG-PCL-PEG. *Biomacromolecules* **2005**, *6*, 885-890.
21. Walberer, J. A.; McHugh, A. J. The Linear Viscoelastic Behavior of Highly Filled Polydimethylsiloxane Measured in Shear and Compression. *J. Rheol.* **2001**, *45*, 187-201.
22. Li, J. G.; Chang, Y. H.; Lin, Y. S.; Kuo, S. W. Templating Amphiphilic Poly(ethylene oxide-b- $\epsilon$ -caprolactone) Diblock Copolymers Provides Ordered Mesoporous Silicas With Large Tunable Pores. *RSC Adv.* **2012**, *2*, 12973-12982.
23. Li, J. G.; Kuo, S. W. Phase Behaviour of Mesoporous Nanostructures Templated by Amphiphilic Crystalline Diblock Copolymers of Poly(ethylene oxide-b- $\epsilon$ -caprolactone). *RSC Advances* **2011**, *1*, 1822–1833.
24. Beck, J. S.; Vartuli, J. C.; Roth, W. J.; Leonowicz, M. E.; Kresge, C. T.; K., Schmitt, D.; Chu, C. T.-W.; Olson, D. H.; Sheppard, E. W.; McCullen, S. B.; Higgins, J. B.; Shchlenker, J. L. A New Family of Mesoporous Molecular Sieves Prepared With Liquid Crystal Templates. *J. Am. Chem. Soc.* **1992**, *114*, 10834-10843.
25. Chen, C. Y.; Li, H. X.; Davis, M. E. Studies on Mesoporous Materials: I. Synthesis and Characterization of MCM-41. *Microporous Mater.* **1993**, *2*, 17-26.
26. Huo, Q.; Margolese, D. Y.; Ciesla, U.; Feng, P.; Gier, T. E.; Sieger, P.; Leon, R.; Petroff, P. M.; Schuth, F.; Stucky, G. D. Generalized Synthesis of Periodic Surfactant/Inorganic Composite Materials. *Nature* **1994**, *368*, 317-321.



27. Corma, A., Kan, Q., Navarro, M. T.; Perez-Pariente, J.; Rey, F. Synthesis of MCM-41 With Different Pore Diameters Without Addition of Auxiliary Organics. *Chem. Mater.* **1997**, *9*, 2123-2126.
28. Zhao, D.; Feng, J.; Huo, Q.; Melosh, N.; Fredrickson, G. H.; Chmelka, B. F.; Stucky, G. D. Triblock Copolymer Syntheses of Mesoporous Silica with Periodic 50 to 300 Angstrom Pores. *Science* **1998**, *279*, 548-552.
29. Mesa, M.; Sierra, L.; Guth, J. Contribution to the study of the formation mechanism of mesoporous SBA-15 and SBA-16 type silica particles in aqueous acid solutions. *Microporous and Mesoporous Mater.* **2008**, *112*, 338-350.
30. Tompsett, G. A.; Krogh, L.; Griffin, D. W.; Conner, W. C. Hysteresis and Scanning Behaviour of Mesoporous Molecular Sieves. *Langmuir* **2005**, *21*, 8214-8225.
31. Barrett, E. P.; Joyner, L. G.; Halenda, P. P. The Determination of Pore Volume and Area Distributions in Porous Substances. *J. Am. Chem. Soc.* **1951**, *73*, 373-380.
32. Maglara, E.; Kaminski, R.; Conner, W. C. In *Characterization of Porous Solids IV*; McEnaney, B., Mays, T.J., Rouquerol, J., Rodrigues-Reinoso, F., Sing, K. S. W., Unger, K. K.; Royal Society of Chemistry:London, **1997**
33. Lunn, J. D.; Shantz, D. F. Peptide Brush-Ordered Mesoporous Silica Nanocomposite Materials. *Chem. Mater.* **2009**, *21*, 3638-3648.
34. Zhang, Q.; Archer, L. A. Poly(ethylene oxide)/Silica Nanocomposites: Structure and Rheology. *Langmuir* **2002**, *18*, 10435-10442.

## CHAPTER V

### FUTURE WORK

Apart from three routes: co-condensation, post-grafting, and sol-gel; we have developed another route to synthesis polymer nanocomposites via self-assembly. We have shown the application of surfmer to synthesis polymer nanocomposites with increased mechanical strength via network formation. Such crosslinked networks are difficult to transform the polymer nanocomposites into a desired shape using any fabrication techniques. The crosslinking resulted due to the mixture of mono- and bi- functionalized surfmer. Future work will include the separation of bi-functionalized from mono-functionalized surfmer. It would be interesting to synthesize the polymer nanocomposites via aforementioned self-assembly using mono-functionalized surfmer. In this way, the obtained polymer nanocomposites will be thermoplastic and can be shaped for desired application. The characterization such as tensile strength, impact resistance, and flexural strength will be performed in order to determine its mechanical property.

It is also important to compare the mechanical properties of the polymer nanocomposites obtained via self-assemble route with the traditional polymer nanocomposites containing non-porous silica (such as Cab-O-Sil) as an inorganic component.

We have shown the application of biocompatible and biodegradable poly(ethylene oxide)-poly(caprolactone)-poly(ethylene oxide) (PECE) triblock copolymer as structure directing agent to organize the mesoporous silica. The mesoporous silica obtained has high surface area

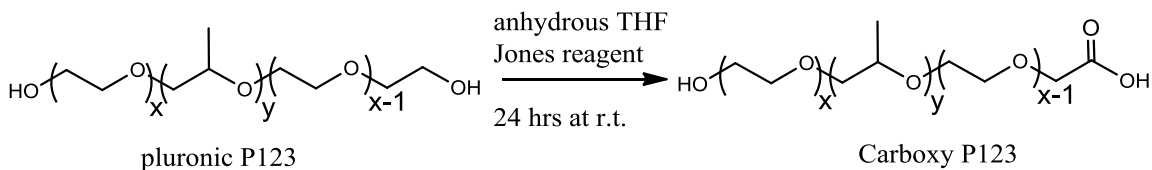
and thick walls with some degree of disordered structure. Future work will include the fine tuning of the type of silica precursors and reaction conditions useful to obtain the resolved structural features of mesoporous silica using PECE as surfactant. The characterization such as adsorption-desorption, BET surface area, TEM, SEM, and SAXS will be performed to observe the structure of mesoporous silica.

When silica used as additives, they are first pre-treated with the modifying agents to minimize the interfacial adhesion. The mesoporous silica synthesized in this research work possess reactive component inside the pores. Therefore, it will be interesting to find its application as additives as such silica does not require pre-treatment.

## APPENDICES

### A1. End-group functionalization of triblock copolymer pluronic P123.

Pluronic P123 was purchased from Sigma Aldrich and used as such for functionalization reactions. All organic solvents were obtained from Pharmco-AAPER. In a 250 ml two-necked flask, Pluronic P123 (1mmol) was dissolved in 100 mL anhydrous tetrahydrofuran (THF) in an inert atmosphere. 4mmol of the Jones reagent (a solution of chromium trioxide in a diluted sulphuric acid) is added to the stirred solution. The reactants are allowed to react for 24hours at room temperature. The excess Jones reagent was then quenched using saturated solution of sodium bi-sulphite. The product was then extracted using dichloromethane. The product was recovered by evaporating dichlormethane.



**Scheme A1.** Oxidation of pluronic P123 using Jones reagent

**A2. Characterization of carboxy P123.** Shown below in Figure A1 is the 600-MHz solution  $^{13}\text{C}$  NMR spectrum of **carboxyP123**. The spectrum was obtained with gated decoupling to minimize Overhauser effects. In order to preserve the structure-directing capabilities of P123, we targeted ca. 50% conversion of hydroxyl groups to carboxylic acid group in the oxidation reaction. In other words, we wanted an average of one carboxylic acid and one hydroxyl chain end per **carboxyP123** molecule. From Figure A1, which compares the starting P123 spectrum to the product **carboxyP123** spectrum, one observes based on the relative intensities of the 60, 67, and 172 ppm end-group peaks in the two spectra that this target was achieved. Note that the starting P123 in Figure 1 has only the characteristic 60-ppm end group peak for the methylene group adjacent the terminal hydroxyl.

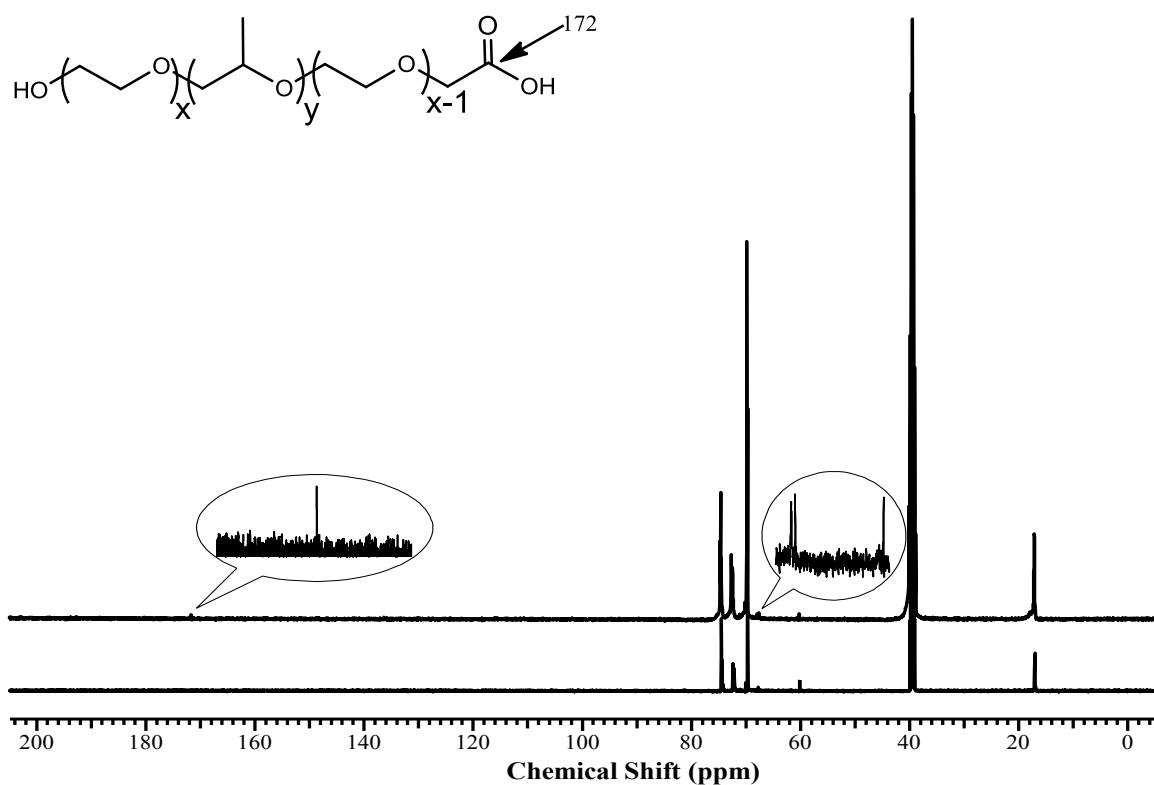


**Figure A2.1.** 600 MHz  $^{13}\text{C}$  solution NMR spectrum acquired with  $^1\text{H}$  decoupling of **(bottom)** pure P123 starting material and **(top)** carboxy-functionalized P123 following reaction according to Scheme A1. End group signals are shown in the **carboxyP123** inset.

**A3. Synthesis of SBA-15 and SBA-15 analogues.** The molar composition for the synthesis of SBA-15 or SBA-15 type materials is TEOS:P123/**carboxyP123** :HCl:H<sub>2</sub>O = 1: 0.0016 : 5.54 : 182.82, where TEOS is tetraethylorthosilicate. In a typical synthesis, 4 g of P123 or **carboxyP123** was dissolved in 30 mL of de-ionized water and stirred for 3 hours at room temperature, and 112 mL of 2.133 M HCl was added drop-wise and kept under stirring for 2 hours. The above solution was then heated to 40 °C and 9 g of TEOS was added drop-wise and stirred for 20 hours. The reaction mixture was aged at 100°C for 24 hours under static conditions. The materials from each solution was washed with excess de-ionized water, dried overnight, and calcined at 550°C for 7 hours using a temperature ramp of 1°C/min. As described in the text, TGA, XRD, and BET analysis verified that crystalline mesoporous SBA-15 siliceous materials were formed in the presence of either P123 or **carboxyP123**.

#### **A4. Characterization of SBA15\_carboxyP123.**

**Figure A4.1a** and **A4.1b** shows a representative adsorption/desorption isotherm and pore size distribution for the silica product templated by the **carboxyP123**. The isotherm in **A4.1a** is consistent with Type IV behavior and displays the characteristic hysteresis indicative of mesoporosity. **Figure A4.1b** indicates that the average pore diameter is 32 Å, calculated using a BJH model to analyze the data. For **carboxyP123** template synthesis, the resulting mesoporous silica surface area was 900 m<sup>2</sup>/g identical to that expected for SBA-15 structures synthesized from the unfunctionalized P123.

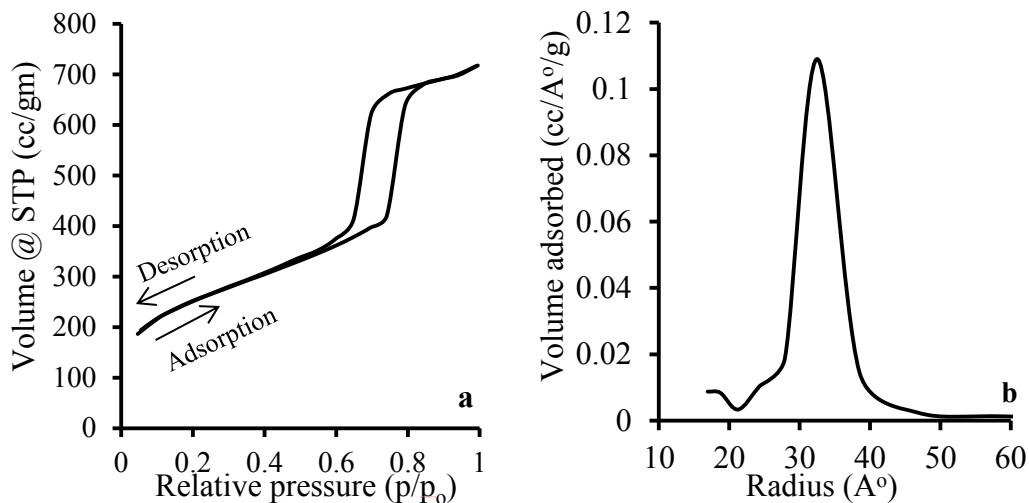


**Figure A4.1.** a) adsorption-desorption curves and b) pore size distribution of SBA15\_carboxyP123

The characteristic ca. 4 nm hexagonally-arrayed channels are observed in transmission electron microscopy image of SBA15\_carboxyP123 (shown in **Figure A4.2a**). **Figure A4.2b** compares the powder SAXS results from materials synthesized using the control P123 and **carboxyP123** prior to calcinations. SBA15\_carboxyP123 materials exhibit the specific diffraction peaks consistent with published SBA-15 topologies.

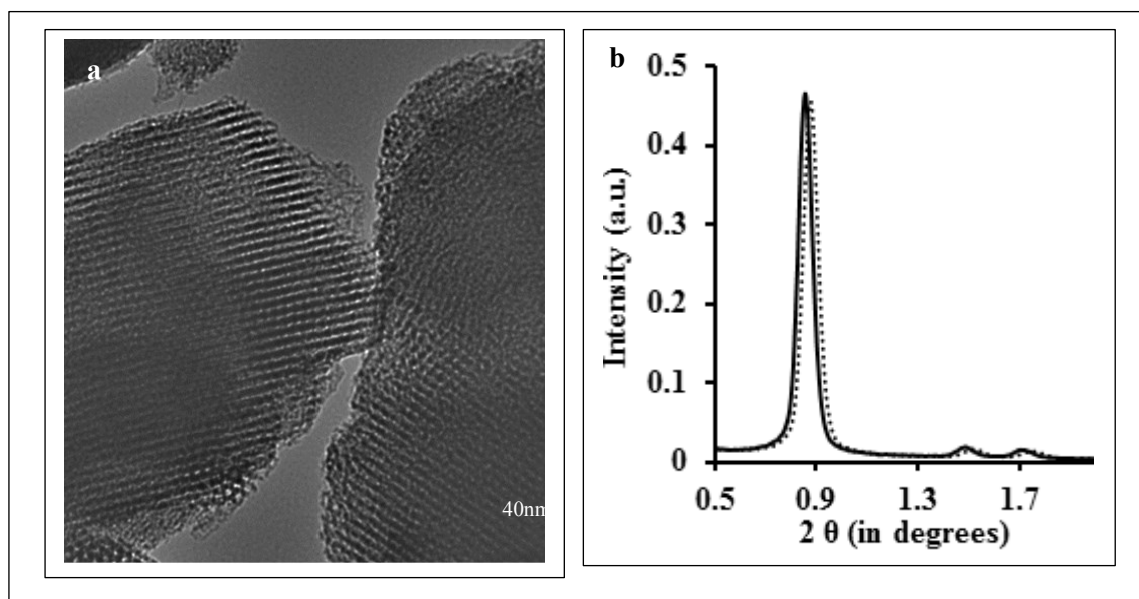


**Figure A4.2.** a) TEM image and b) SAXS data of SBA15\_carboxyP123. SAXS plot of SBA15\_P123 is shown in solid line while SBA15\_carboxyP123 is shown in dotted line.

## B1. Thermal Gravimetric Analysis of Polymer nanocomposites from styrP123 and SBA15\_styrP123.

Percentage organic contents of the polymer nanocomposites were determined on TA-instruments Hi-ResTGA2950. The samples were heated from room temperature to 500°C with a ramp rate of 20°C/min under air flow. Figure B1.1 shows the THGA thermograms of polymer nanocomposites.

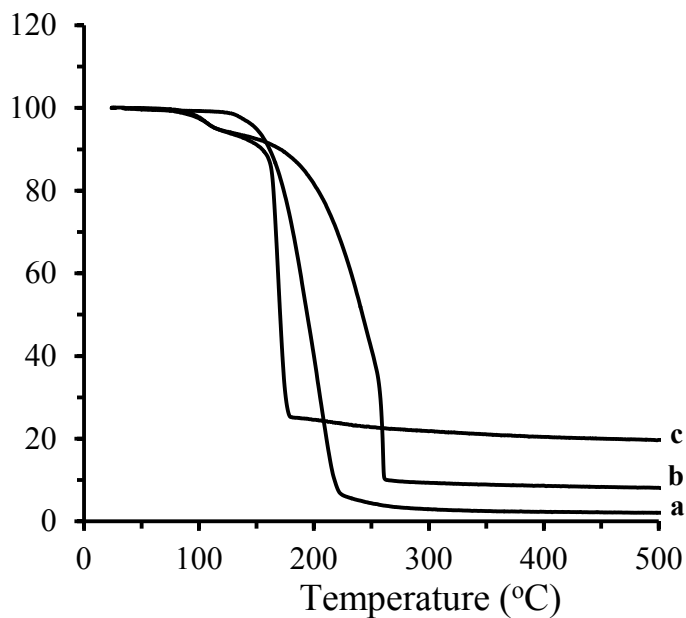


**Figure B1.1.** TGA thermograms of polymer nanocomposites prepared using styrP123 and SBA15\_styrP123 with a) 0%, b) 10%, and c) 20% silica content.



## B2. Fourier Transform Infra-red of acryP123.

Fourier transform infrared (FT-IR) spectra were obtained in the wave number range 600-4000  $\text{cm}^{-1}$  using a Perkin Elmer Fourier transform infrared spectrometer using the NaCl plates with 32 scans. Figure B2.1 shown below is a series of FTIR spectra of pluronic P123, acryloyl chloride, and acryP123. The presence of carbonyl stretch ca.  $1725\text{cm}^{-1}$  in acryP123 (Figure B2.1c) confirms the functionalization of pluronic P123.

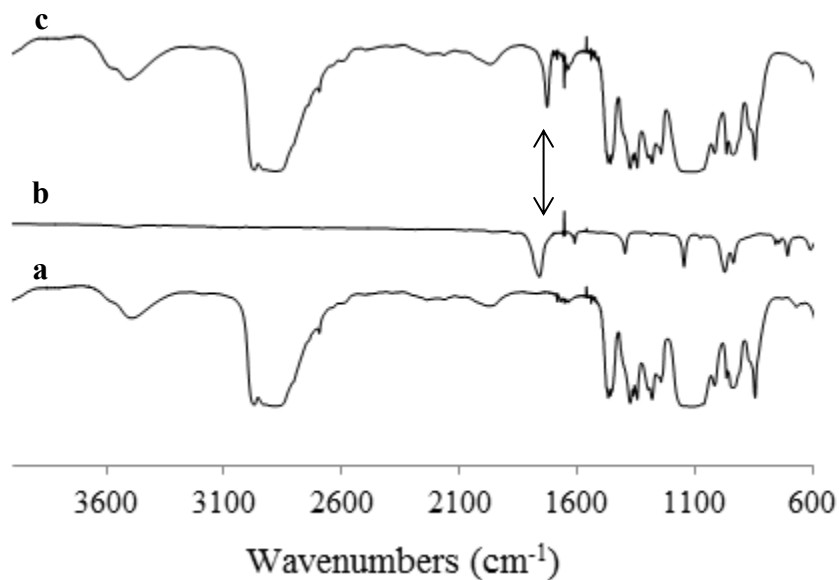


**Figure B2.1** FTIR spectra for a) pluronic P123, b) acryloyl chloride, and c) acryP123. The arrow denotes the carbonyl stretch from acrylic group.

**C1. Characterization of the PECE (poly-ethylene oxide-caprolactone-ethylene oxide) triblock copolymer.** The overall reaction scheme is reproduced below for clarity. In order to verify that the triblock copolymer sequence was produced, quantitative analysis of the 400 MHz  $^1\text{H}$  solution NMR data was required.

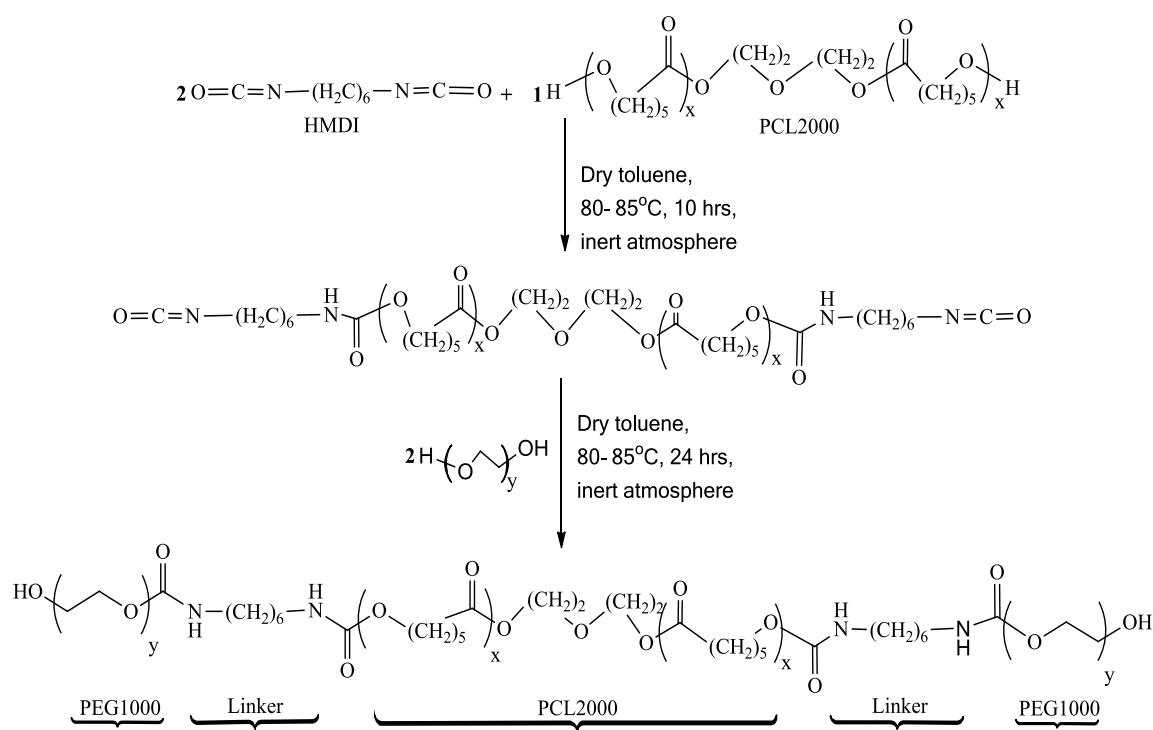
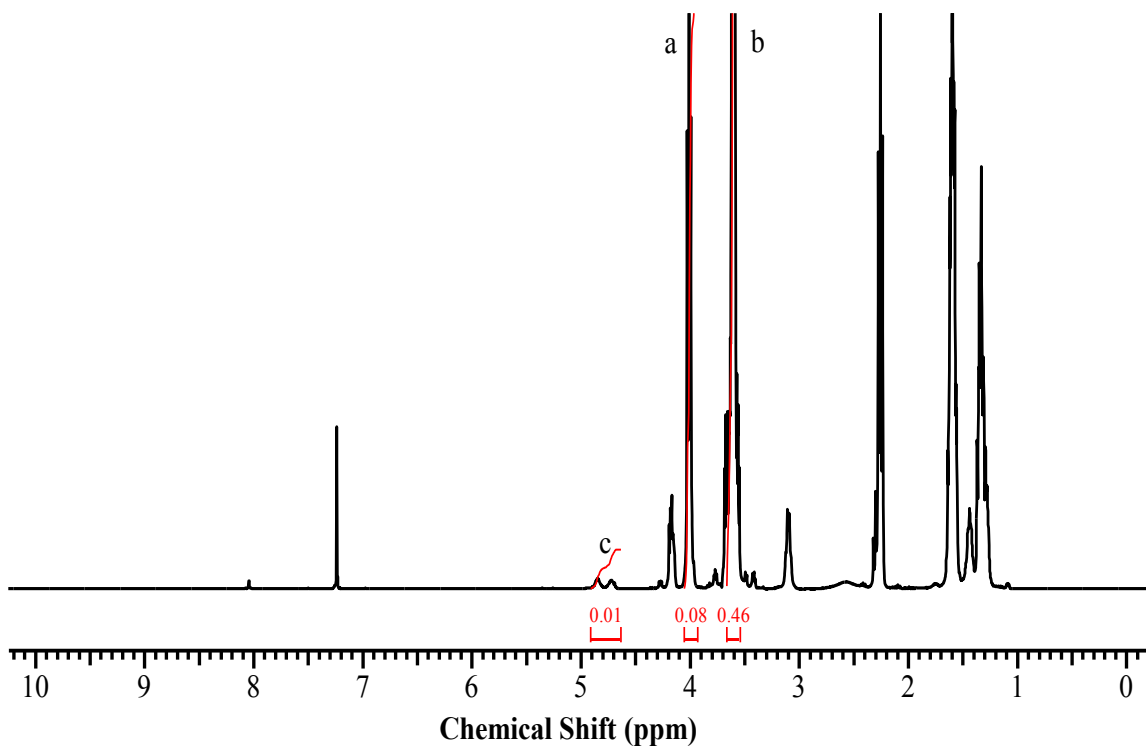
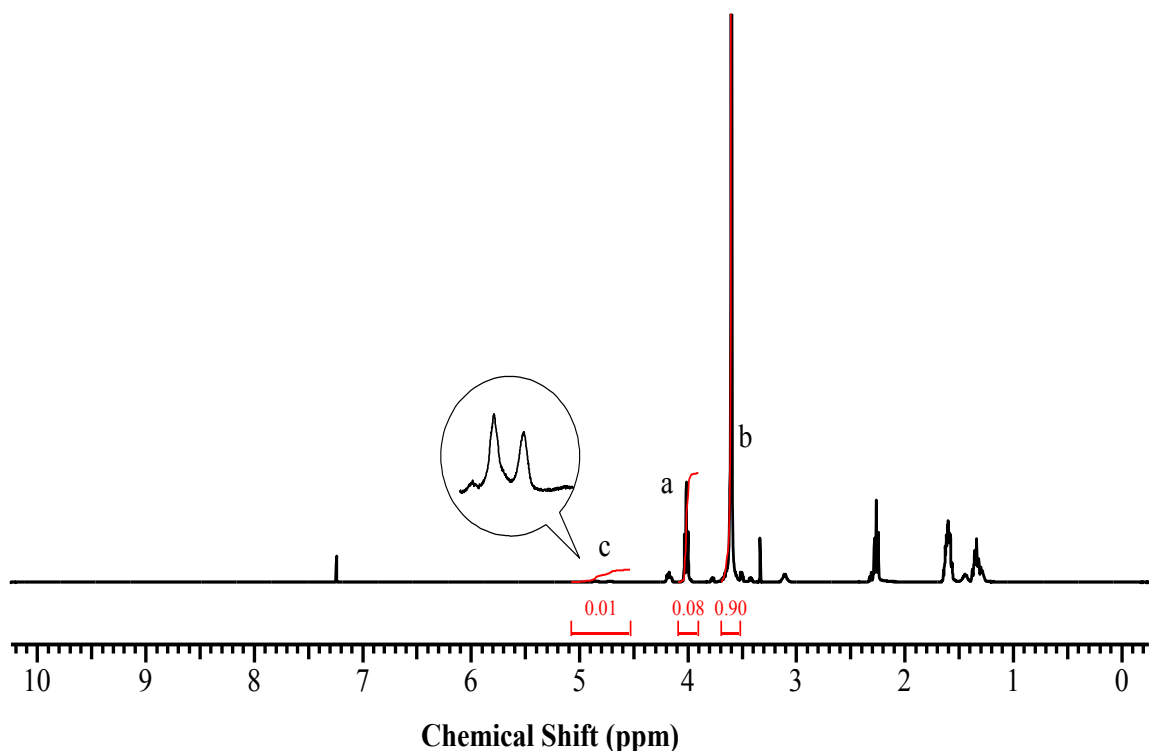


Figure C1.1 and C1.2 show the NMR data of PECE4K and PECE6K, with peaks labeled according to the structure scheme provided above. The most intense peak, labeled **b** at 3.6 ppm, arises from the ethylene oxide blocks, while the 4.0 ppm peak labeled **a** originates from the caprolactone block. Given that the caprolactone reagent is a diol, there are four additional ethylene oxide units that contribute eight hydrogens to the **b** signal. If the washed and purified product exists as the 4000 molecular weight triblock copolymer, the ratio of signal **b** to signal **a** in Figure S1 should be 5.65:1, as there are 198 ethylene oxide hydrogens and 34 caprolactone hydrogens for the groups in the respective signals **b** and **a**. From the integral regions shown

below each peak, we see that the ratio  $0.46:0.08 = 5.75:1$ . Furthermore, peak **c** arises from the four urethane linkages per triblock, giving rise to four chemically unique hydrogens. As such, the ratio of its intensity to peak **b** should be  $192:4$ , or  $48:1$ . From the integral regions below each peak, we observe that the experimental ratio is  $46:1$ , in agreement with the structure. Similar calculations on PECE6K confirm the molecular weight of that triblock copolymer as 6000.



**Figure C1.1.** 400 MHz  $^1\text{H}$  solution NMR data for the PECE4K triblock copolymer, with peaks labeled according the scheme on top. The solvent was  $\text{CDCl}_3$ .



**Figure C1.2.** 400 MHz  $^1\text{H}$  solution NMR data for the PECE6K triblock copolymer, with peaks labeled according the scheme on top. The solvent was  $\text{CDCl}_3$ .

The molecular weight of each block of triblock copolymer PECE4K and PECE6K is calculated from the equations shown below.  $I_b$  (3.63ppm),  $I_a$  (4.93), and  $I_c$  (4.05) are the intensities of protons of methylene of PEG, urethane, and  $\epsilon$ -methylene from carbonyl carbon of PCL, respectively.  $2X$  and  $Y$  are the respective blocks of polycaprolactone and polyethylene glycol respectively. It can be concluded that polyethylene glycol PEG are attached to both ends of polycaprolactone diol PCL via urethane linkage in both: PECE4K and PECE6K.

$$\frac{I_b}{I_c} = \frac{2(4Y)}{4} \quad (1)$$

$$\frac{I_a}{I_c} = \frac{4(X)}{4} \quad (2)$$

$$M_n(\text{PCL}) = 2(114X) \quad (3)$$

$$M_n(\text{PEG}) = 2(44Y) \quad (4)$$

$$M_n(\text{PECE}) = M_n(\text{PEG}) + M_n(\text{PCL}) \quad (5)$$

FTIR results support formation of the triblock PECE as shown in the schematic. Shown below in Figure C1.3 are a series of spectra obtained for the pure components (a and b), the reaction product of polycaprolactone (PCL) with HDMI (hexamethylene diisocyanate) in C1.3c, and the final triblock copolymer in C1.3d. The arrow between S3c and S3d indicates the expected loss of the N=C=O stretch at  $2280\text{ cm}^{-1}$  following reaction of the PCL-HDMI product with PEO.

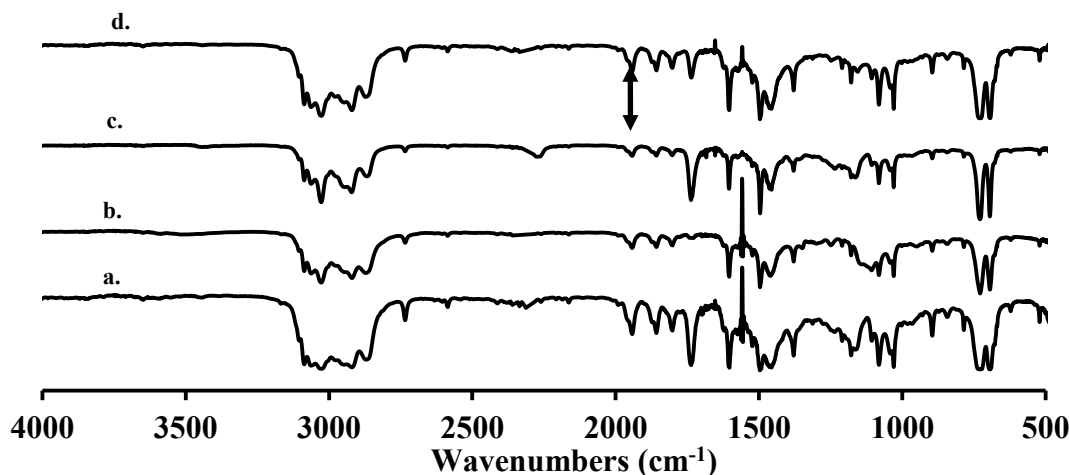


**Figure C1.3.** FTIR spectra for (a) pure PCL, (b) pure polyethylene oxide, (c) the PCL-HDMI reaction product, and (d) the PECE triblock copolymer. The arrow denotes the loss of the N=C=O stretch at  $2280\text{ cm}^{-1}$  following reaction of the PCL-HDMI product

## C2. End group functionalization of PECE with acryloyl chloride:

The hydroxyl groups of PECE (4K or 6K) were converted to acrylate group using acryloyl chloride. The mole ratios were selected in such a way that on an average only one hydroxyl groups were converted to acrylate moiety. Shown in Figure B2.1 and B2.2 are the  $^1\text{H}$  liquid NMR acrylated PECE (4K and 6K). The presence of acrylate groups confirms the successful functionalization of PECE with acrylate groups. Comparing the integrals of acrylate, urethane, methylene of poly(ethylene glycol), and  $\epsilon$ -methylene (relative to the carbonyl group) of

polycaprolactone groups, it can be concluded that, on average one acrylate group is attached to each PECE chain. However, the final product will be a mixture of chains containing zero, one, and two acrylate end groups per chain.

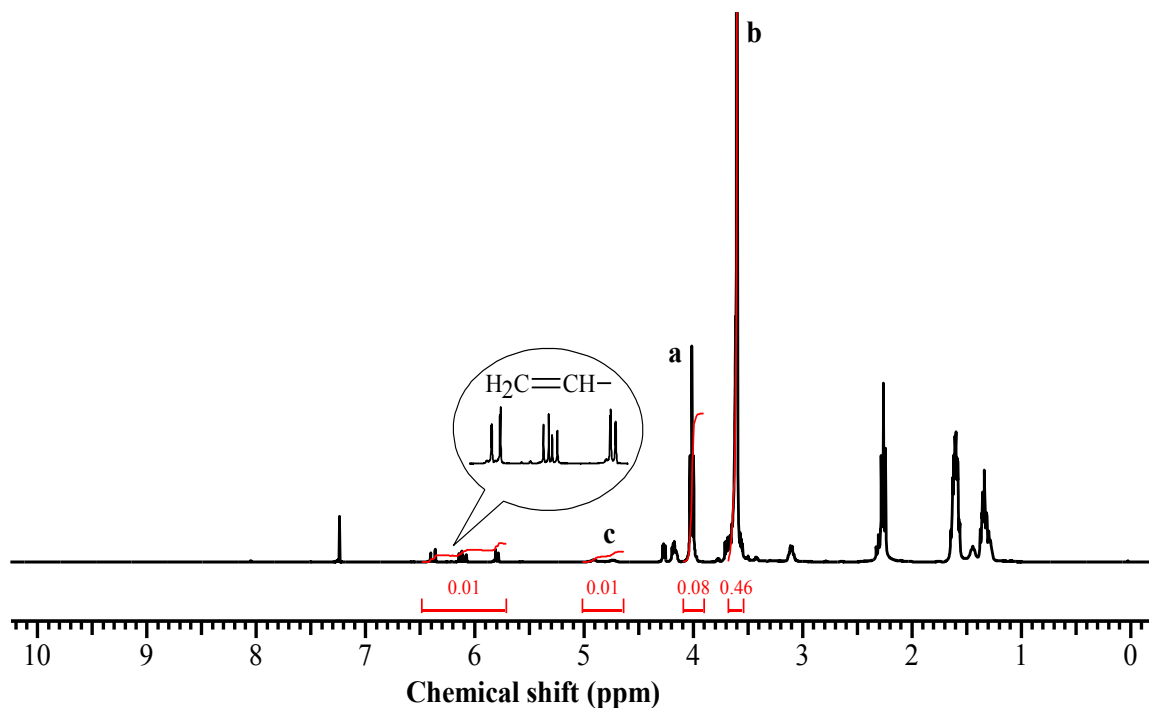
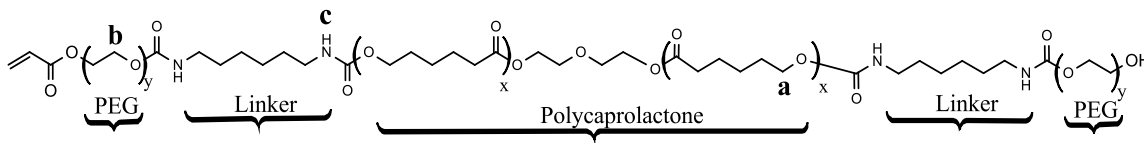


**Figure C2.1.** 400 MHz  $^1\text{H}$  solution NMR data of acryPECE4K triblock copolymer in  $\text{CDCl}_3$ , with peaks labeled according the chemical structure shown above the spectra.

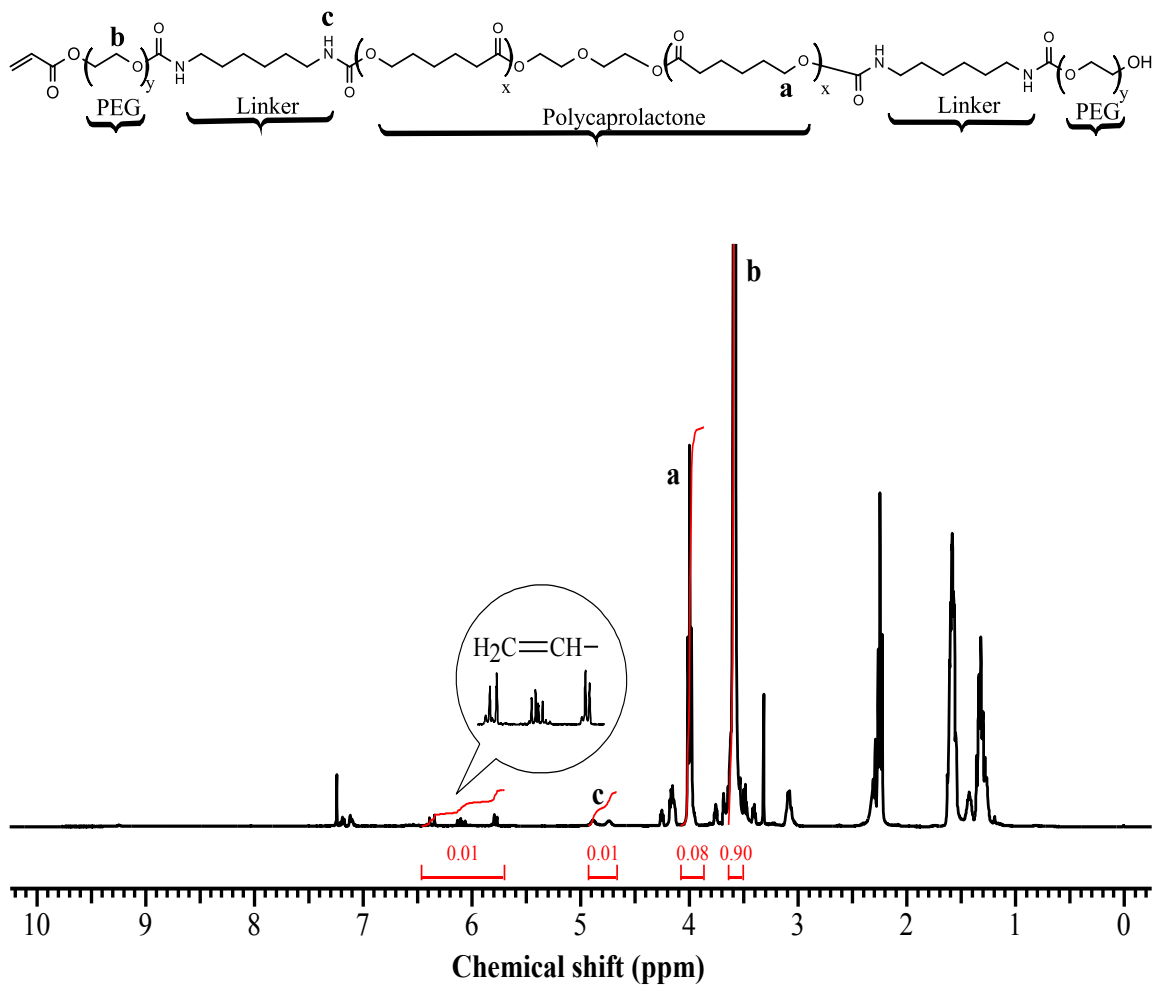


**Figure C2.2.** 400 MHz  $^1\text{H}$  solution NMR data of acryPECE6K triblock copolymer in  $\text{CDCl}_3$ , with peaks labeled according to the chemical structure shown above the spectra.

VITA

Nitin Vikas Patil

Candidate for the Degree of

Doctor of Philosophy

Thesis: SELF-ASSEMBLED POLYMER NANOCOMPOSITES AND THEIR NETWORKS

Major Field: Chemistry

Biographical:

Education:

Completed the requirements for the Doctor of Philosophy in Polymer chemistry at Oklahoma State University, Stillwater, Oklahoma, in December in 2013.

Completed the requirements for the Bachelor of Polymer Engineering and Technology in Polymer at University Institute of Chemical Technology, Mumbai, Maharashtra, India in 2006.

Experience:

Employed by Asian Paints Ltd., Mumbai, India as Polymer Technologist from May 2006-Feb 2008; employed by Oklahoma State University, as graduate research and teaching assistant, 2008 to present.

Professional Memberships:

American Chemical Society (ACS)

ACS, Cellulose and Renewable Materials

ACS, Division of Polymer Chemistry